DESIGN AND FABRICATION OF HIGHLY REFLECTIVE DBRs FOR USE WITH LONG WAVELENGTH VCSELs

DESIGN AND FABRICATION OF HIGHLY REFLECTIVE DBRs FOR USE WITH LONG WAVELENGTH VCSELs

By

MEHDI SHAHIDEH, B. Eng & Management

A Thesis
Submitted to the School of Graduate Studies
in Partial Fulfillment of the Requirements
for the Degree
Masters of Applied Science

MASTERS OF APPLIED SCIENCE (2004)   MCMASTER UNIVERSITY

                                                                     Hamilton, Ontario

TITLE: Design and Fabrication of Highly Reflective DBRs for use with Long
                Wavelength VCSELs

AUTHOR: Mehdi Shahideh, B. Eng & Management (McMaster University)

SUPERVISOR: Dr. Dave A. Thompson

NUMBER OF PAGES: xi, 98

Abstract

This project successfully designed, fabricated and characterized two highly reflective distributed Bragg reflectors for use with long wavelength vertical cavity surface emitting lasers. The first reflector consisted of 20 pairs of alternating $InP/In_{0.64}Ga_{0.36}As_{0.777}P_{0.223}$ layers grown on an InP substrate with a theoretically predicted normal incident reflectivity of 96.6% at a center wavelength of 1550nm. The second DBR had 20 pairs of alternating $GaAs/In_{0.484}Ga_{0.516}P$ layers grown on a GaAs substrate with a theoretically predicted reflectivity of 94.9% at a center wavelength of 1550nm for normal incident light. Experimental results obtained using a specially designed reflectivity measurement setup confirmed reflectivity models and predictions at both normal and variable incident light angles. However, these measurements revealed a discrepancy between theoretical and experimental layer thickness values for both DBR structures. Applying perturbations to the theoretical models, the actual layer thicknesses of the DBRs were determined. X-ray analysis was employed to examine the periodicity of the super-lattices along with the accuracy of lattice matching to the substrate. Transmission electron microscopy revealed that no detectable drift in layer thickness was apparent during growth of the DBR structures. Photoluminescence was used to investigate any compositional variations of the quaternary layers in the first DBR stack.

*Dedicated to my loving parents and brother for their
never ending love and support. A special heartfelt
thanks to my 'Hamilton' mom and dad for all their
support and advice. Finally, a sincere thank you to all
my friends who taught me the lessons that no
classroom ever will. I will NEVER forget!*

Be like the fountain that over flows, not like one that merely contains.

Table of Contents

List of Figures

List of Tables

1. Introduction

1.1 Background

Reflectors are an essential component to any laser operation. Without them, it would be next to impossible to create enough stimulated emission to achieve 'lasing' in everyday edge emitting semiconductor lasers. The most common form of reflector found in such devices is comprised of a cleaved edge facet (facet coatings usually added) providing at best a reflectivity of 40% [1]. Despite this rather low reflectivity value, the gain media in edge emitting laser devices , as shown schematically in Figure 1.1.1(a), are large enough (typically 0.5-1.0mm in length [1]) to establish lasing with reasonable injection current levels. In the case of vertical cavity surface emitting lasers where the gain medium is only on the order of 240-300Å as shown in Figure 1.1.1(b), a mirror reflectivity of 40% would be inadequate to attain a lasing device. A much higher percentage of the produced light would have to traverse the gain medium several hundred times in order to offset the gain medium size. For example, a 240Å gain medium being reasonably pumped with current yields a gain of about 1% per pass [2]. Thus, if the intent of the laser is to provide 50% of the generated light as useful output power, the output mirror transmission must be about 0.5% and the other losses, including the back mirror transmission, must be about 0.5% as well [3]. This translates into the need for mirrors with reflectivities of higher than 99.5%.

1
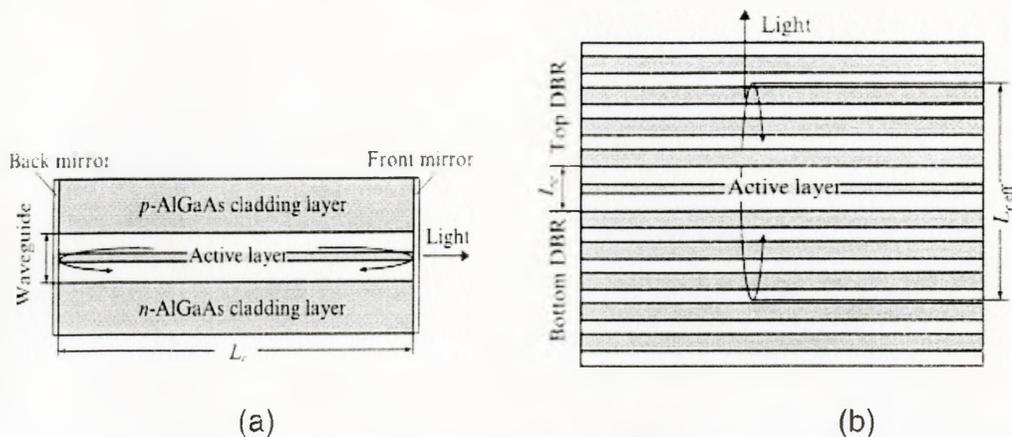
Figure 1.1.1: Cross-sectional diagram of a) edge emitting laser with large gain medium b) VCSEL with small gain medium [4].

With such a challenging problem, it becomes questionable whether the challenges of designing and manufacturing such reflectors for VCSELs are even worth the trouble. The answer is simply yes. VCSELs have quite a number of advantages over conventional edge emitting lasers making them a desirable commodity. Their vertical design results in ease of manufacturability by eliminating multiple lithography and etching steps. Furthermore, their typical 3-8µm device diameter permits larger laser yields per processed wafer [5]. An added bonus to reducing manufacturing costs arises due to the fact that light exits the top of the devices. Consequently, devices may be tested and characterized after production without the need to extensively handle the wafer or cleave a single device out for testing as is the case with edge emitters.

In addition to manufacturability features, VCSELs also have other attractive characteristics. Their circular shape translates into a low numerical aperture output beam making fiber coupling effortless. Furthermore, their high power conversion efficiency in the low power range makes them perfect for highly integrated circuits as heating issues are resolved [2]. Finally, their vertical emission and growth method allows for the manufacturing of 2-dimensional arrays, perfect for display applications or optical switching. A scanning electron microscope image of a VCSEL is provided in Figure 1.1.2.
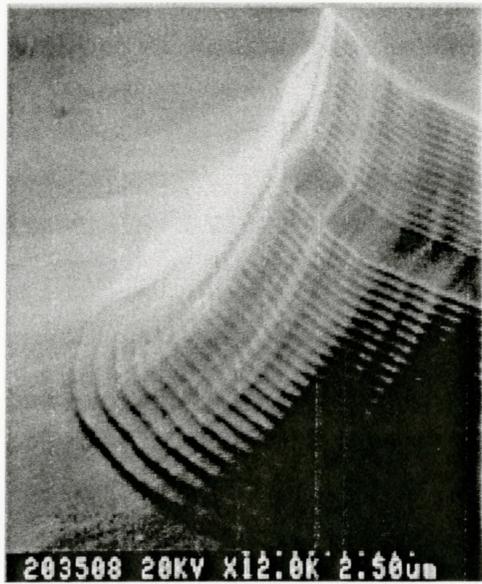
Figure 1.1.2: SEM image of VCSEL [6].

Clearly VCSELs are of great interest as discussed above. However, the demanding requirements of the reflectors have limited their application. Initially, various types of reflectors were conceived to suit an assortment of VCSEL design criteria. These reflectors can typically be divided into four main categories. These include metallic reflectors, distributed Bragg reflectors (DBR), hybrid metal-DBR reflectors, and reflectors based on total internal reflection [2]. Figure 1.1.3 depicts these four categories of reflectors.

Metallic	DBR	Hybrid	TIR
R = 80-99%	R < 100%	R < 100%	R = 100%
T = 0%	T = 1-R	T = 0%	T = 0%
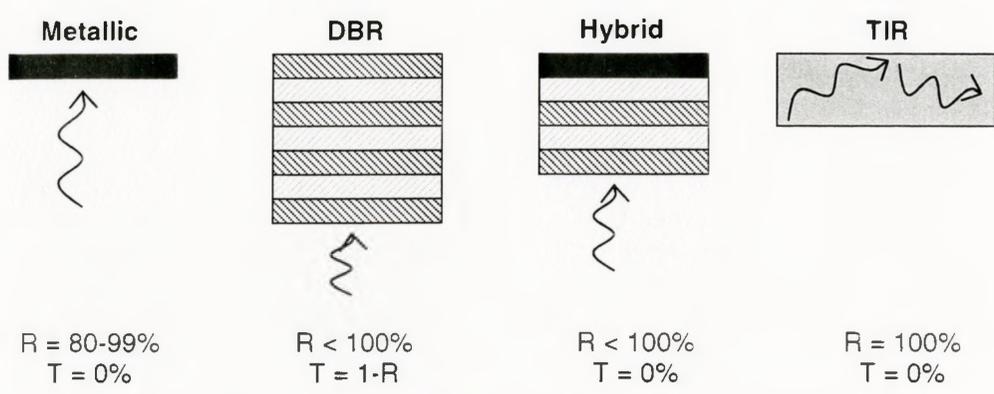
Figure 1.1.3: Schematic illustration of different types of reflectors.

Metallic and hybrid reflectors are highly reflective and thus commonly used in VCSELs. They also have the advantage of possessing a larger electric and thermal conductivity relative to other reflectors. These reflectors are, however, restricted to use only on the non-light exiting side of the VCSEL due their absorbing nature.

Total internal reflection (TIR) reflectors are of little use to VCSEL applications. They do possess a reflectivity of 100% yet in order for this to be realized, the incident light angle must meet the TIR condition determined by Snell's Law. These conditions are next to impossible to control with the light originating from stimulated emission in such a small active region.

This leaves distributed Bragg reflectors as the only remaining choice for VCSELs. DBRs consist of periodic quarter-wave stacks of low and high refractive index compound semiconductors. A DBR can be designed to have a reflectivity just below 100% with the capability to transmit the portion of light that is not reflected. In addition, if designed correctly, DBRs can be epitaxially grown directly onto the active region or vice-versa eliminating the need for complicated and messy bonding techniques such as fusion bonding. As a result, they are the ideal candidate and hence the most actively investigated solution to the reflector dilemma facing long wavelength VCSELs.

1.2 Motivation

The performance of VCSELs is often limited by the availability and quality of distributed Bragg reflectors. Successful GaAs based VCSELs in the 0.8-1.0μm wavelength range have characteristics comparable to, or better than, those of edge emitters in the lower power (~1mW) regime [2]. While successful devices have been fabricated in the infrared wavelength range (~860-980nm), operation at wavelengths greater than 1.3μm has been problematic [7].

The major obstacle for fabricating long wavelength VCSELs is the difficulty in manufacturing suitable DBRs with the commonly used compounds such as InGaAs,

InGaAsP, and InP. To overcome this issue, many research groups have begun to incorporate various antimonide and aluminum compounds to achieve highly reflective DBRs at long wavelengths. Despite the fact that this has proven to be promising, long wavelength VCSELs are still behind in performance of present day 850nm VCSELs, and long wavelength edge emitting devices. Table 1.2 summarizes some of the latest devices and their specifications.

Table 1.2: Summary of latest VCSELs designs [8].

Approach	Op.	λ (nm)	Temp. (°C)	Power (mW)	Threshold Current (mA)	Threshold Voltage (V)
Metamorphic DBR	CW	1550	15	1.40	2.30	1.70
InP/air gap DBR	CW	1550	25	1.00	0.70	
GaAs Sb DBR	CW	1565	25	0.90	0.80	1.40
InAlGaAs QW + dielectric DBR	CW	1550	20	0.72	0.40	0.90
InP/air gap DBR	CW	1304	25	1.60	0.70	
GaInNAs QW	CW	1307	25	1.00	2.20	2.00
GaInNAsSb QW	CW	1300	20	1.00		1.20

Clearly, long wavelength VCSELs have exhibited tremendous progress since their conception in 1979 [3]. This progress has been a result of developments in materials growth technology, as well as innovation in device design and fabrication. The knowledge gained in studying high reflective DBRs continues to greatly contribute to the steeper learning and development curve of VCSELs. This thesis will attempt to complement current research pertaining to the field of DBRs and provide a stepping stone for future researchers at McMaster University wishing to enter this exciting, dynamic and challenging field.

1.3 Organization of the Thesis

This work for the most part provides the essential steps for design, fabrication, and characterization of distributed Bragg reflectors for use with vertical cavity surface emitting lasers. An experimental setup was designed and assembled to measure the wavelength and angle of incidence dependence of the reflectivity of DBR reflectors.

Tests were carried out on InGaAsP/InP and InGaP/GaAs DBRs. This experimental setup is discussed in chapter 2.

Chapter 3 mostly pertains to the design and modeling aspects of DBRs. Design requirements, materials selection, refractive index calculations, as well as considerations for stack sizes are examined. The remaining chapters of this work present and discuss the experimental findings in regard to the DBR stacks designed for this thesis. These results are analyzed and compared to theoretical calculations in order to verify their validity. The thesis finally concludes by discussing future possibilities for research, providing several directions.

2. Experimental Setup

2.1 Introduction

The concept of obtaining the reflectivity of any given material is rather straightforward. First off, a light source of given wavelength and power is directed onto the sample at a specified incident angle. Thereafter, a measurement must be made of the power of light reflected or transmitted by the sample. For this project, it is preferred to measure the reflected beam rather than the transmitted beam. This is largely due to the fact that the region of interest is a thin film structure that lies close to the surface and is highly reflective (80% or greater reflectively). In addition it is grown on a thick substrate where absorption losses may become significant. Both these aspects translate into minimal light being transmitted thus making the measurement much more difficult and more prone to errors. This however, does not imply that measuring the reflected power is without its challenges and these will be fully discussed in a later section.

Once the reflected or transmitted power is measured, some rudimentary algebra is performed to obtain the reflectivity of the sample as demonstrated by the equations below.

$$reflectivity = \frac{power_{reflected}}{power_{incident}} \cdot 100\% \qquad (2.1)$$

$$reflectivity = \frac{1 - power_{transmitted}}{power_{incident}} \cdot 100\% \qquad (2.2)$$

7

Given that the reflectivity is determined by taking a ratio of the incident and reflected/transmitted light, it is most critical that the measurements are carried out in a manner that minimizes and allows for keeping track of any optical power loss while the light is propagating through the experimental setup.

2.2 System Requirements & Components

To adequately acquire all of the necessary measurements deemed essential for designing and testing high reflectivity mirrors, an experimental setup was required that would enable measurements to be taken at a variety of incident angles, power levels, and wavelengths. An HP 8168E tunable laser source equipped with a grin lens fiber output was used as the light source. This features a maximum output power of 3mW at its central wavelength region (1500nm to 1520nm) with an operational output spectrum ranging from 1470nm to 1580nm [9]. Despite the fact that the tunable range is quite impressive, an even larger range would have been desirable in order to fully view the mirror stop bands and lateral characteristics. The grin lens satisfactorily allowed for light collimation with negligible divergence over the design distances.

Because of various design limitations, two different measurement systems were contrived. One geometry was used for normal incidence light measurements and another for variable incident light angles. Each setup had different physical detecting requirements and therefore an assortment of detectors were required and the different setups are discussed in 2.3 and 2.4. The detector outputs were then amplified using a Stanford Scientific SR810 Lock-In Amplifier which significantly reduces inherent background noise.

2.3 Normal Incidence Experimental Setup

The design concept for this setup was inspired by a paper on the subject of in situ reflectance monitoring during epitaxial growth [10]. The collimated laser output is passed through a beam splitter which divides the beam into two parts. One part passes through the beam splitter and is incident on the sample surface where it is reflected back to the beam splitter which directs the reflected beam to a detector. The other part of the beam is directed to a second detector which is used to monitor the laser output power. Figure 2.3.1 below illustrates the experimental setup.
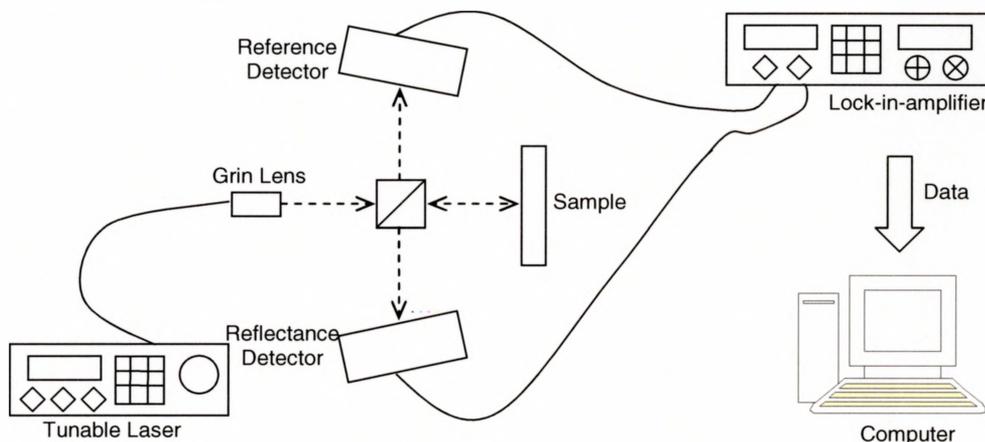
Figure 2.3.1: Normal incidence experimental setup.

It is important to note that the combined path length that the light traverses from the moment it leaves the grin lens until its detection by the detector is roughly 7cm. This ensures that the beam divergence, which is < 0.25° degrees/cm, does not result in a final spot size larger than the detector surface area [11]. A program written in LabView coordinated and recorded the measurement process. This was accomplished by having the laser wavelength remotely altered in defined increments while simultaneously recording the detector readings through the lock-in amplifier.

Two identical detectors (HP IR818 optical detector heads with diffusive covers) were used to measure both reference and reflected beams with their output passed through the dual channel lock-in amplifier. The detector heads were aligned slightly off perpendicular to the incident light (refer to Figure 2.3.1) to eliminate oscillations in the collected data as a result of back reflections.

The initial task was to calibrate both detectors to determine their individual characteristics. This was accomplished by a series of tests whereby the laser power and wavelength were varied as the incident beam was directed onto each individual detector. Typical results of these analyses are summarized Figures 2.3.2, 2.3.3, 2.3.4.

Detector Output Versus Laser Output Power
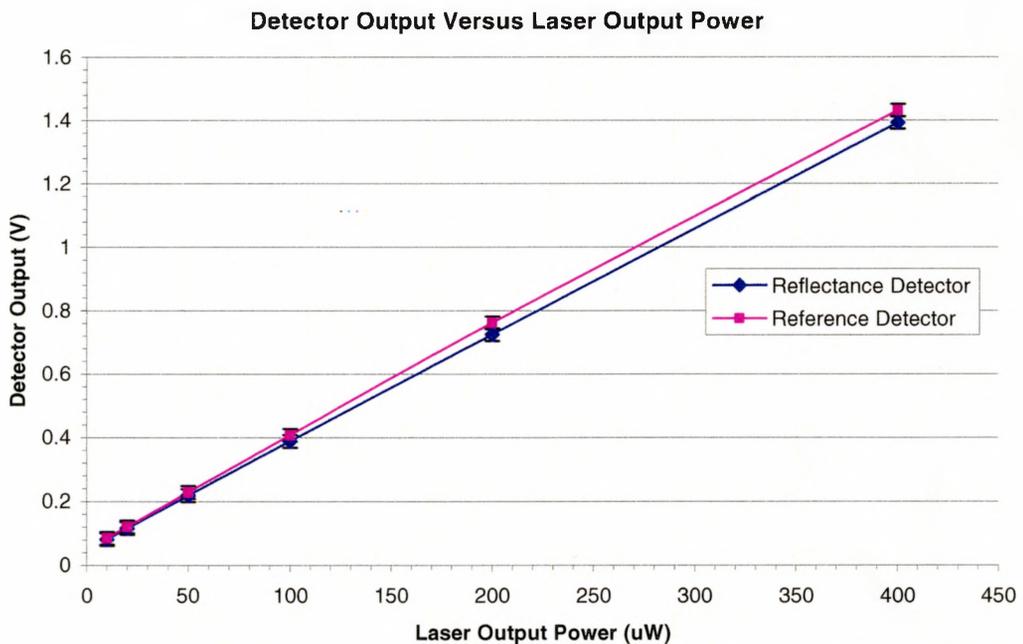
Figure 2.3.2: Plot displaying linear power response of both detectors at 1550nm.

Detector Output Versus Incident Wavelength
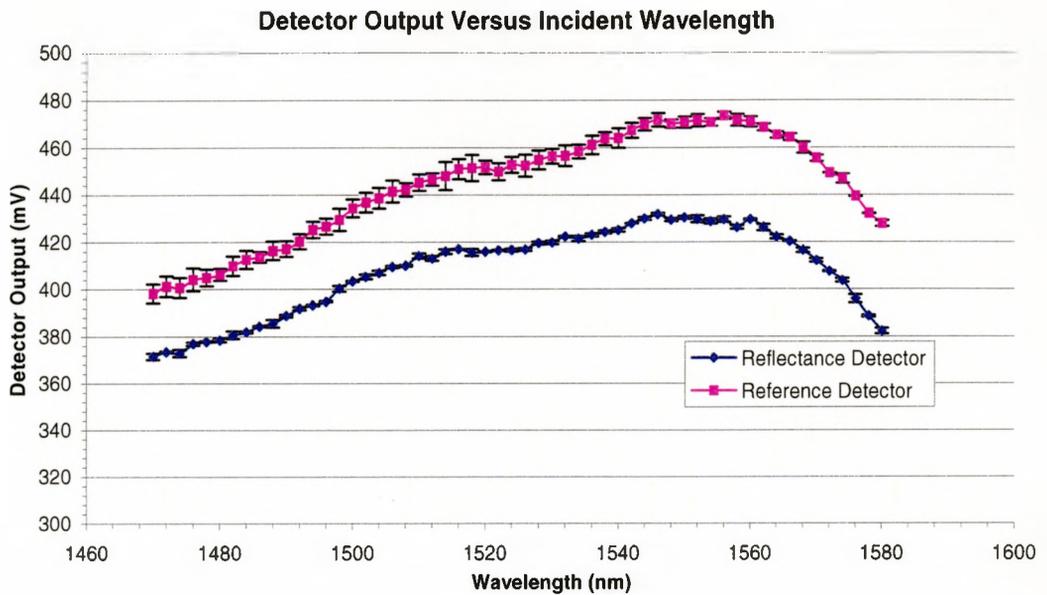
Figure 2.3.3: Typical wavelength dependence of both detectors shown for a fixed laser output power of 100μW.

Detector Power Difference Versus Wavelength
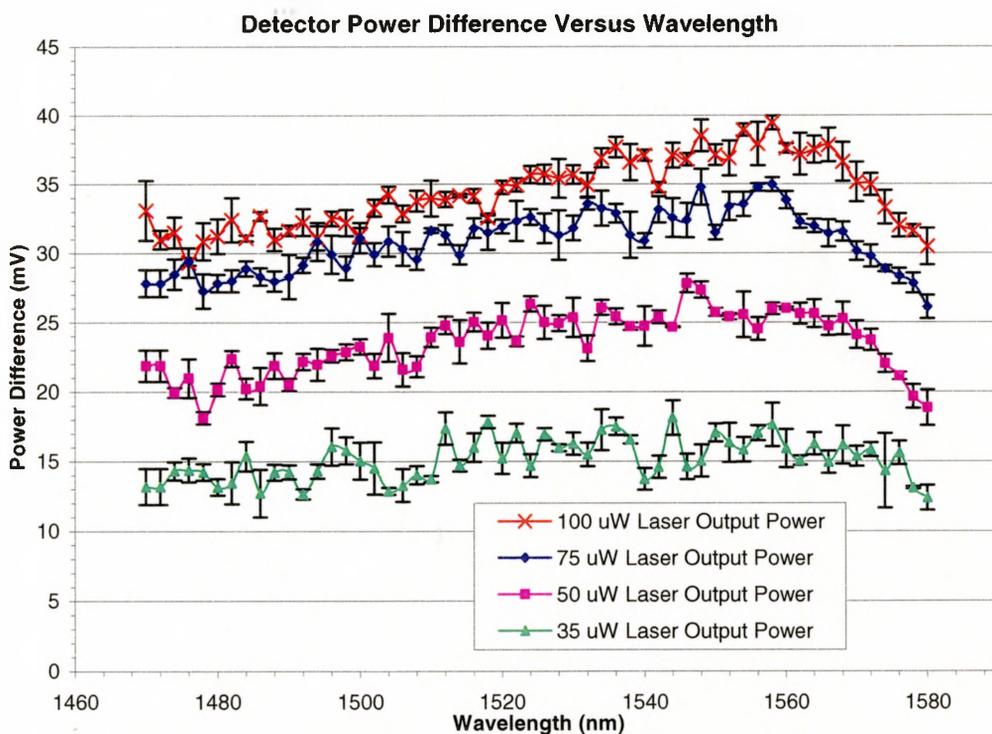
Figure 2.3.4: Varied laser output power and the resultant power difference between detector outputs.

Figure 2.3.2 confirmed that both detectors were operating well within their linear range. From data in Figures 2.3.3 and 2.3.4, it was determined that the power difference in readings between detectors was constant at each wavelength but varied with different power levels due to detector characteristics. Therefore, in order to compare readings between the two detectors, an addition/subtraction would have to be made to either detector reading for reliable results.

The beam splitter utilized in this arrangement was specified as a true 50/50 beam splitter over the wavelength operational window. However, when the reflectance detector was placed in the position of the sample in order to confirm this specification, it was determined that not only did the beam splitter lack true 50/50 properties, it also had a roughly 10% loss coefficient throughout the spectral window of operation. The results of beam splitter properties are evident in Figures 2.3.5 and 2.3.6.
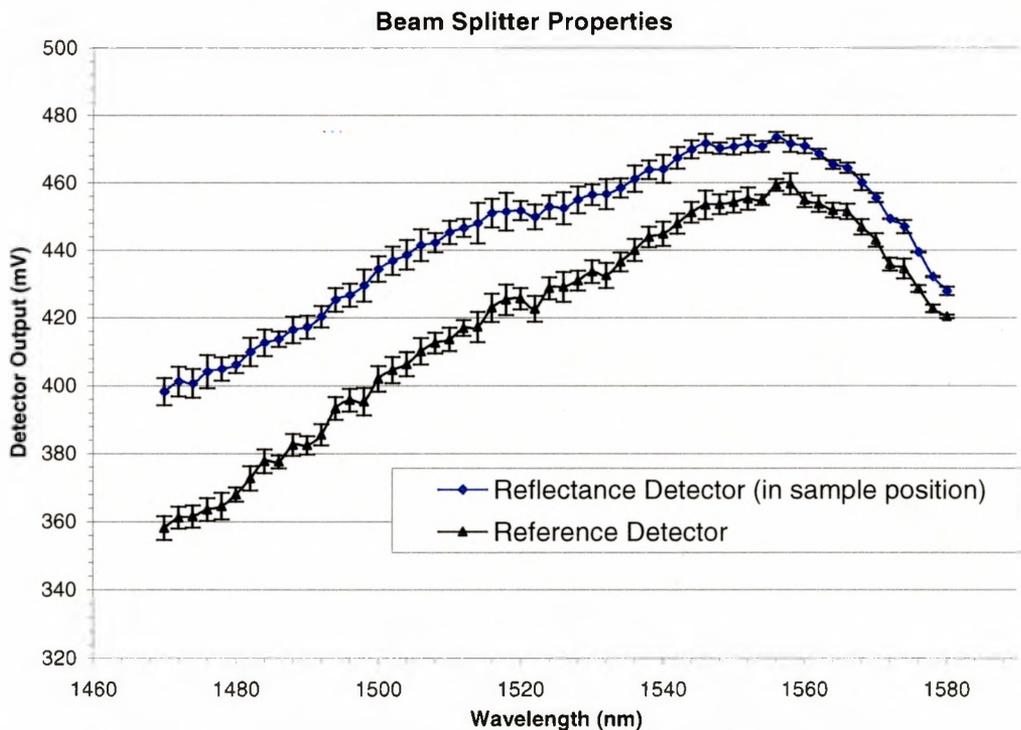
Figure 2.3.5: Plot portraying the beam splitting properties of the cube over the laser operating spectrum at 100μW output power.

Inherent Absorption in Beam Splitter Cube
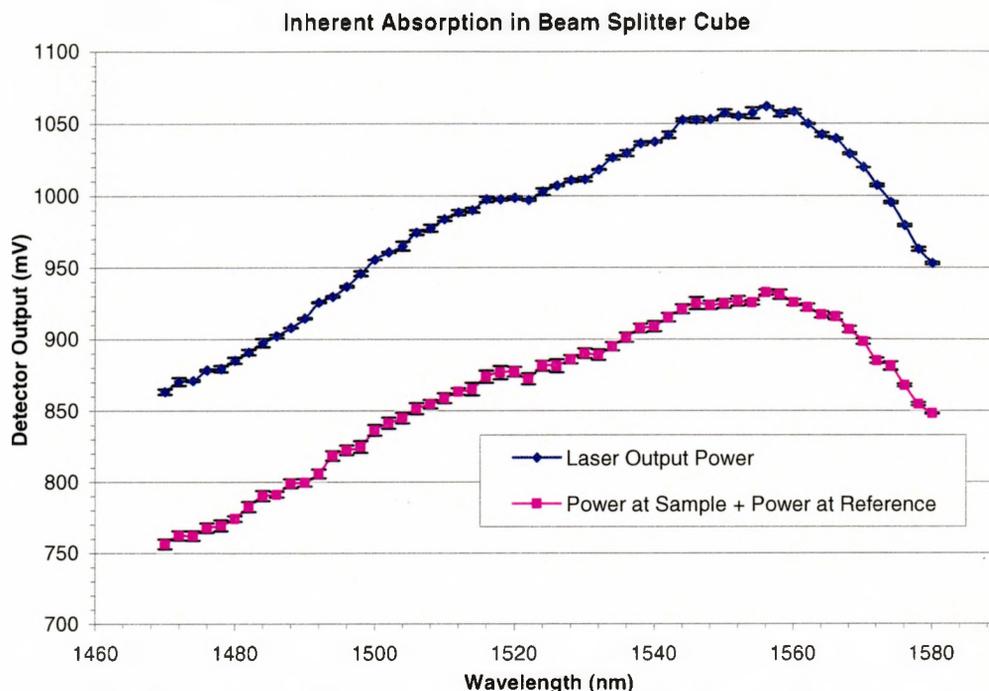
Figure 2.3.6: The two curves clearly reveal the presence of some type of loss in the beam splitter.

The data in Figure 2.3.5 is the result of placing one detector in the sample position while the other was kept in the reference position. In order to compare the values of the two detectors, an addition or subtraction step is required due to the inherent differences in the detectors.

The data in Figure 2.3.6 was obtained by comparing light measurements made post and prior to the beam splitter. The laser output power was measured directly by a detector and recorded. Noting the law of conservation of energy, the sum of the detector outputs at the sample and at the reference positions must then add up to the total detector output power prior to the beam splitter. This is clearly not the case as can be seen in Figure 2.3.6. This discrepancy was attributed to loss in the beam splitter cube.

In order to obtain accurate reflectivity results, the detector differences and effects of the beam splitter had to be taken into account. The loss within the cube was modeled following the schematic shown in Figure 2.3.7. P_o is the output power from the grin lens,

the power of the transmitted and reflected beams from the cube are denoted P_t and P_r respectively, with P_d being the final power at detector. These are all values that are acquired during the experiment. Additional variables included α as the absorption coefficient, L for the length of the cube, R for the back reflection off each face of the cube (extremely small value due to antireflection coatings), and finally S_t and S_r for the fraction of light transmitted and reflected respectively by the beam splitter.
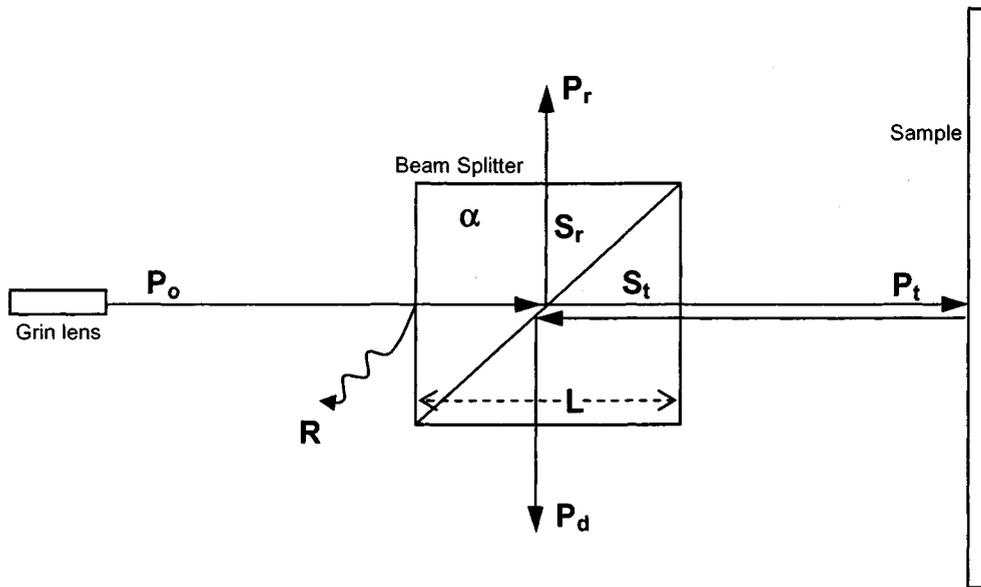
Figure 2.3.7: Illustration of variable assignments to beam splitter model.

The following three equations were formulated to model the absorption.

$$S_t + S_r = 1 \tag{2.3}$$

$$P_t = P_o \cdot R^2 \cdot e^{-\alpha \cdot L} \cdot S_t \tag{2.4}$$

$$P_r = P_o \cdot R^2 \cdot e^{-\alpha \cdot L} \cdot S_r \tag{2.5}$$

By substituting Equation 2.3 into Equation 2.4 and summing the resultant equation with Equation 2.5, it then became trivial to solve for the absorption coefficient as shown in Equation 2.6.

$$\alpha = \frac{-1}{L} \cdot \ln\left(\frac{P_t + P_r}{P_o \cdot R^2}\right)$$ (2.6)

With the absorption of the cube determined, the beam splitting ratios were then modeled. This was accomplished by using Equation 2.3 in conjunction with the following relationship.

$$\frac{S_r}{S_t} \approx 1 \approx \frac{P_r}{P_t}$$ (2.7)

By substituting Equation 2.3 into Equation 2.7, two equations can be derived that provides a numerical value for the percentage of light transmitted and reflected by the cube. Thus, any unequal beam splitting can then be accounted for by the model.

$$S_t = \frac{P_t}{(P_r + P_t)}$$ (2.8)

$$S_r = 1 - \frac{P_t}{(P_r + P_t)}$$ (2.9)

With all the necessary adjustments made, the experimental setup for the normal incidence scenario was then completed for use.

2.4 Variable Incidence Experimental Setup

The variable incidence setup required a great deal more thought than that of the normal incidence. The design had to meet the following criteria; assuming that the light source and detector are at the same point, if the sample is rotated by θ, then the detector would have to rotate by 2θ in order to capture the reflection. Figure 2.4.1 below depicts this relation.
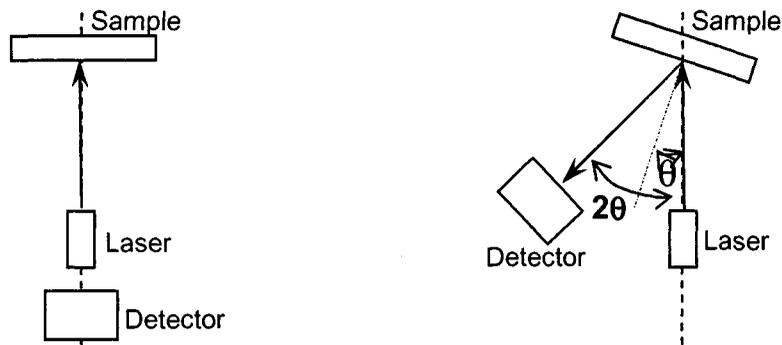
Figure 2.4.1: θ and 2θ relation.

It was resolved that in order to simplify alignment issues and prevent damage to the grin lens and/or the optical fiber, the laser source should remain stationary while the sample and sole detector would rotate. This was accomplished by literally stacking the two motorized rotation stages on top of one another with the addition of an aluminum bracket designed to make this possible. The bracket also provided a housing for the sample mount.

The lower rotation stage was fixed to an optical table with the aluminum bracket screwed to it. The second rotation stage was then screwed atop the bracket and fitted with an extendable arm designed to hold the detector (Figure 2.4.2). With the described system, it then became possible to rotate the sample and detector while maintaining the required θ-2θ relation. Figure 2.4.3 illustrates the entire apparatus.
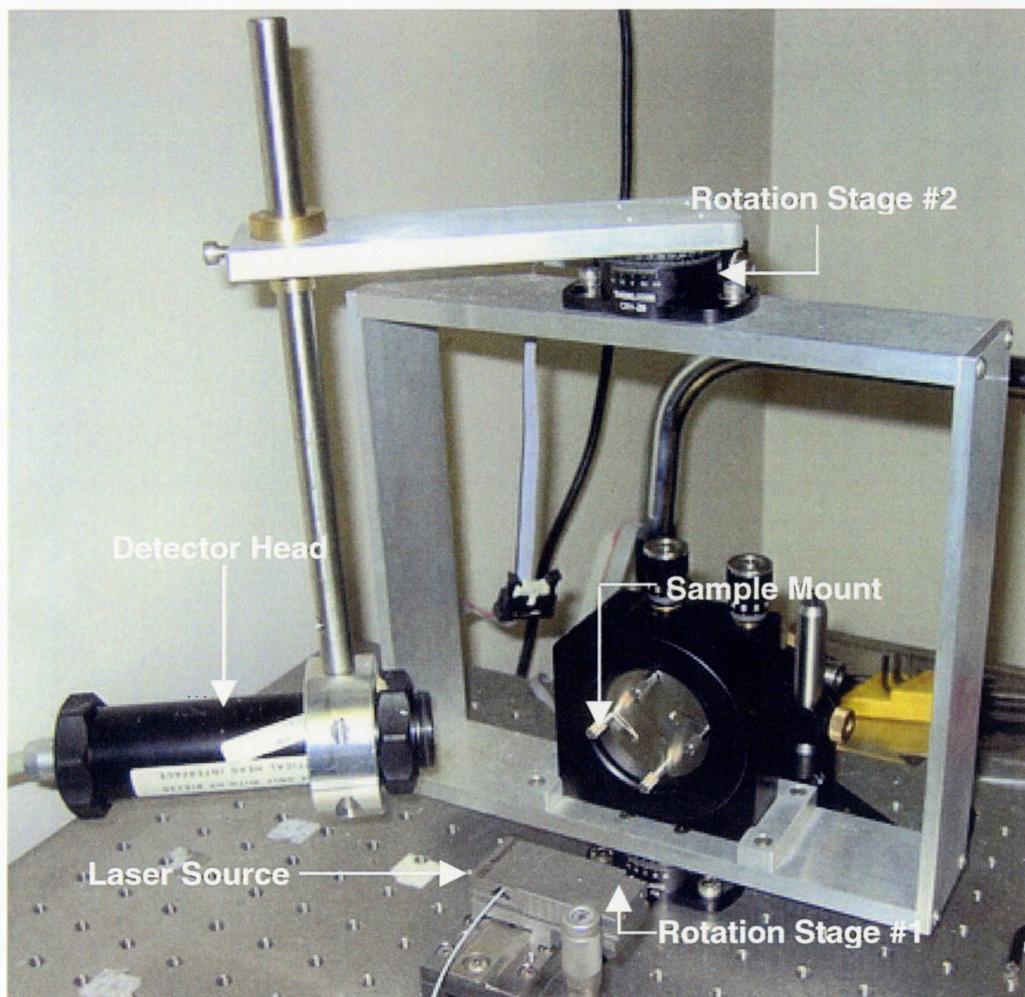
Figure 2.4.2: Rotation stage apperatus.
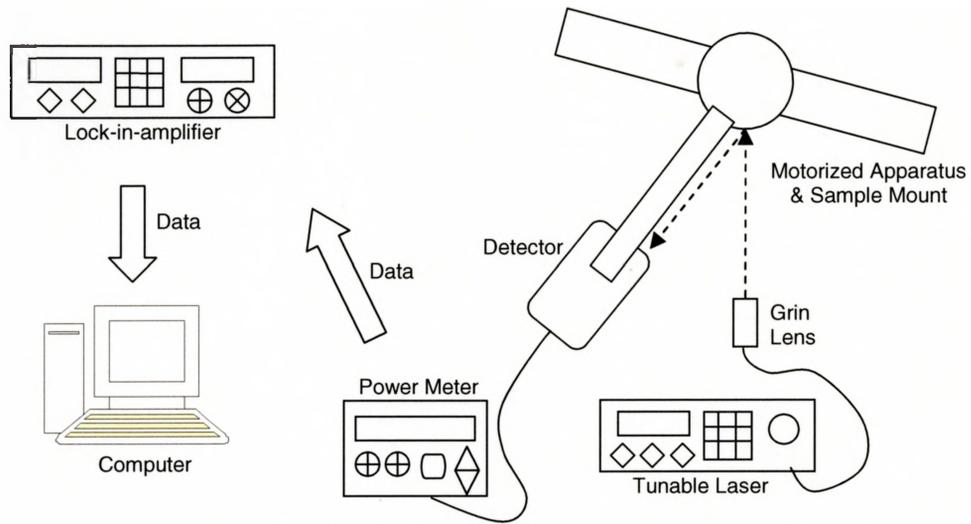
Figure 2.4.3: Variable incidence experimental setup.

Similar to the normal incidence setup, the variable angle setup is also computer controlled via a LabView program. The program provides the user with angle selection (ranging from 6° degrees to 54° degrees due to physical apparatus constraints), laser output power, wavelength selection and step size. Data acquisition was also provided.

An added advantage of this setup was the elimination of the beam splitter and the requirement of only a single detector. The detector of choice was an HP 81525A optical head (operational range of 800-1600nm) used with the HP 8153A Lightwave optical power meter. The output of the power meter was then fed into the Stanford Scientific SR810 Lock-In Amplifier for noise reduction. The HP detector head was an excellent choice due to its large detection surface area making alignment somewhat trouble-free.

It is important to note that with this setup no mathematical modeling was required simply due to the simplicity of operation. The laser power was measured through all wavelengths at the sample surface. The sample was then exposed to the laser and its reflection measured thus eliminating all the extra work required by the normal incident setup.

3. Modeling of High Reflectivity Distributed Bragg Reflectors (DBRs)

3.1 Design Requirements

DBRs that are to be designed for use in vertical cavity surface emitting lasers (VCSELs) have several design requirements. The first and most obvious is the need to be extremely reflective and transparent (preferably higher than 98% reflective) at a required wavelength. Next, the DBRs must contain as few layers as necessary in order to reduce production costs through ease of growth, material consumption, and time. Furthermore, this would reduce the possibility of compositional and growth rate drifts that would affect the device performance. Finally, the DBR stack must be conductive both electrically and thermally in order to allow current injection into the active region of the device. Figure 3.1.1 depicts a cross-sectional diagram of a typical VCSEL.

M.A.Sc. Thesis – M. Shahideh. McMaster – Engineering Physics

20
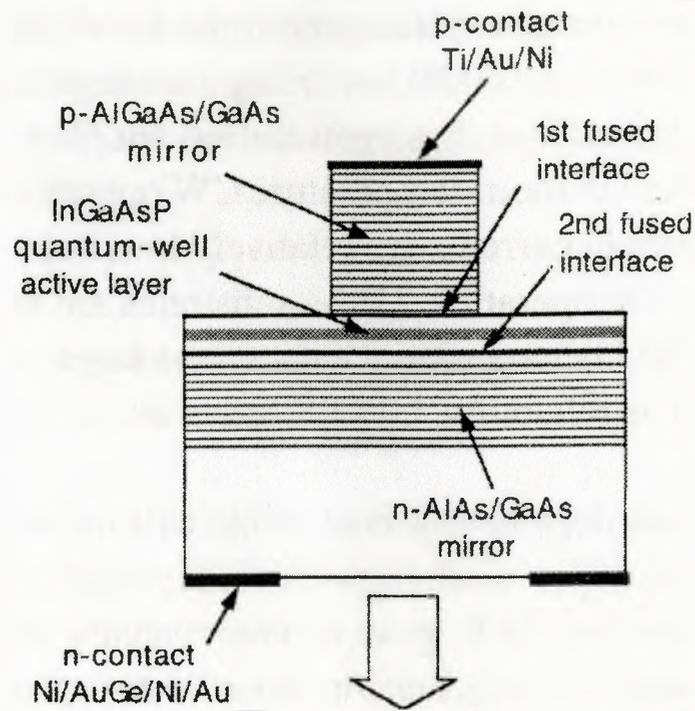
Figure 3.1.1: Cross-section diagram of a 1.55μm wavelength VCSEL with fused AlGaAs/GaAs mirrors [12].

All of these design requirements can be met by constructing a DBR stack with the appropriate material composition. To achieve the first two requirements (the goal of this thesis), the materials for each pair in the stack should be selected such that the difference in the index of refraction between the two layers is as large as possible with the layer thicknesses satisfying the Bragg quarter-wave condition (Equation 3.1 below) [13].

$$L_{(1,2)} = \frac{\lambda_{Bragg}}{4 \cdot n_{(1,2)}}$$

(3.1)

where L is the layer thickness, λ_{Bragg} is the Bragg wavelength of operation, and n is the refractive index of the layer. Once the layer compositions and thicknesses for the two layers are determined, the number of pairs then required to achieve the desired reflectivity needs to be determined. The optical field incident on the DBRs penetrates into the reflector by a finite number of quarter-wave pairs as seen in Figure 3.1.2. The

number required to achieve the desired reflections is entirely dependent on the magnitude of the difference between the index of refraction for both material layers. The larger the difference, the fewer layers are required.
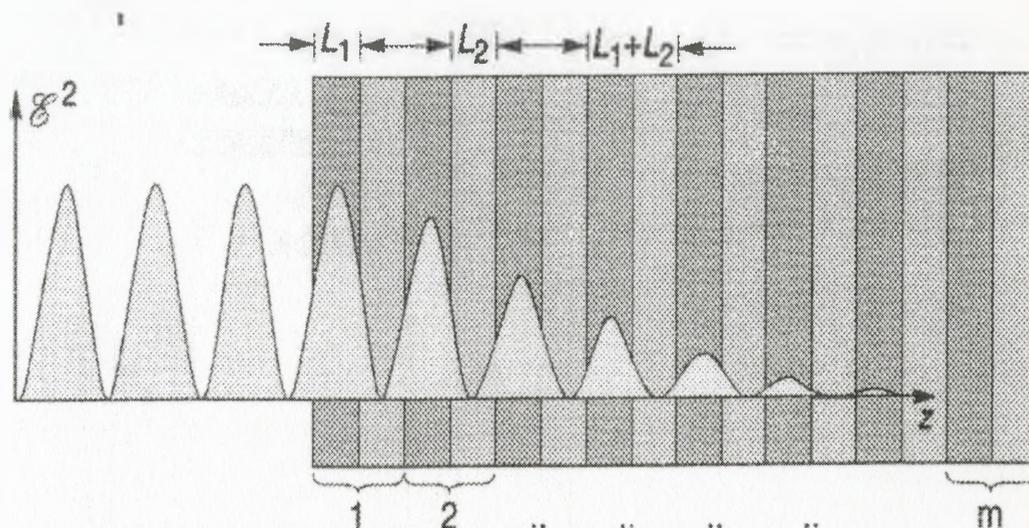
Figure 3.1.2: Illustration of the DBR penetration depth consisting of two materials of thickness L_1 and L_2 [3].

Another difficulty that arises in material selection comes about because the band gap of the selected materials must be larger than the energy of the incident light to avoid absorption. Consequently, when designing DBR stacks at the 1.55μm range, the available materials are quite limited. Table 3.1 provides a summary of some available materials and their respective indices.

Table 3.1: A summary of refractive index values for DBR mirrors tuned at 1550nm. Percentages at the row-column crossings correspond to $\Delta n/n_{average}$.[a]

Low Index →		AlAs	$Al_{67}Ga_{33}As$	$AlAs_{56}Sb_{44}$	$AlP_{0.4}Sb_{0.6}$	$Al_{48}In_{52}As$	InP
High Index ↓	n	2.89	3.04	3.10	3.05	3.21	3.17
GaAs	3.37	15%	10.3%	-	-	-	-
InGaAsP[b]	3.45	-	-	10.7%	12.3%	7.2%	8.5%
AlInGaAs[b]	3.47	-	-	11.3%	12.9%	7.8%	9%
AlGaAsSb[b]	3.6	-	-	15%	16.5%	-	-
AlGaPSb[b]	3.55	-	-	13.5%	15.2%	-	-

[a] Data has been accumulated from Refs. [14, 15, 16, 17,18].

[b] Band gap wavelength ≈ 1400nm.

An additional consideration for designing the mirror stacks arises when the light output covers a broad spectral range or when the laser source is tunable. In such a scenario, the importance of the stop band becomes very crucial. The stop band of the mirror refers to the spectral width over which the mirror maintains its intended high reflectivity. Figure 3.1.3 illustrates a typical DBR response showing the stop band.
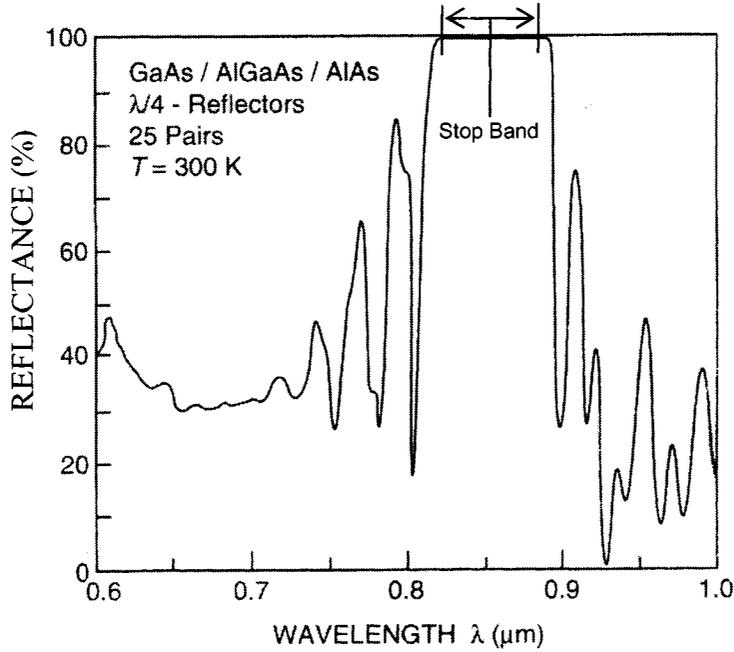
Figure 3.1.3: Reflectance of an AlGaAs/AlAs DBR with 25 pairs [3].

The spectral width of the stop band is given by [19]

$$\Delta\lambda_{stopband} = \frac{2 \cdot \lambda_{Bragg} \cdot \Delta n}{\pi \cdot n_{eff}} \tag{3.2}$$

where λ_{Bragg} is the Bragg wavelength, Δn is the difference in refractive index of the two layers, and n_{eff} is the effective refractive index. The effective refractive index is given by [19]

$$n_{eff} = 2 \cdot \left(\frac{1}{n_1} + \frac{1}{n_2} \right)^{-1} \tag{3.3}$$

With all these design requirements in mind, the next step is to model and materials in order to fabricate a functioning DBR stack operational at 1.55μm.

3.2 Material Selection

As previously stated, material selection is crucial to the functionality and practicality of the DBR stack. Thus, many considerations must be made prior to manufacturing. One such consideration is the growth facility available to manufacture the desired stack. At McMaster University, there are currently two molecular beam epitaxy (MBE) units allowing for the growth of a multitude of materials. At present, however, only one of the two units is operational thus limiting material compositions to the InGaAsP family base. Consequently, the material selection and composition are quite limited for the design of a DBR stack at the desired operational wavelength of 1.55μm.

Keeping the design requirements in mind and referring to Figure 3.2.1, it becomes evident that in order to grow a stack with minimal strain and a band gap no smaller than 0.9eV (in order to safely avoid absorption by a comfortable margin), an InP or GaAs substrate is essential. For the first sample grown, an InP substrate was selected. With the substrate determined, all that remained was the selection of the materials for the two layers that would constitute the DBR stack. Referring to Table 3.1 while observing the growth restrictions, it becomes clear that InP and InGaAsP are the only two materials that meet the design requirements. The factor remaining was to select the growth composition of the quaternary structure.

M.A.Sc. Thesis – M. Shahideh. McMaster – Engineering Physics

24
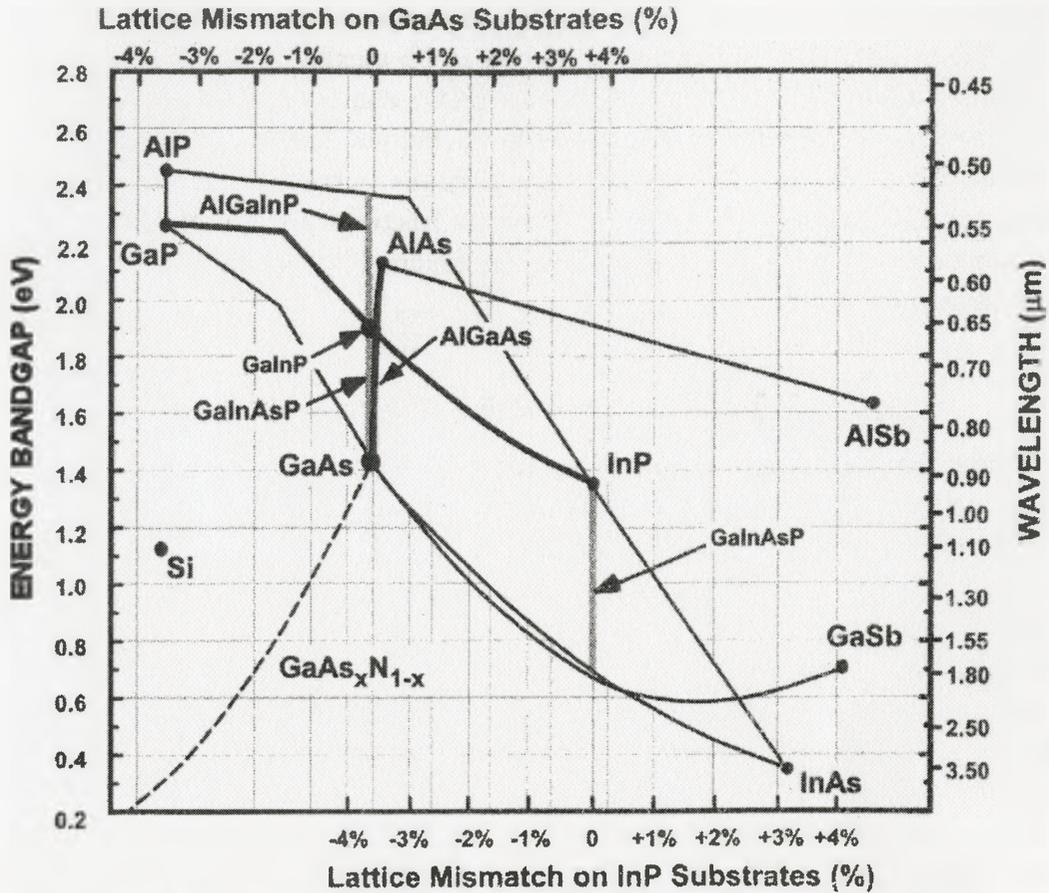
Figure 3.2.1: A plot of the dependence of band gap energy (emission wavelength) on lattice mismatch relative to GaAs and InP substrates [3].

The composition of the quaternary $Ga_xIn_{1-x}P_yAs_{1-y}$ had to satisfy three basic requirements; a) to have a band gap equal to or larger than 0.9eV b) be lattice matched to InP c) possess the largest index of refraction possible at 1.55μm. An interpolation scheme was used to calculate the quaternary alloy energy band gap as a function of alloy composition ($0 \le x \le 1$, $0 \le y \le 1$). For an $A_xB_{1-x}C_yD_{1-y}$ quaternary type alloy, the energy band gap is obtained by the following [20]

$$E_g(x,y) = \frac{(x(1-x)[(1-y)E_{ABD}(x) + yE_{ABC}(x)] + y(1-y)[(1-x)E_{BCD}(y) + xE_{ACD}(y)]}{[x(1-x) + y(1-y)]}$$

(3.4)

where E_{ABC}, E_{ABD}, E_{BCD}, and E_{ACD} are the ternary alloy energy band gaps containing the corresponding bowing parameters. The lattice matching relationship between x and y in the quaternary to the InP substrate were met by using the following relationship [21]

$$y = \frac{(0.189 - 0.405 \cdot x)}{(0.189 + 0.013 \cdot x)} \tag{3.5}$$

A full account of these band gap calculations can be found in Appendix 7.1. It is important to note that values such as bowing parameters, binary and ternary energy gap values, etc. were all obtained from a single source (Reference [20]) in order to ensure some level of consistency in the final calculations.

With the equations and all the variable values gathered, a MathCAD program was written to simplify the arithmetic required to obtain the band gap energy. A target band gap of 0.90eV was set and through an iteration process, various x values were employed until the desired result was obtained. According to the theoretical calculations, the following quaternary composition would yield the desired 0.90eV band gap while successfully lattice matching to the InP substrate.

$$Ga_{0.36}In_{0.64}P_{0.223}As_{0.777}$$

The second sample that was grown by the MBE was based on a GaAs substrate with alternating pairs consisting of GaAs and $Ga_xIn_{1-x}P$. Once again, the same criteria as for the first sample had to apply. Thus similar calculations were carried out in order to determine a lattice matching composition for the ternary structure with a band gap larger than 0.9eV. The lattice matching condition for the ternary was found to be (using Vegard's Law)

$$y = \frac{(0.405 - 0.405 \cdot x)}{(0.1895 + 0.0126 \cdot x)} \tag{3.6}$$

with the energy band gap given by Equations 3.4 and 3.5. A full account of these calculations can be found in Appendix 7.2. The calculations yielded a latticed matched ternary composition with a band gap of 1.896eV to the GaAs substrate of

$$Ga_{0.516}In_{0.484}P$$
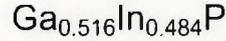
3.3 Index Modeling

In order to determine the refractive index of the quaternary and ternary compounds of the last section with any given compositions, the primary equation utilized was [8]

$$n = \sqrt{A\left[f(x_o) + 0.5 \cdot \left(\frac{E_o}{E_o + \Delta_o} \right)^{1.5} \cdot f(x_{os}) \right] + B} \qquad (3.7)$$

where

$$f(x_o) = x_o^{-2} \cdot \left(2 - \sqrt{1 + x_o} - \sqrt{1 - x_o} \right)$$
$$f(x_{os}) = x_{os}^{-2} \cdot \left(2 - \sqrt{1 + x_{os}} - \sqrt{1 - x_{os}} \right) \qquad (3.8)$$

where

$$x_o = \frac{\hbar \cdot \omega}{E_o} \qquad\qquad x_{os} = \frac{\hbar \cdot \omega}{\left(E_o + \Delta_o \right)} \qquad (3.9)$$

and E_o is the band gap energy of the material at the designed center wavelength, Δ_o is the split band energy, and ω is the angular frequency.

It is important to note that the above equation is valid only for quaternary or ternary materials where the incident photon energies are below the direct band gap E_o. A sample set of calculations can be found in Appendix 7.3. Once again, all variable values were obtained from the same source (Reference [20]) to ensure consistency in the calculations.

The index of refraction for the $Ga_{0.36}In_{0.64}P_{0.223}As_{0.777}$ quaternary at 1.55μm was calculated to be 3.474. In order to verify this result, a literature search was conducted in an attempt to find the index of a quaternary with a similar composition. A quaternary was found with composition $Ga_{0.36}In_{0.64}P_{0.21}As_{0.79}$ where the band gap was calculated to

be 0.90eV with a refractive index of 3.48 at 1.55µm [21]. This finding for the most part confirmed the calculations performed here.

The index of refraction for the ternary composition of $Ga_{0.561}In_{0.484}P$ at 1.55µm was calculated to be 3.131. This value was confirmed through a curve fit using experimental results found in a recent paper [21].

Since the experimental setup for making reflectivity measurements used a laser over a tunable wavelength range of 1480-1580nm, one additional note worth mentioning is that because the index changes with respect to wavelength, the theoretical refractive index was calculated over this entire range for both samples.

3.4 Reflectivity Modeling

The aim of this project was to design and fabricate a highly reflective DBR stack at a specified wavelength. Consequently, the reflectivity modeling is the most crucial segment for design considerations. Due to the multilayer stack design of alternating high-low index layers, a transfer matrix approach was utilized. This method allows for the analysis of the propagating light through each individual layer of the stack making it quite a useful tool.
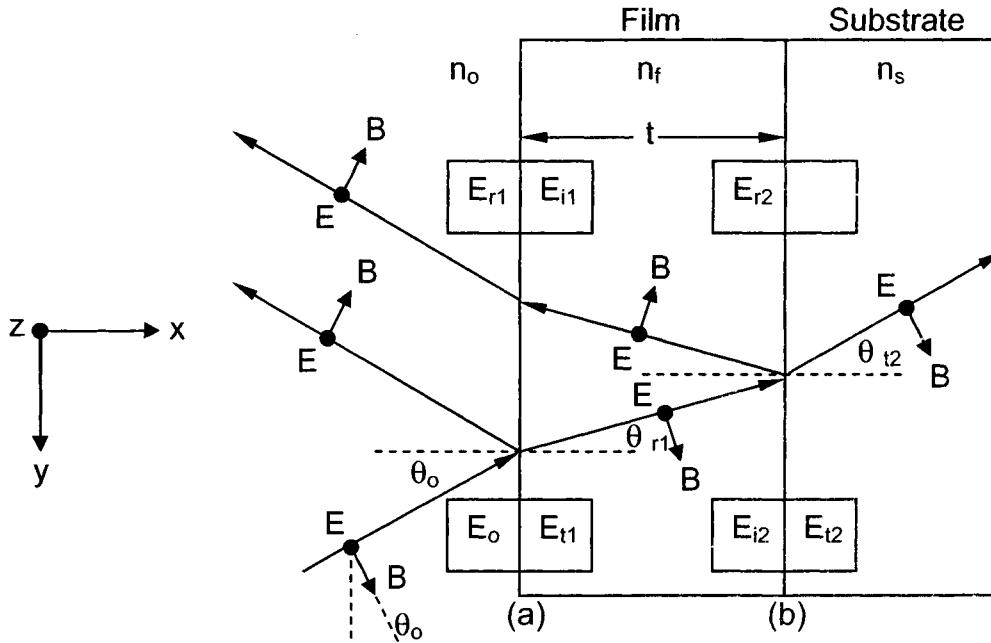
Figure 3.4.1: Reflection of a beam from a single layer film [13].

A brief explanation of the inner workings of the transfer matrix approach can be described by Figure 3.4.1. As shown, an incident beam with an E-field perpendicular to the plane of incidence strikes a film assumed to be homogeneous and isotropic in nature (as is the case with the fabricated sample) with a layer thickness on the order of the wavelength in the medium. As expected, a portion of the beam is reflected at interface (a) while the remainder continues on through to interface (b) where it undergoes the same process as at interface (a). To account for multiple beams from multiple reflections, the insets are included to define the magnitude of the E-fields at boundaries (a) and (b). For example, E_{r1} represents the sum of all the multiple reflected beams at interface (a) in the process of emerging from the film while E_{i2} represents the sum of all the multiple beams at interface (b) directed towards the substrate. Across the boundaries (a) and (b), both the E-fields and B-fields are continuous. Thus the corresponding equations are valid [13]

$$E_a = E_o + E_{r1} = E_{t1} + E_{i1} \qquad (3.10)$$

$$E_b = E_{i2} + E_{r2} = E_{t2} \qquad (3.11)$$

$$B_a = B_o \cdot \cos\theta_o - B_{r1} \cdot \cos\theta_o = B_{t1} \cdot \cos\theta_{t1} - B_{i2} \cdot \cos\theta_{t1} \quad (3.12)$$

$$B_b = B_{i2} \cdot \cos\theta_{t1} - B_{r2} \cdot \cos\theta_{t1} = B_{t2} \cdot \cos\theta_{t2} \quad (3.13)$$

keeping in mind the relation [13]

$$B = \frac{E}{v} = \left(\frac{n}{c}\right) \cdot E = n \cdot \sqrt{\mu_o \cdot \epsilon_o} \cdot E \quad (3.14)$$

Rewriting Equations 3.12 and 3.13 in terms of E-fields with the help of Equation 3.14 yields [13]

$$B_a = \gamma_o \cdot (E_o - E_{r1}) = \gamma_1 \cdot (E_{t1} - E_{i1}) \quad (3.15)$$

$$B_b = \gamma_1 \cdot (E_{i2} - E_{r2}) = \gamma_s \cdot E_{t2} \quad (3.16)$$

where

$$\gamma_o = n_o \cdot \sqrt{\epsilon_o \cdot \mu_o} \cdot \cos\theta_o$$

$$\gamma_1 = n_1 \cdot \sqrt{\epsilon_o \cdot \mu_o} \cdot \cos\theta_{t1} \quad (3.17)$$

$$\gamma_s = n_s \cdot \sqrt{\epsilon_o \cdot \mu_o} \cdot \cos\theta_{t2}$$

It is important to note that a phase change δ occurs as the light traverses the film. This phase change can be expressed by [13]

$$\delta = k_o \Delta = \left(\frac{2 \cdot \pi}{\lambda_o}\right) \cdot n_1 \cdot t \cdot \cos\theta_{t1} \quad (3.18)$$

Using Equation 3.18 in conjunction with Equation 3.12 and 3.13 followed by some arithmetic (a full account of which is given in Reference [13] chapter 19-1), the following matrix relationship was obtained [13]

$$\begin{bmatrix} E_a \\ B_a \end{bmatrix} = \begin{bmatrix} \cos\delta & \dfrac{i \cdot \sin\delta}{\gamma_1} \\ i \cdot \gamma_1 \cdot \sin\delta & \cos\delta \end{bmatrix} \cdot \begin{bmatrix} E_b \\ B_b \end{bmatrix} \quad (3.19)$$

The 2x2 matrix above is referred to as the transfer matrix of the film and in general can be represented by

$$M = \begin{bmatrix} m_{11} & m_{12} \\ m_{21} & m_{22} \end{bmatrix}$$

(3.20)

The beauty of Equation 3.19 is that it can be expanded. For example, if boundary (b) was another film rather than the substrate, the equation can be made valid by adding a second transfer matrix that would relate the electric and the magnetic fields at the now present third boundary (c) between the second film and substrate. Consequently, Equation 3.19 can be expanded to accommodate an arbitrary number of film layers as shown below [13].

$$\begin{bmatrix} E_a \\ E_b \end{bmatrix} = M_1 \cdot M_2 \cdot M_3 \cdots M_N \cdot \begin{bmatrix} E_N \\ B_N \end{bmatrix} = M_{Total} \cdot \begin{bmatrix} E_N \\ E_N \end{bmatrix}$$

(3.21)

With the behavior of the electric and magnetic fields accounted for in each film layer by the above equation, determining the stack reflectivity then becomes quite trivial. Once again using Equations 3.10, 3.11 and 3.15, 3.16 in combination with the reflection and transmission coefficients, the following two equations were derived [13]

$$1 + r = m_{11} \cdot t + m_{12} \cdot \gamma_s \cdot t$$

(3.22)

$$\gamma_o \cdot (1 - r) = m_{21} \cdot t + m_{22} \cdot \gamma_s \cdot t$$

(3.23)

where r and t are the reflection and transmission coefficients respectively and m_{11}, m_{22}, m_{12}, and m_{21} are the transfer matrix elements. Solving Equations 3.23 and 3.24 for r and t yields [13]

$$t = \frac{2 \cdot \gamma_o}{\gamma_o \cdot m_{11} + \gamma_o \cdot \gamma_s \cdot m_{12} + m_{21} + \gamma_s \cdot m_{22}}$$

(3.24)

$$r = \frac{\gamma_o \cdot m_{11} + \gamma_o \cdot \gamma_s \cdot m_{12} - m_{21} - \gamma_s \cdot m_{22}}{\gamma_o \cdot m_{11} + \gamma_o \cdot \gamma_s \cdot m_{12} + m_{21} + \gamma_s \cdot m_{22}}$$

(3.25)

The reflectance of the sample can then be determined by,

$$R = |r|^2$$ (3.26)

Throughout this derivation, the polarization of the electric field was assumed to be perpendicular to the plane of incidence as shown in Figure 3.4.1. For the case that the electric field is parallel to the plane of incidence, a minor change is required to γ_1 in Equation 3.17, the cosine factor shifts to the denominator of the equation as shown in Equation 3.27. In the case of randomly polarized light, an average of the perpendicular and parallel scenarios must be taken to obtain the correct result.

$$\gamma_1 = n_1 \cdot \frac{\sqrt{\epsilon_o \cdot \mu_o}}{\cos\theta_{t1}}$$ (3.27)

As stated earlier, a DBR stack may consist of many pairs of high and low index layers. For a stack with 40 pairs, 80 transfer matrices would be required to characterize the behavior of the propagating light through each individual layer. This monster task can be avoided if the pairs are identical and repeat in an organized fashion, as is the case with DBR stacks. The periodicity of the pairs enables the use of only 2 transfer matrices, one describing the high index layer and the other the low index layer. The resultant of these two transfer matrices is then put to the power of N where N is the number of pairs present in the stack.

Consequently, to model the reflectivity of a stack as a function of wavelength, the refractive index values of the high and low index materials must be known at the wavelength of interest, and their layer thicknesses (typically quarter-wave thickness for high reflectivity) along with the angle of incidence of the light. The only variable remaining and directly affecting the reflectivity is that of N defining the number of pairs in the stack. The larger this value, the higher the reflectivity.

All the above reflectivity calculations for this project were carried out in MathCAD. A copy of the code along with a sample calculation can be found in Appendix 7.4. The reflectivity modeling for the DBR stacks modeled thus far dictated 45

pairs, for the InP substrate design, to achieve a reflectivity of 99.9% at 1550nm when the incident medium for the light was InP. The model was adjusted to accommodate the experimental conditions which had air as the incident medium. With this adjustment made, it was decided that 20 pairs was a reasonable number yielding a theoretical reflectivity of 96.6% at the center wavelength of 1550nm. For the GaAs substrate design, it was calculated that 20 pairs would yield a theoretical reflectivity of 94.9% at the center wavelength of 1550nm.

3.5 Mirror Losses

Thus far, no loss factors have been discussed in the DBR stack reflectivity modeling. This is due to the fact that the amount of loss in the DBR is so very small that it can for the most part be neglected entirely. On average, a reasonably doped DBR stack may have total losses ranging from $5cm^{-1}$ to $15cm^{-1}$ depending on quality of growth and material composition [22]. In general, the local incremental loss due to doping is approximately $11cm^{-1}$ per $10^{18}cm^{-3}$ of p-doping and $5cm^{-1}$ per $10^{18}cm^{-3}$ of n-doping in the 850nm to 980nm range and slightly higher in the $1.3\mu m$ to $1.55\mu m$ range [3].

Another source of loss in the DBR stack is due to the operational temperature of the VCSEL. The higher the VCSEL temperature, the larger the absorption of the mirror as more carriers are able to overcome the energy band gap. It is for this reason that band gaps in DBRs are purposely designed to be somewhat larger in energy than the intended photon energy to avoid unnecessary absorption.

Losses may also arise depending on the material transition from layer to layer in the DBR stack. For this project, the layer transitions were quite abrupt resulting in minimal losses. If the transition were graded however as is the case with some DBRs, more losses would be evident and the above model could not effectively be applied without some perturbations.

The DBR stacks designed for this project had minimal doping (on the order of $10^{14} cm^{-3}$), operated at room temperature and had sharp, abrupt junctions. This translates into minute losses and they are thus not considered when modeling the stack.

3.6 DBR Stack Model Summary

From the above discussion, it is evident that there are many aspects to consider when designing a highly reflective DBR stack. The initial consideration must be the desired reflectivity at a given wavelength. In this design case, a center wavelength of 1550nm was desired with a reflectivity of roughly 95% so as to have a reasonable number of pairs in the super-lattice. With these goals set, material selection became the next issue. The first sample consisted of InP/InGaAsP pairs for the low and high index requirements, respectively grown on an InP substrate. The second sample was grown on a GaAs substrate with high and low index layers composed of GaAs/InGaP, respectively. Band gap calculations were carried out to determine a composition for the quaternary and ternary compounds that would not be absorbing at the operational wavelength. A band gap of 0.90eV was set as the target for the quaternary yielding a composition of $In_{0.64}Ga_{0.36}As_{0.777}P_{0.223}$. The band gap value of the second stack was calculated to be 1.896eV for a lattice matched composition of $Ga_{0.516}In_{0.484}P$. Further calculations were then conducted to determine the index of refraction for each layer in the pairs. The refractive indexes were 3.17 and 3.474 for the InP and InGaAsP layers respectively and 3.37 and 3.131 for the GaAs and InGaP layers respectively. Using this information, it was found that growth thicknesses for the first sample should be 111.5nm and 122.2nm for the high and low refractive indexes respectively, satisfy the Bragg quarter-wave condition. For the second sample, thicknesses were calculated to 123.8nm for the ternary layer and 115.0nm for the binary layer. Subsequent modeling revealed that 20 pairs yielded a reflectivity of 97% for the first sample and 95% for the second. Schematic diagrams of the designed DBR stacks are shown in Figure 3.6.1 and 3.6.2.
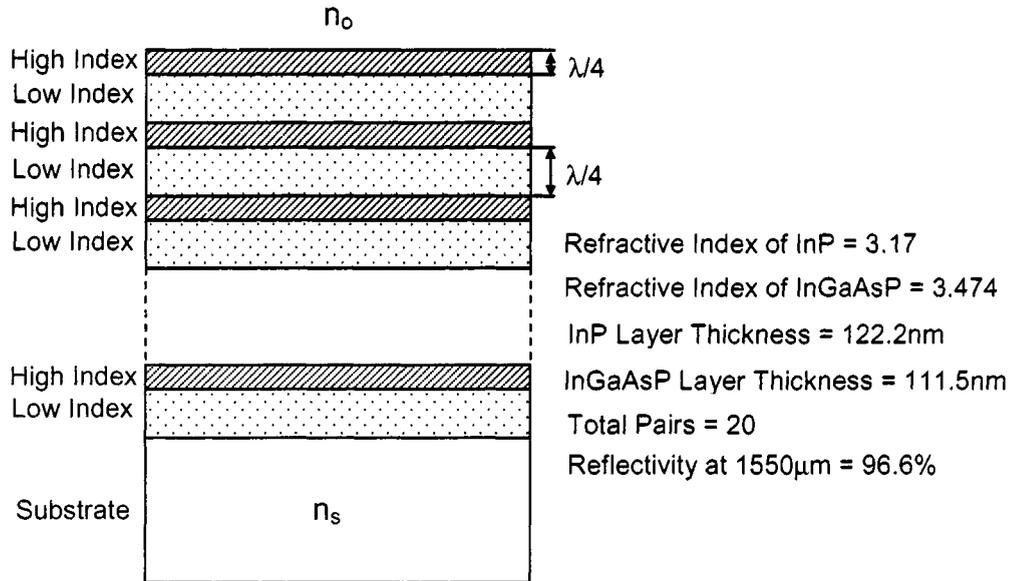
Figure 3.6.1: DBR design summary for InP substrate.
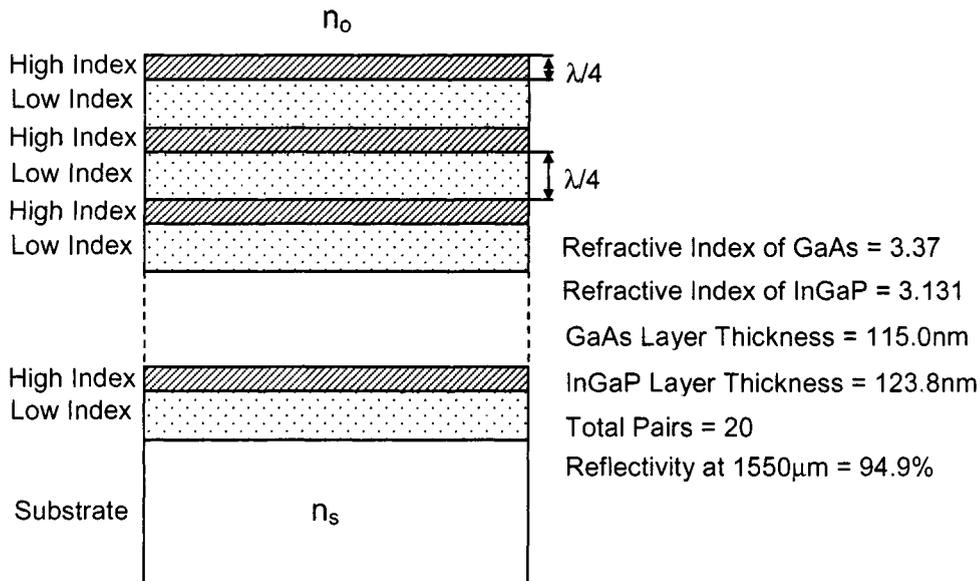
Figure 3.6.2: DBR design summary for GaAs substrate.

4. Experimental Results and Analysis for InP/InGaAsP DBR

4.1 Reflectivity Measurement Preparations

The reflectivity measurements were carried out in several phases. First, the as grown sample was cleaved into seven segments in order to provide samples for several methods of characterization including X-ray analysis, transmission electron microscopy and for reflectivity measurements.

The goal of the reflectivity measurements was to a) confirm the theoretical calculations and b) determine the uniformity of growth throughout the 40 layers of the DBR stack. Consequently, five sample pieces were required to carry out reflectivity measurements at a variety of pair numbers in the DBR stack. In order to carry out these measurements, four of the five samples required the wet etch removal of several pairs. The number of pairs desired in each sample piece was arbitrarily chosen to provide a broad coverage. The final breakdown was:

a) 20 pair DBR sample (no etching required)

b) 18 pair DBR sample

c) 14 pair DBR sample

d) 12 pair DBR sample

e) 6 pair DBR sample

With a multitude of samples such as these, it becomes possible through reflectivity measurements to detect any variability in the layer thicknesses after the sample has been grown. Simultaneously, the effects of the number of pairs present on the reflectivity of the DBR stack can also be determined.

Etching of the samples was carried out to remove the layers in pairs which required two separate steps with different etchants used for each layer in part. The etchant used for the quaternary layer was $H_2SO_4:H_2O_2:H_2O$ (1:1:10), with an etch rate of 0.1μm/min [23]. The etchant for the InP layer was $HCl:H_3PO_4$ (1:3), with an etch rate of 0.4μm/min [23]. After etching, reflectivity measurements were carried out at incident light angles of 0°, 12°, 24°, and 36°.

4.2 Variable & Normal Incidence Measurements

The normal incidence measurements were conducted first and in a continuous sequential order for each sample. This was done to ensure consistency in the measurements and to eliminate any alignment issues that could arise from moving the laser source over to the variable angle setup. Furthermore, each sample underwent the reflectivity measurement at least three times with the incident beam spot moved to a different part of the sample surface such that an average over the entire sample surface was taken and reproducibility of results was confirmed.

The variable angle measurements were also conducted such that three or more measurements were taken for each sample making sure that the measurements were carried out at various points on the sample. The incident variable angles chosen were 12°, 24°, and 36° to provide a broad coverage as well as to allow for the investigation of any trends present relating to incident light angles.

Figures 4.2.1(a to e) depict the findings of the measurements carried out on five samples. Error bars found on the graphs are obtained by determining the standard deviation between trial runs.

Reflectivity of 20 Pair InP/InGaAsP DBR Stack at Variable Incident Light Angles
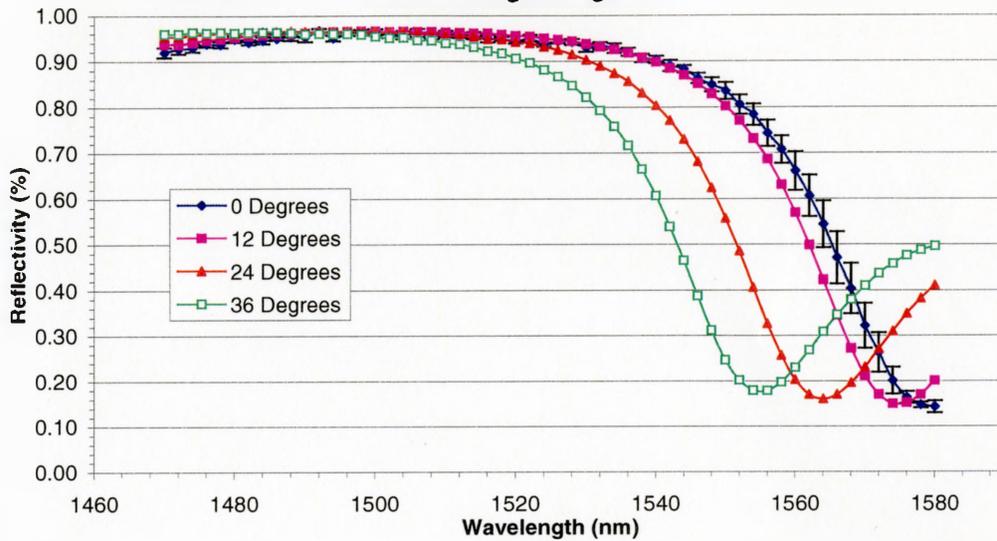
Figure 4.2.1(a)

Reflectivity of 18 Pair InP/InGaAsP DBR Stack at Variable Incident Light Angles
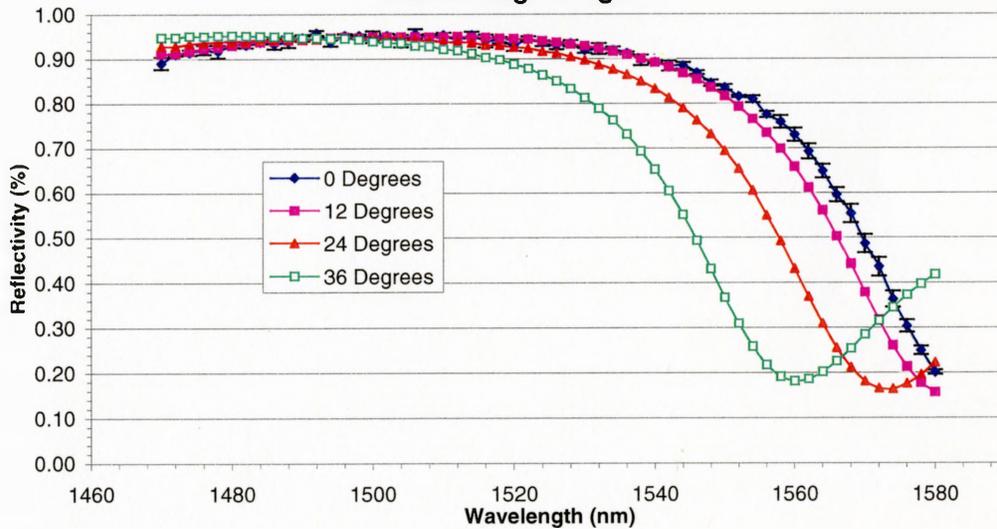
Figure 4.2.1(b)

Reflectivity of 14 Pair InP/InGaAsP DBR Stack at Variable Incident Light Angles
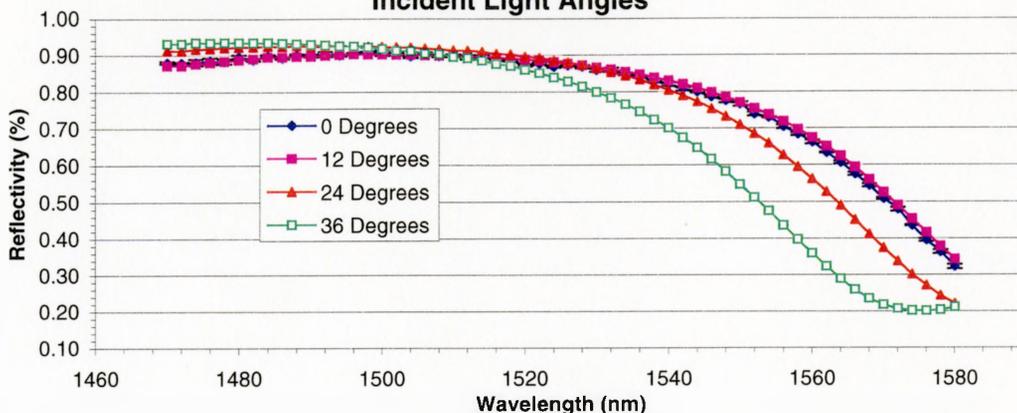
Figure 4.2.1(c)

Reflectivity of 10 Pair InP/InGaAsP DBR Stack at Variable Incident Light Angles
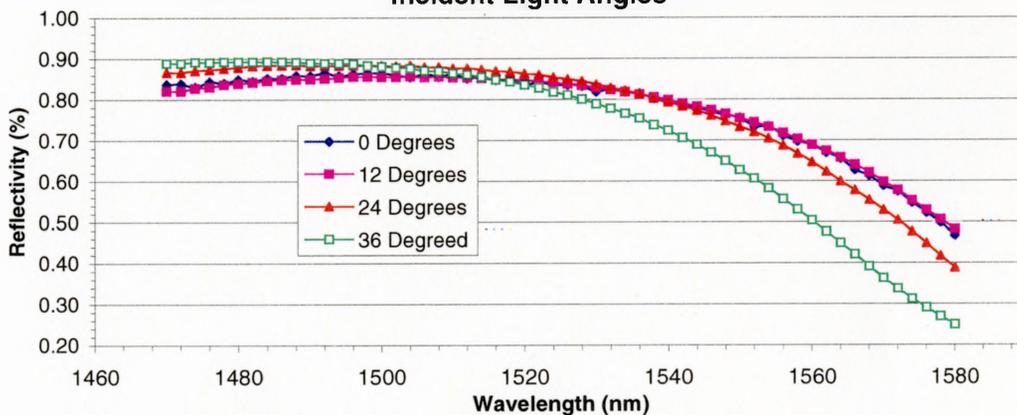
Figure 4.2.1(d)

Reflectivity of 6 Pair InP/InGaAsP DBR Stack at Variable Incident Light Angles
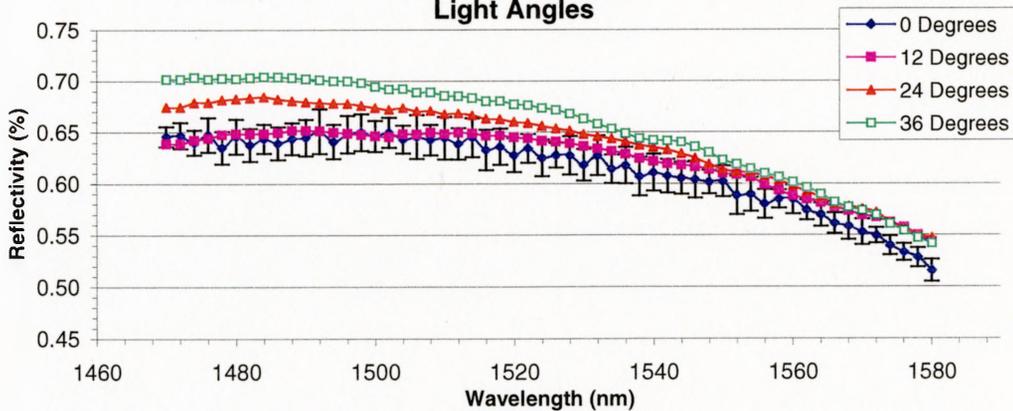
Figure 4.2.1(e)

A quick visual examination of Figures 4.2.1(a to e) reveal one important detail. The center of the stop-band at normal incidence is not at the planned 1550nm wavelength as was originally designed. It appears that the center of the stop-band is actually around 1510nm. This shift however appears to have had no effect on the target reflectivity of 97% for the 20 pair stack at normal incidence. This discrepancy can be explained by errors in the values of refractive indices used or layer thicknesses that were not exactly as designed. Compositional errors in the quaternary layer may also be responsible for this shift as this would affect the index of the quaternary. Figure 4.2.2 plots the theoretical curve using all the modeled values for the 20 pair stack with the experimentally obtained curve to better illustrate the shift present. Figure 4.2.3 illustrates the theoretical reflectivity over a broad spectral window for all five stacks.

Comparison of Theorectal & Experimental Results for InP/InGaAsP 20 Pair Stack
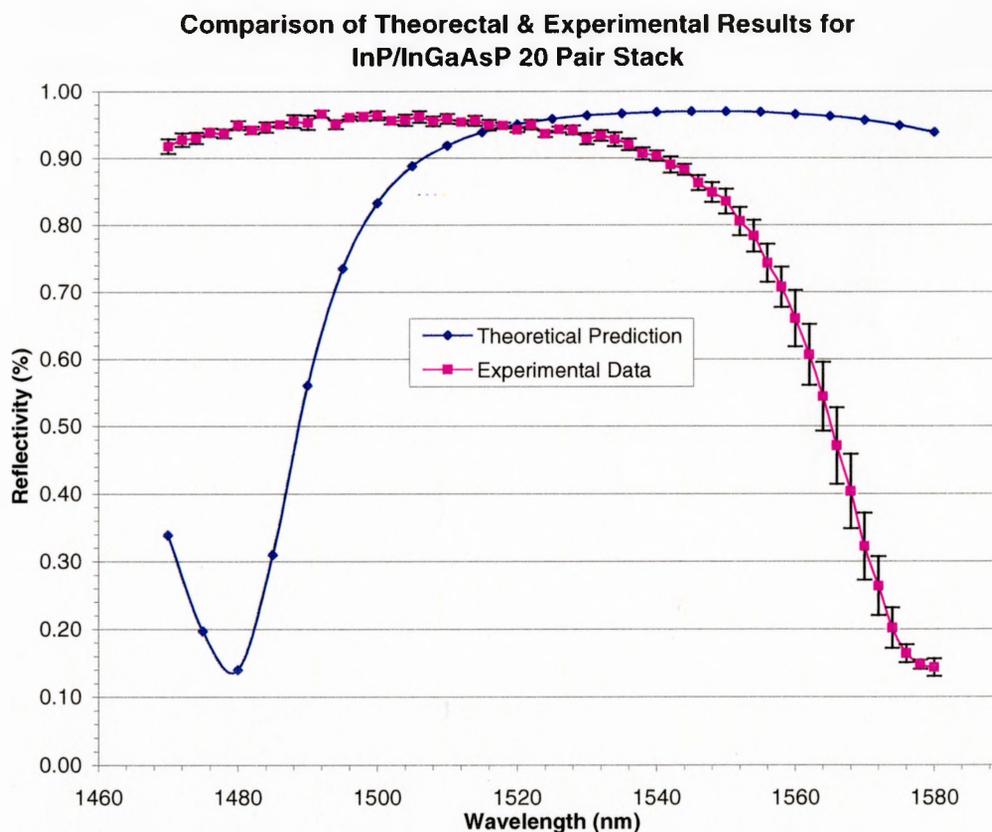
Figure 4.2.2: Comparison of original theoretical values used to calculate reflectivity for 20 pair stack with experimentally gathered curve.
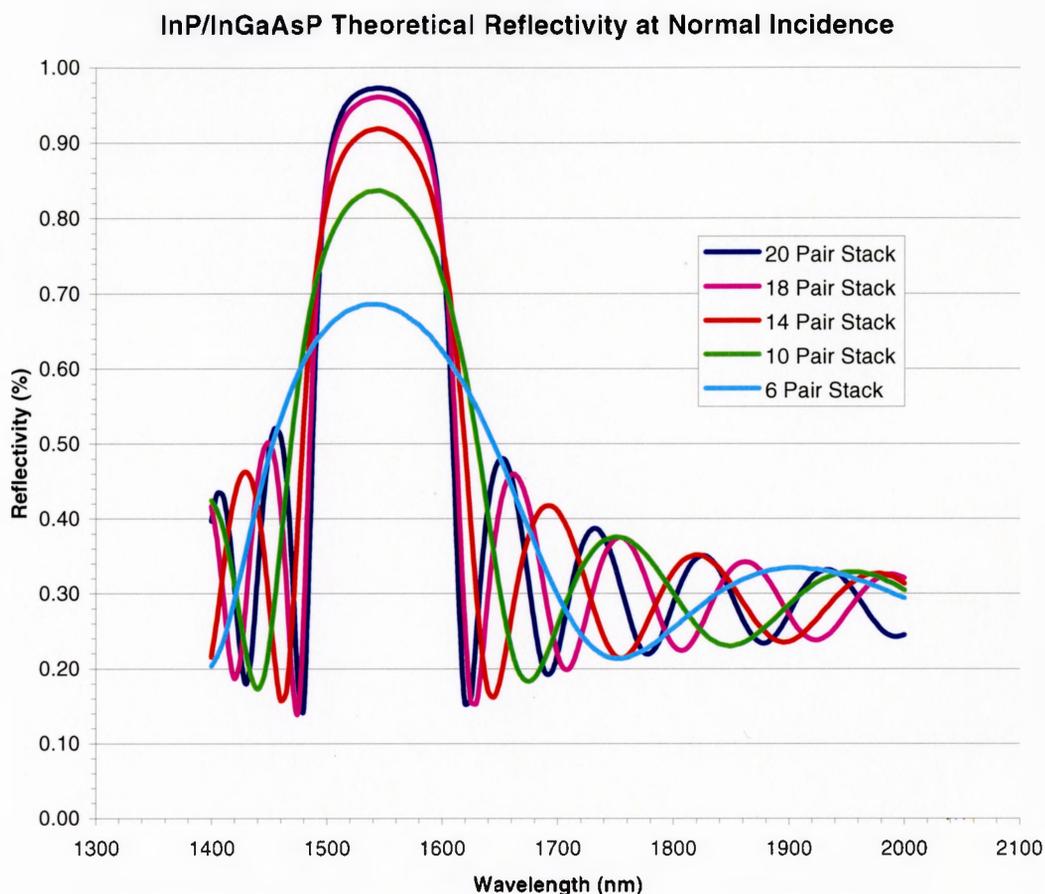
Figure 4.2.3: Theoretical Reflectivity of InP/InGaAsP DBR stack with various numbers of pairs at normal incidence.

Further examination of the experimental plots also uncovers another important point. Despite the fact that a shift is present, the shift is constant throughout all the five samples as can be seen in Figure 4.2.4. This means that regardless of the cause of the shift, the effects do not vary through the growth. In other words, if the shift is caused by a compositional error in the quaternary, the error does not occur in say one single layer but rather all the way through each quaternary layer. As a result, modeling perturbations to take into account the present shift were straightforward.

Furthermore, the consistency observed in the experimental data abolishes concerns of drastic 'wandering' of composition and thicknesses known to plague the growth and manufacturing of large DBR stacks [24].

Reflectivity of InP/InGaAsP DBR Stack
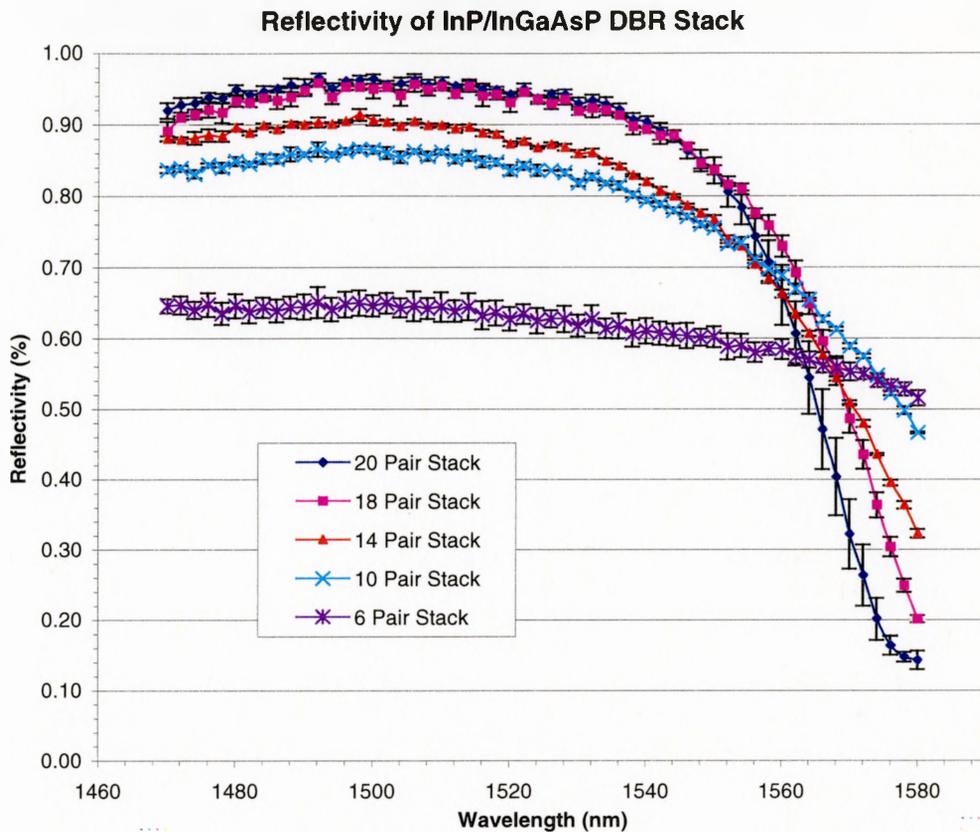
Figure 4.2.4: Normal incidence reflectivity measurement of InP/InGaAsP DBR stack with various numbers of pairs.

Turning the focus onto the variable angle experimental findings, it becomes apparent that the reflectivity curve is more blue shifted as the incident angle is increased. Figure 4.2.5 plots the theoretical results of the 20 pair stack at incident angles of 0°, 12°, 24°, 36°, and 48°. This figure confirms the blue shift found in the experimental results and also reveals that the reflectivity of the stop band increases ever so slightly the larger the incident light angle. This observation is clearly visible in the experimental data plotted in Figure 4.2.1(d and e) and somewhat visible in Figure 4.2.1 (a to c). It is important to note that as angle of incidence increases, so does the effective thickness. Consequently, so does the optical path difference and hence the phase difference resulting in the observed blue shift of the curves.

Variable Incident Angles for 20 Pair InP/InGaAsP DBR Stack
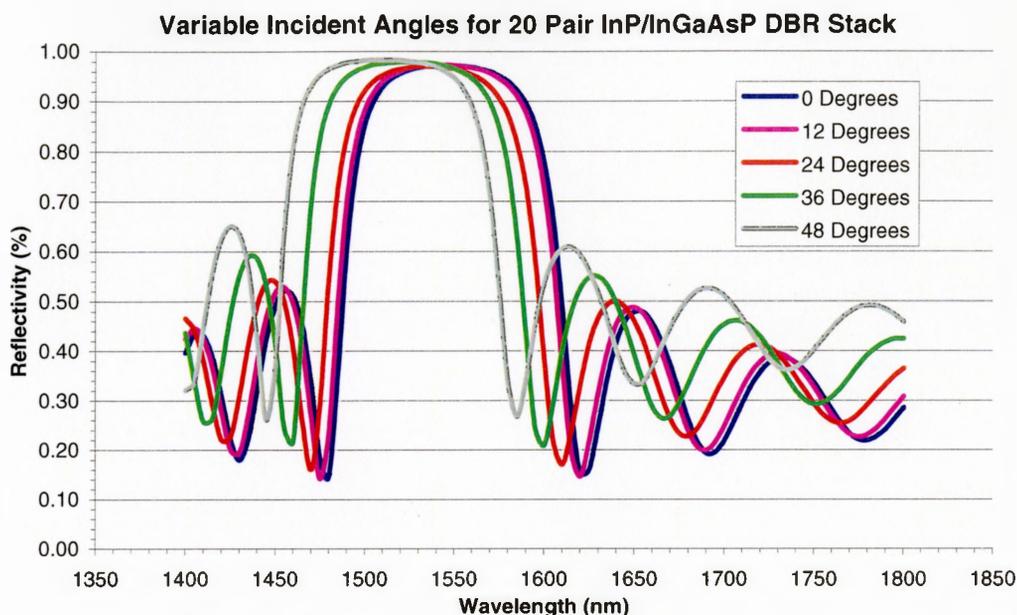
Figure 4.2.5: Variable incident reflectivity measurement
of 20 pair InP/InGaAsP DBR stack.

4.3 Theoretical Curve Fitting to Experimental Data

Curve fitting to the experimental data essentially uses all the principles and mathematical models discussed in Chapter 3 to determine DBR design at a given operational center wavelength. These models are extended to apply to wavelengths in the entire operational window as opposed to the single center wavelength. This process involves calculating the index of refraction as a function of wavelength (index varies slightly with wavelength) for both the binary and quaternary layers using the exact same approach as carried out in Chapter 3. With the indices calculated, the values are then substituted into the reflectivity calculations to determine the reflectivity. Appendix 7.5 provides a sample set of calculations for this process.

As illustrated in Figure 4.2.2, the theoretical fit does not remotely match the experimental data. Thus, in order to fit the theoretical curve to the experimental results, parameters within the theoretical model were varied in a systematic fashion. The four control parameters included a) thickness of quaternary layers b) thickness of binary layers c) index of refraction for quaternary (with respect to wavelength) d) index of refraction

for binary (with respect to wavelength). It is important to note here that the parameters pertaining to the index of refraction encompass both errors in index calculations as well as those caused by compositional uncertainties. As a result, should the fault lie with the index, steps should be taken to determine the root cause.

All of the noted parameters can be altered for each individual layer of the DBR stack proving to be quite a challenge for such a large stack. Fortunately, as observed in Section 4.2, the shift present in the experimental results is constant throughout the layers of the constructed stack. Hence, any changes made to the parameters would apply equally to the 20 layers simplifying the task.

As a benchmark, a 1% change was applied to each parameter individually. This allowed for a visual interpretation of the magnitude of change for a 1% adjustment. The outcome of these tests for the 20 pair DBR stack are displayed in Figures 4.3.1 (a & b).
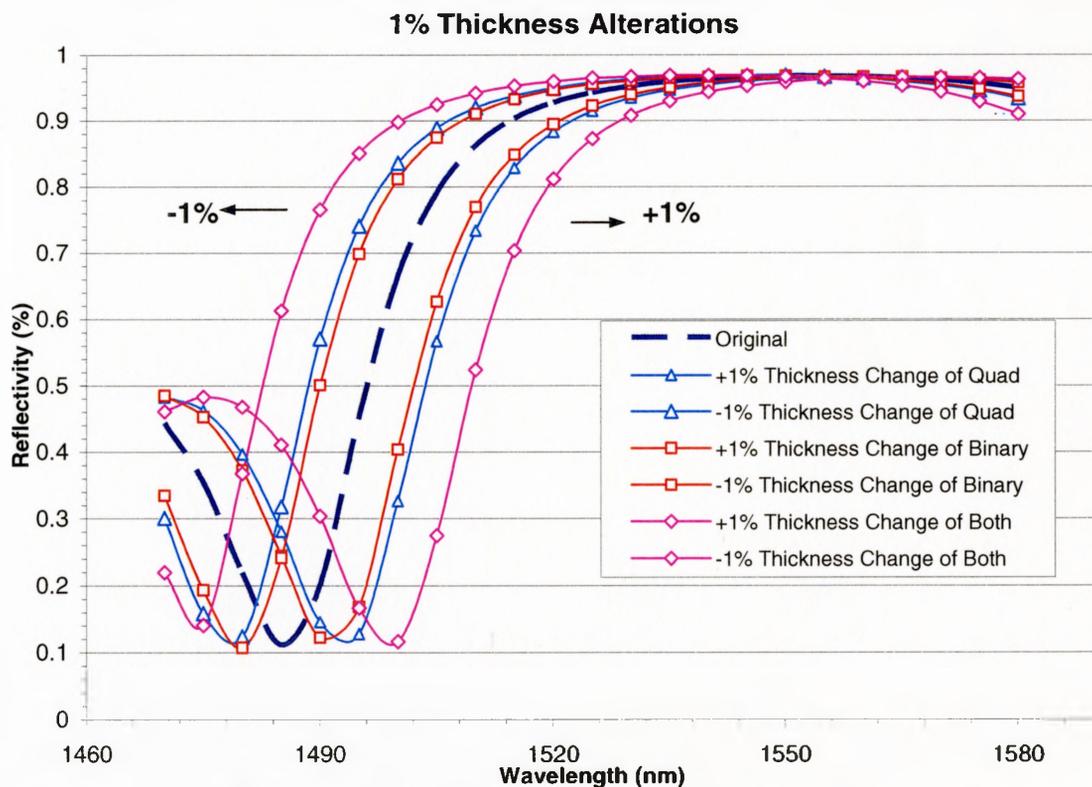
Figure 4.3.1(a): Observed effects of a ±1% alteration
in 20 pair DBR stack layer thickness.

1% Index Alterations
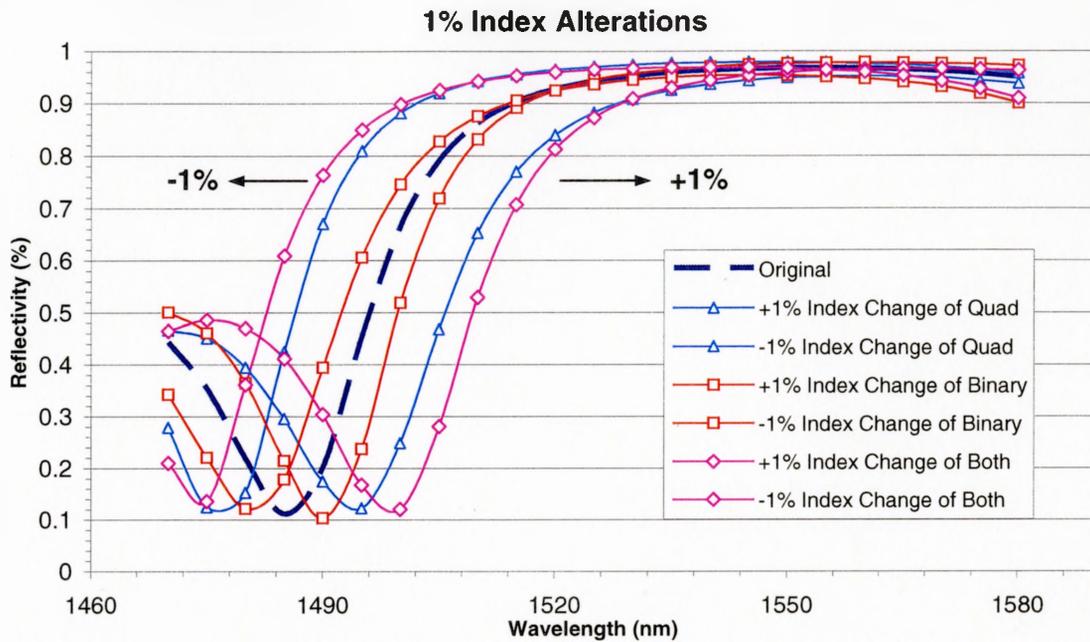
Figure 4.3.1(b): Observed effects of a ±1% alteration of index of refraction for 20 pair DBR stack.

Examination of Figures 4.3.1(a & b) uncovers some interesting points. It appears that negative alterations blue-shift the curve while positive alterations red-shift the curve. Furthermore, the modifications in the quaternary are noticeably bigger than those of the binary as the index and thickness values are larger. From Figure 4.3.1(a), it can be concluded that thickness alterations do not affect the stop-band reflectivity and only result in lateral shifts. The lateral shifts are a direct result of the Bragg quarter-wave condition (Equation 4.1).

$$L_{(1,2)} = \frac{\lambda_{Bragg}}{4 \cdot n_{(1,2)}} \qquad (4.1)$$

As the thickness is varied, the Bragg wavelength is shifted yielding the observed effects.

In contrast to the thickness variations, the index alterations result in both horizontal and vertical changes in the reflectivity curves. This observation has largely to do with both the Bragg quarter-wave equation (dependency on index) as well as the

reflectivity equation of a DBR with m quarter-wave pairs at the Bragg wavelength as can be seen by Equation 4.2 (also dependent on index) [25].

$$R_{DBR} = \left(\frac{1 - \left(\frac{n_1}{n_2} \right)^{2m}}{1 + \left(\frac{n_1}{n_2} \right)^{2m}} \right)^2 \qquad (4.2)$$

From this benchmark test, it was determined that the shift present were solely the result of thickness errors during growth as there was little or no observed vertical shifts in Figure 4.2.4. More specifically, the growth error must be a result of layers being more than 1% thinner than originally specified (as the observed shift is to the left by a significant amount). Consequently, in order to fit the theoretical curve to the experimental data, the layer thicknesses are modified.

Through a process of trial and error, thicknesses were varied until a suitable fit was obtained. This was achieved by using a least squares method (Equation 4.3) where the best fitting curve yields a minimum value for a result [26].

$$\Pi = \sum_{i=1}^{n} [y_i - f(x_i)]^2 \qquad (4.3)$$

where y_i is the experimental value for reflectivity at a given wavelength and $f(x_i)$ is the fitted curve's value for reflectivity at the same wavelength.

The quaternary thickness was reduced from 111.5nm to 108nm, a change of 3.14%. The designed binary thickness of 122.2nm dropped down to 117.5nm, a change of 3.85%. Figures 4.3.2 to 4.3.6 plot the experimental data fitted with the modified theoretical curves for all the incident light angles and various number of pairs.
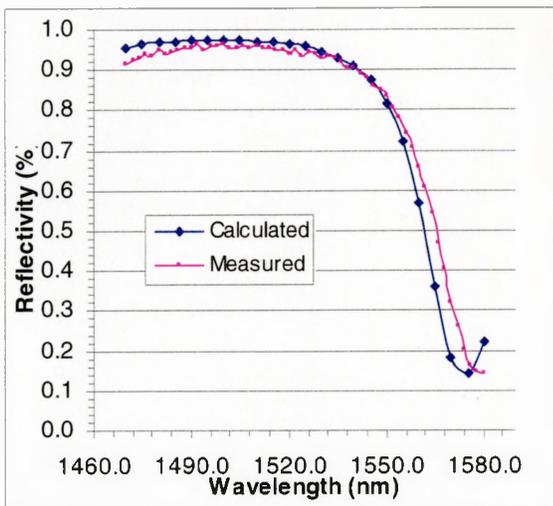
(a) 0° incidence
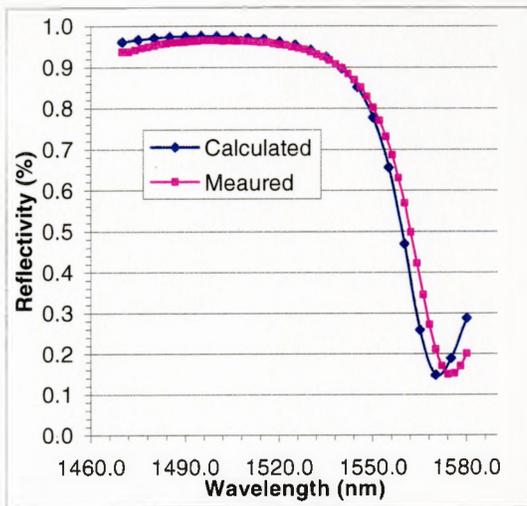
(b) 12° incidence
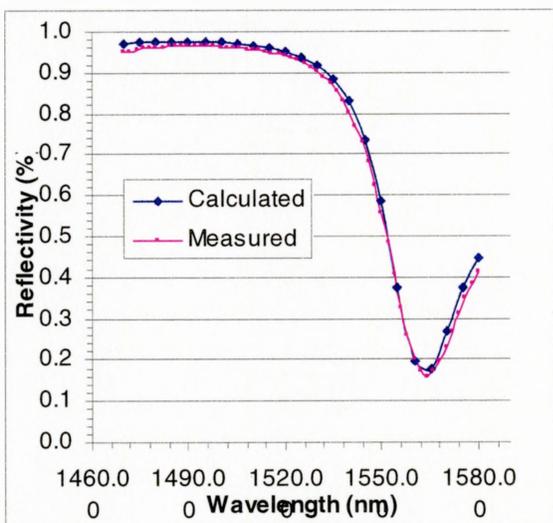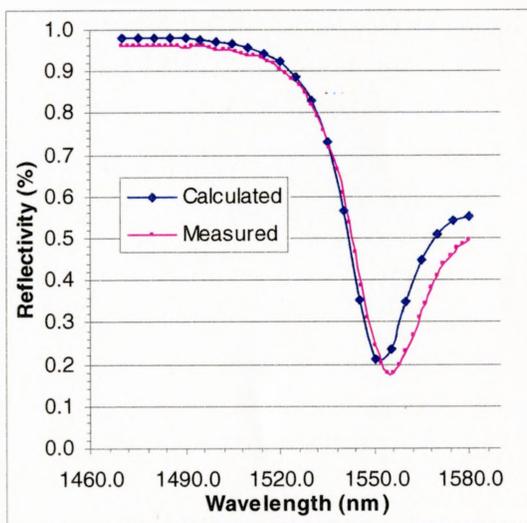
(c) 24° incidence

(d) 36° incidence

Figure 4.3.2: Theoretical fit to experimental data of
20 pair InP/InGaAsP DBR stack.
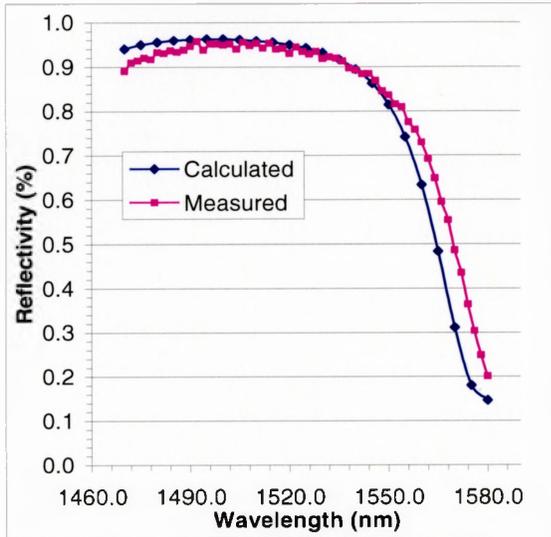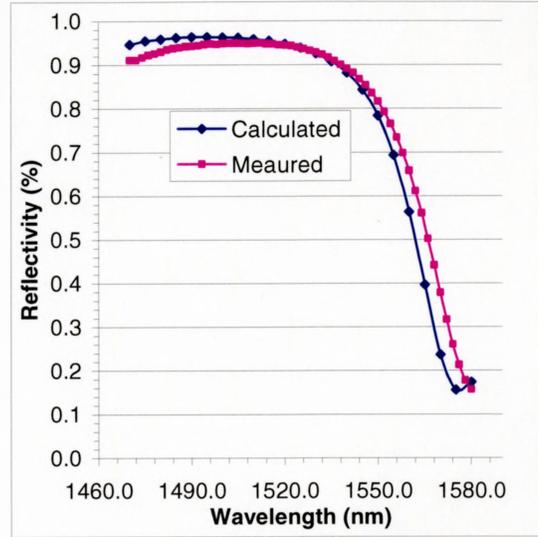
(a) 0° incidence
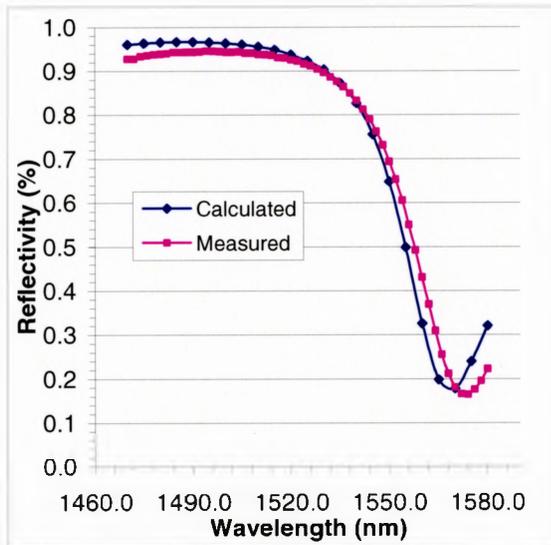
(b) 12° incidence
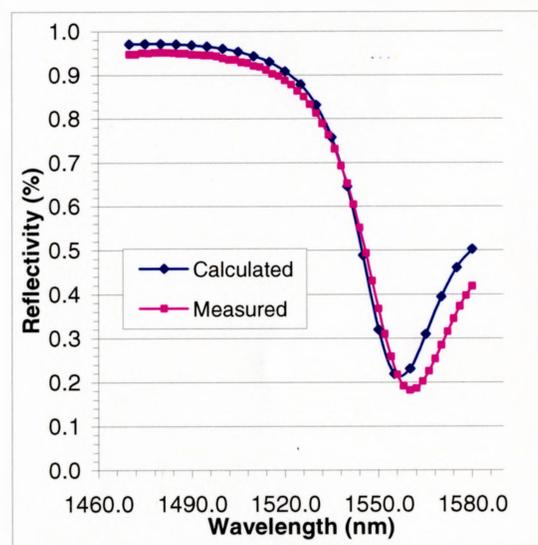
(c) 24° incidence

(d) 36° incidence

Figure 4.3.3: Theoretical fit to experimental data of
18 pair InP/InGaAsP DBR stack.
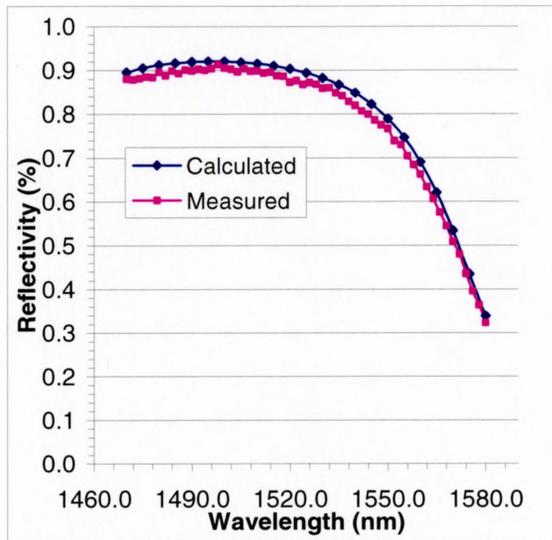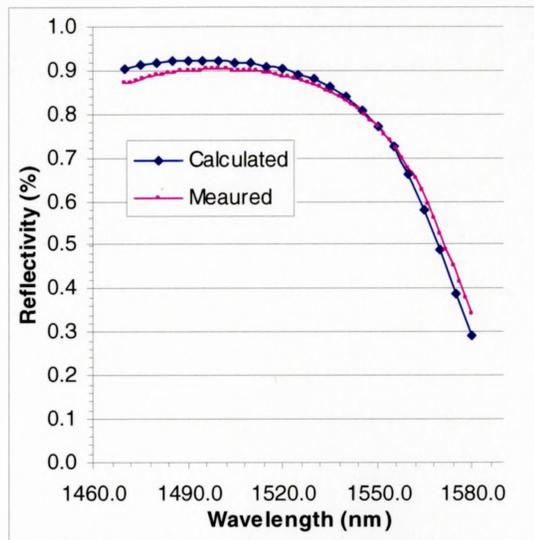
(a) 0° incidence
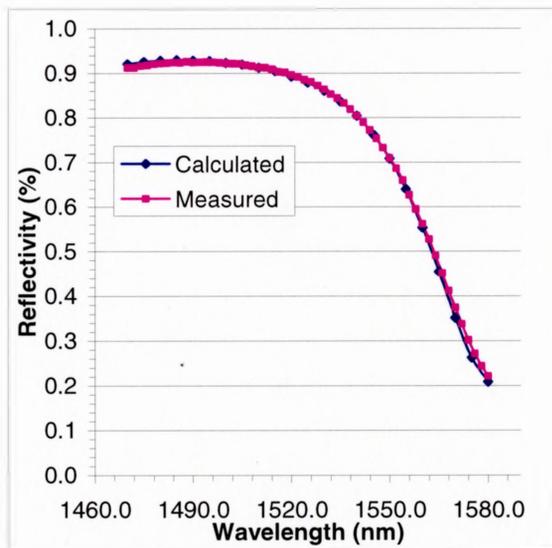
(b) 12° incidence
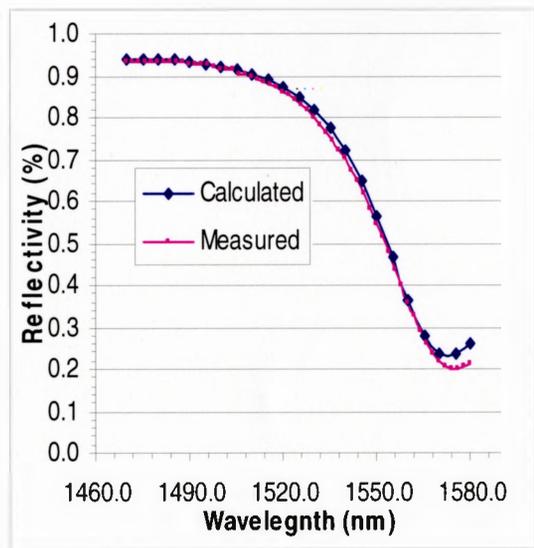
(c) 24° incidence

(d) 36° incidence

Figure 4.3.4: Theoretical fit to experimental data of
14 pair InP/InGaAsP DBR stack.

(a) 0° incidence

(b) 12° incidence

(c) 24° incidence

(d) 36° incidence
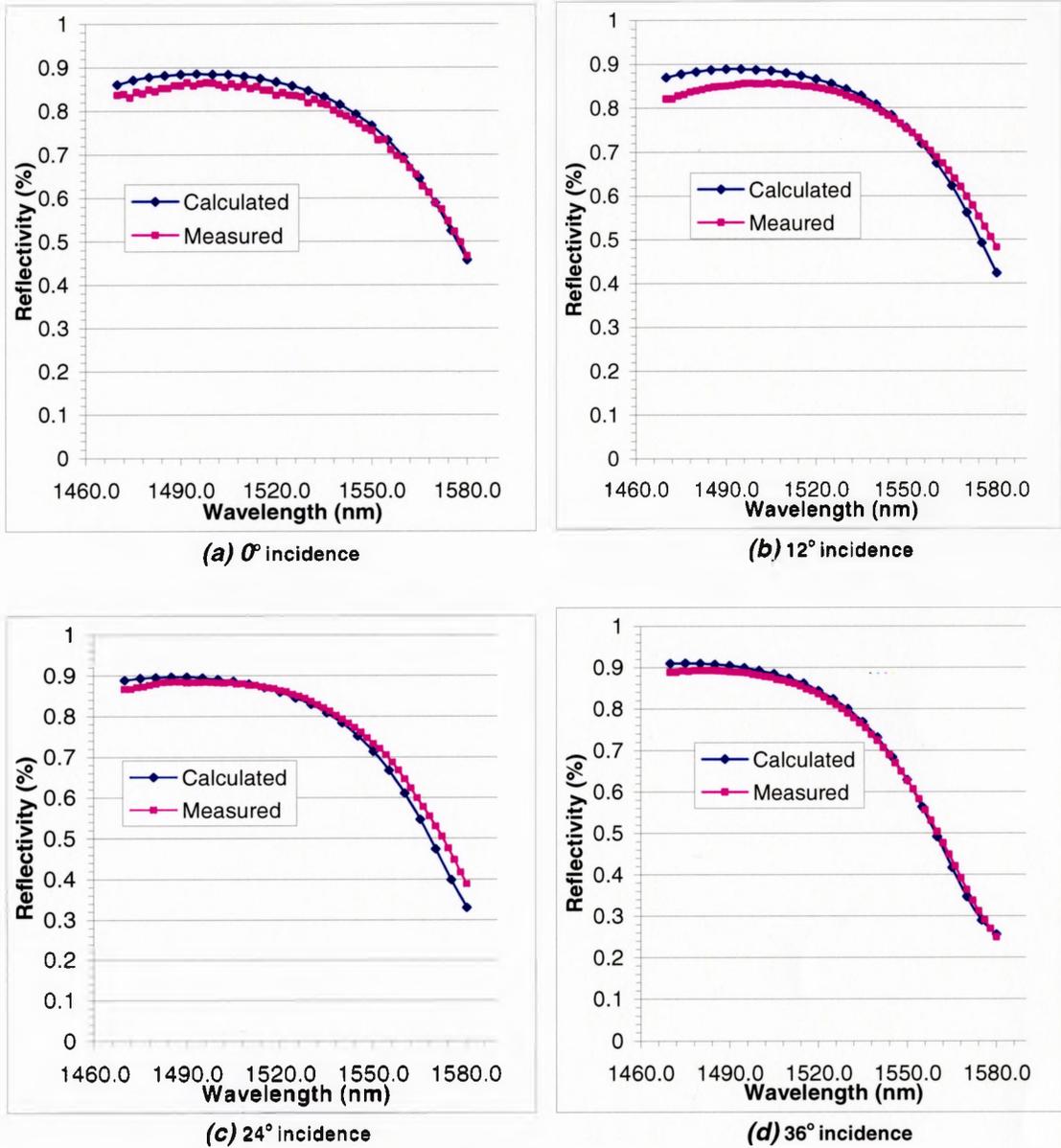
Figure 4.3.5: Theoretical fit to experimental data of 12 pair InP/InGaAsP DBR stack.
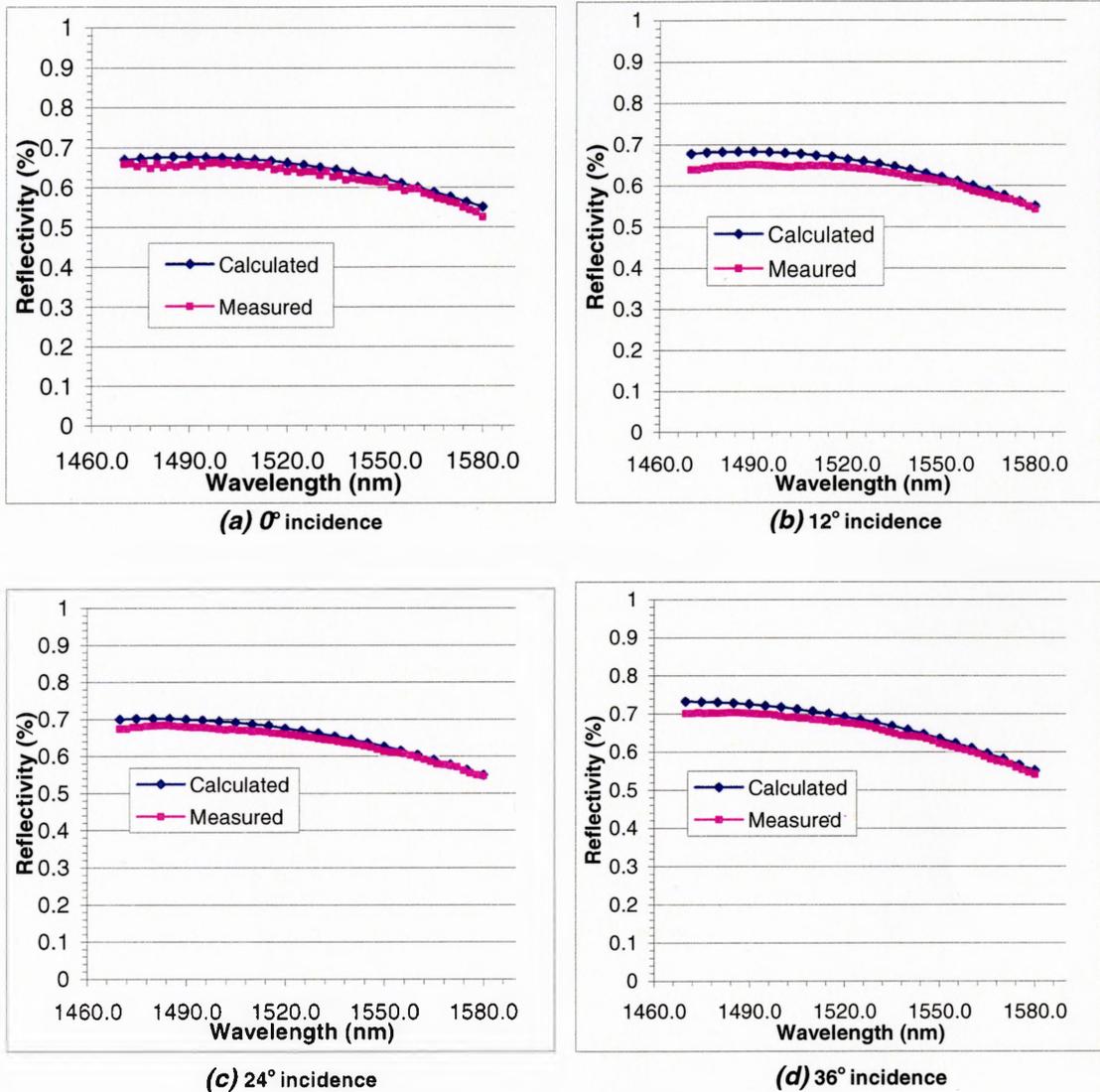
Figure 4.3.6: Theoretical fit to experimental data of
6 pair InP/InGaAsP DBR stack.

The modified theoretical fits and the experimental results are in decent agreement. They confirm the index of refraction calculations and DBR design model while successfully uncovering the cause of the stop-band shift. Any discrepancies between the experimental and theoretical curves observed in Figures 4.3.2 to 4.3.6 can be attributed to experimental error. This error includes many factors, the first and most significant being the condition of the sample surface. Any dust particle, dirt, tweezer scratches, or dried on etchant can have unfavorable effects on the measured reflectivity. Another source of

error was the varying room temperature that fluctuated at times from 20°C to 30°C affecting the detector responsivities by up to 5% [27]. Other minor sources of error affecting measurements would involve misalignment of detectors, variations in the tunable laser power output over time, as well as the lighting conditions in the room (experiments sometimes conducted with room lights off).

4.4 Effects of Improper Chemical Etching

The chemical etching process briefly described in Section 4.1 is quite crucial to the DBR stack's reflectivity. Great care should be taken to ensure that each and every layer is completely removed before moving on to the next layer. If for example a given layer is not completely removed (not etched for the appropriate amount of time), the next etchant solution will have little or no effect when the sample is immersed in it. As a result, the number of layers removed will then become unclear.

Any errors made during the etching process will only be obvious after the reflectivity measurements have been carried out and the experimental results have been compared to the theoretical calculations. Figure 4.4.1 plots the effects of an incomplete etch for a 6 pair InP/InGaAsP DBR stack. In this case, a thin film of unknown thickness of InP was left on the quaternary surface resulting in 6 complete layers with some InP residue. The effects of this thin unwanted layer are obvious in Figure 4.4.1 as this thin layer disrupts the Bragg quarter-wave condition for maximum reflection.

M.A.Sc. Thesis – M. Shahideh. McMaster – Engineering Physics

52

Reflectivity of 6.X Pair InP/InGaAsP DBR Stack at Variable Incident Light Angles
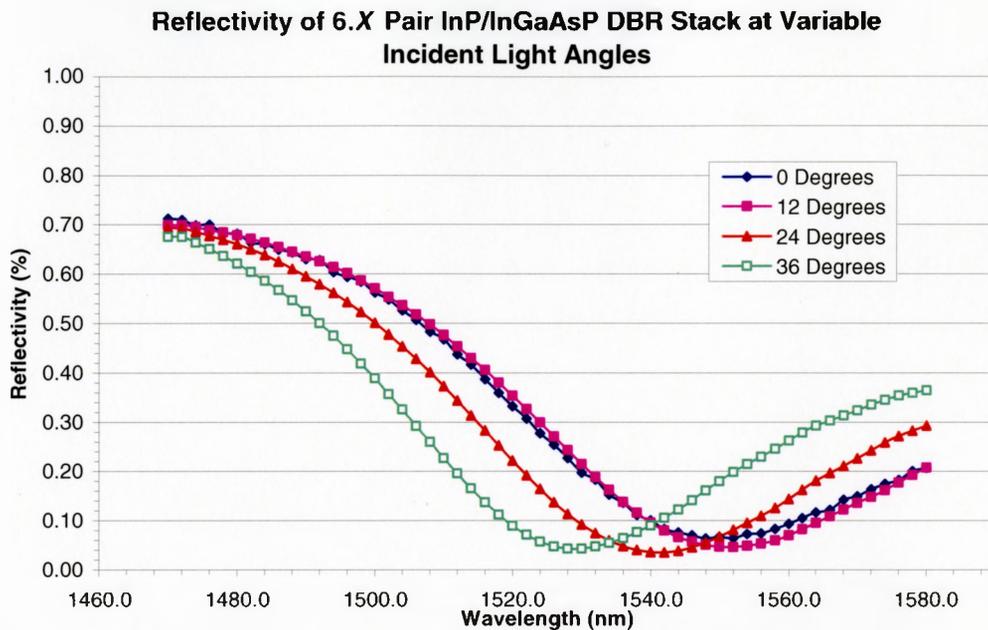
Figure 4.4.1: Plot of improperly etched 6 pair DBR stack resulting in alterations of reflectivity characteristics.

4.5 Transmission Electron Microscopy (TEM)

In order to investigate the layer structure of the super-lattice and attempt to reconfirm the fact that layer thickness 'wandering' (which plagues large DBR stacks) was not an issue with this DBR stack, transmission electron microscopy (TEM) was utilized. The results showed that the super-lattice was too large to fit the field-of-view of the TEM system at the desired magnification. That is to say that at a magnification of 200,000, not all the layers in the structure could fit into the field of view. Figure 4.5.1 provides the micrograph of the entire 40 layer DBR stack at a magnification of 22,000. As can be seen, the contrast between layers is not sharp and hence accurately determining where one layer ends and another begins in almost impossible (especially after further magnification by digitizing the image).
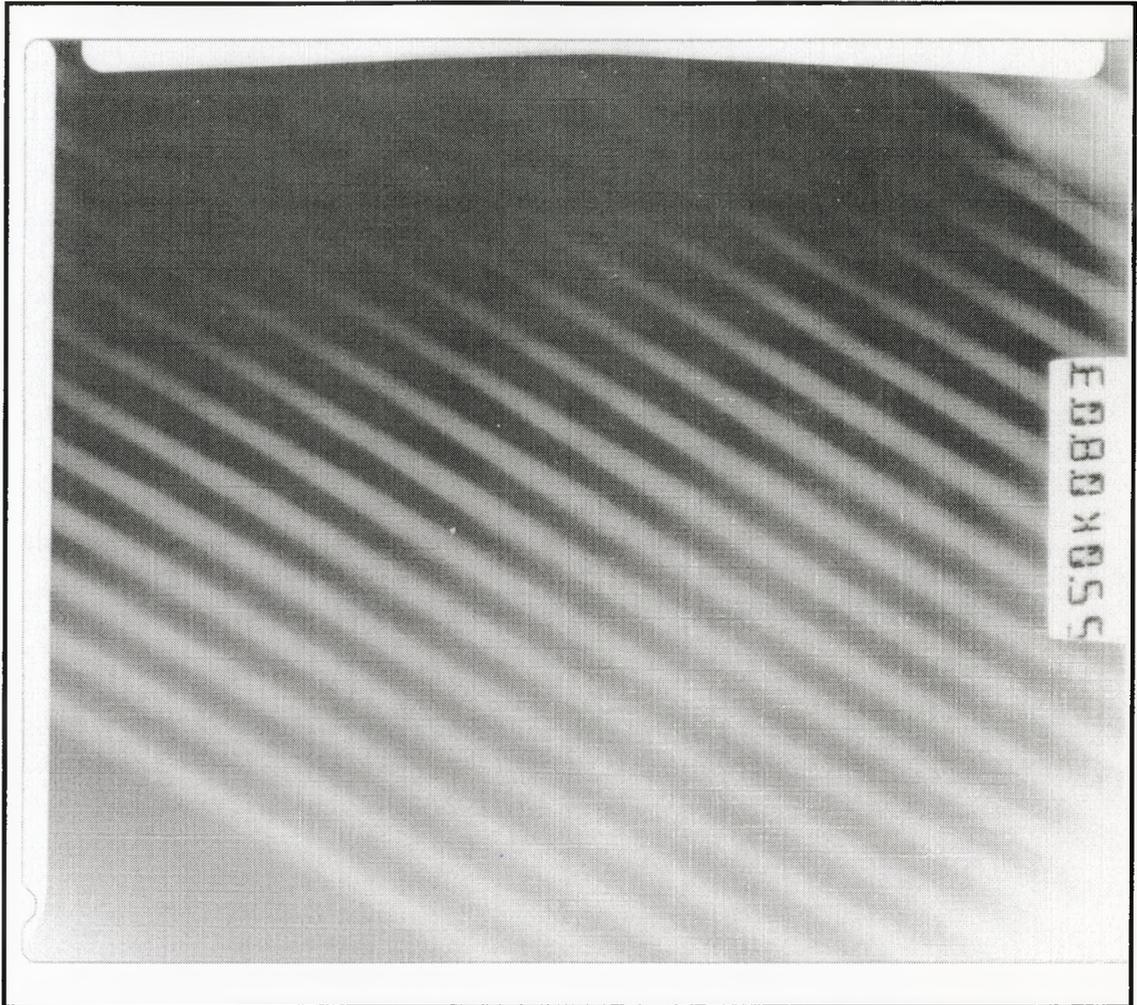
Figure 4.5.1: TEM micrograph of all 40 layers of the InP/InGaAsP super-lattice structure.

As Figure 4.5.1 demonstrated, the strategy for measuring layer thickness precisely and effectively had to be rethought. It was determined that the best approach to measuring layer thickness variations would be to take images at high magnification of the first dozen layers (closest to substrate) and then compare those with images taken at the same magnification of the topmost dozen layers. Figures 4.5.2(a & b) display the micrographs of the bottom and top dozen layers of the DBR stack. Theses images were taken at a magnification of 60,000. Extreme care was taken to ensure the best contrast between the binary and quaternary layers.

(a)   *(b)*
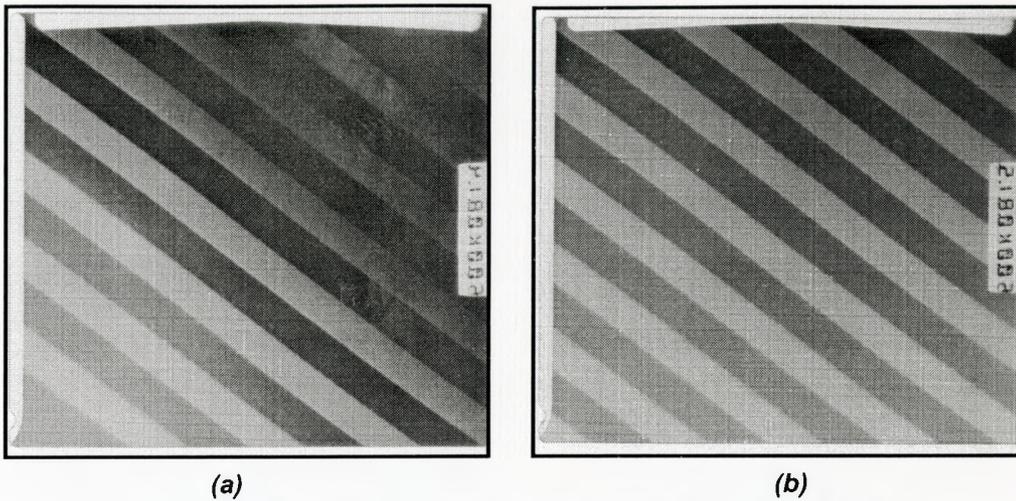
Figure 4.5.2: TEM micrographs of (a) bottom dozen layers and
(b) top dozen layers of InP/InGaAsP DBR stack.

The micrographs of Figure 4.5.2 are noticeably sharper than those of Figure 4.5.1 and provide an opportunity for making thickness measurements and comparisons. To begin, the micrographs were digitized at a 1:1 ratio and imported into AutoCAD 2000. Using the precision measuring tools of the program, the first and last twelve layer thicknesses of the DBR stack were measured. The results of these measurements are displayed in Table 4.5.1. It is important to note that some uncertainty was involved in the measurements as there was not a single definite line defining the start and end of layer. As a result, an error of 0.03cm is attached to each layer thickness measurement. This error is the end result of the average thickness of the 'grey' region between layers.

Table 4.5.1: Layer thickness measurements of bottom and
top dozen layers of InP/InGaAsP DBR stack.

Layer Number	Thickness of Bottom Dozen Layers[a]		Thickness of Top Dozen Layers[b]	
	Magnified	**Actual**	**Magnified**	**Actual**
1	0.71 ± 0.03 cm	118.3 ± 5.0 nm	0.67 ± 0.03 cm	111.7 ± 5.0 nm
2	0.66 ± 0.03 cm	110.0 ± 5.0 nm	0.69 ± 0.03 cm	115.0 ± 5.0 nm
3	0.69 ± 0.03 cm	115.0 ± 5.0 nm	0.66 ± 0.03 cm	110.0 ± 5.0 nm
4	0.67 ± 0.03 cm	111.7 ± 5.0 nm	0.67 ± 0.03 cm	111.7 ± 5.0 nm
5	0.66 ± 0.03 cm	110.0 ± 5.0 nm	0.68 ± 0.03 cm	113.3 ± 5.0 nm
6	0.68 ± 0.03 cm	113.3 ± 5.0 nm	0.69 ± 0.03 cm	115.0 ± 5.0 nm
7	0.65 ± 0.03 cm	108.3 ± 5.0 nm	0.65 ± 0.03 cm	108.3 ± 5.0 nm
8	0.69 ± 0.03 cm	115.0 ± 5.0 nm	0.67 ± 0.03 cm	111.7 ± 5.0 nm
9	0.66 ± 0.03 cm	110.0 ± 5.0 nm	0.68 ± 0.03 cm	113.3 ± 5.0 nm
10	0.70 ± 0.03 cm	116.7 ± 5.0 nm	0.69 ± 0.03 cm	115.0 ± 5.0 nm
11	0.67 ± 0.03 cm	111.7 ± 5.0 nm	0.66 ± 0.03 cm	110.0 ± 5.0 nm
12	0.68 ± 0.03 cm	113.3 ± 5.0 nm	0.67 ± 0.03 cm	111.7 ± 5.0 nm

[a] Layer 1 refers to layer closest to the substrate.

[b] Layer 1 refers to the topmost layer.

Despite the improvement in the clarity of Figure 4.5.2 in comparison to that of Figure 4.5.1, the measurements made of the bottom and top dozen layers of the stack still do not provide enough precision to distinguish between individual layer thicknesses. The data in Table 4.5.1 however does allow for a rough comparison of the layer thicknesses between the top and bottom most layers of the stack. As can be seen, there is no noticeably large difference between the top and bottom layer thicknesses thus confirming the experimental results.

In a last attempt to examine the thickness wandering issue, images of the three bottom and top most layers were taken at a magnification of 200,000. Figures 4.5.3(a & b) provide a copy of the micrographs.

(a)   *(b)*
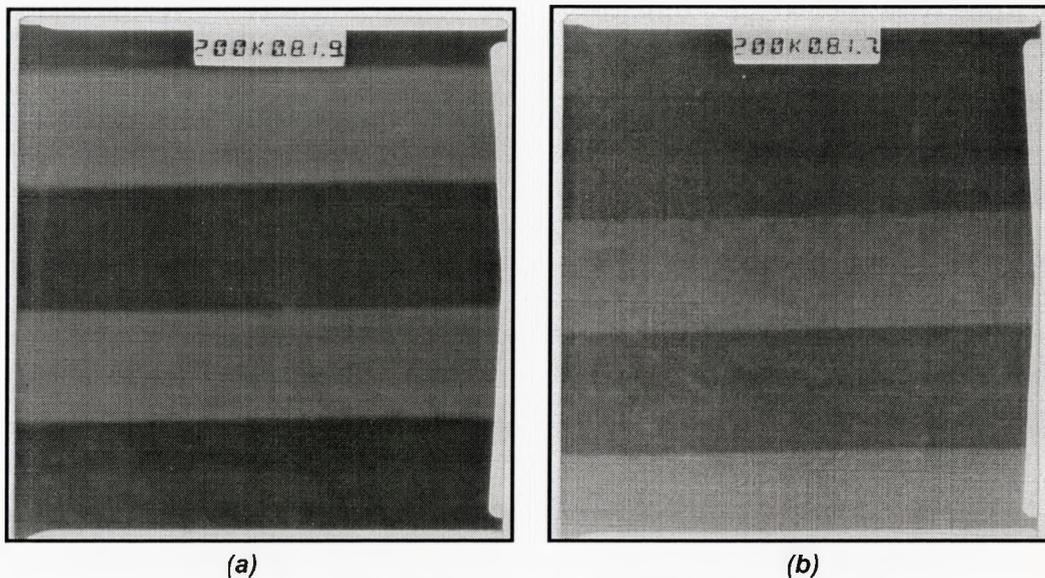
Figure 4.5.3: TEM micrographs of (a) bottom three layers and (b) top three layers of InP/InGaAsP DBR stack.

The same approach was used to measure the thicknesses of the layers for Figure 4.5.3. Once again, contrast problems prevented precise measurements that would allow for the differentiation of individual layer thicknesses. In fact, the error associated with this set of measurements is even larger than for the 60,000 magnification micrographs of Figure 4.5.2 at ±0.08cm. However, comparison of top and bottom layers was possible through careful measurements and the results can be found in Table 4.5.2. Once again,

the figures in Table 4.5.2 confirm to an extent that thickness wandering was not a significant issue in this DBR stack.

Table 4.5.2: Layer thickness measurements of bottom and top three layers of InP/InGaAsP DBR stack.

Layer Number	Thickness of Bottom Dozen Layers[a]		Thickness of Top Dozen Layers[b]	
	Magnified	Actual	Magnified	Actual
1	2.15 ± 0.08 cm	107.5 ± 4.0 nm	2.26 ± 0.08 cm	113.0 ± 4.0 nm
2	2.28 ± 0.08 cm	114.0 ± 4.0 nm	2.12 ± 0.08 cm	106.0 ± 4.0 nm
3	2.19 ± 0.08 cm	109.5 ± 4.0 nm	2.27 ± 0.08 cm	113.5 ± 4.0 nm

[a] Layer 1 refers to layer closest to the substrate.

[b] Layer 1 refers to the topmost layer.

From the above discussion, it can be concluded that transmission electron microscopy could be a very useful tool in the analysis of the DBR super-lattice from a macro prospective. However, its application on a layer-by-layer basis proves to be useless with the tools and approach utilized here. Unless another method is developed to better suit the difficulties surrounding contrast issues at the interface between layers, TEM analysis can only be used for determination of reproducibility of thicknesses.

4.6 X-Ray Analysis of the DBR Stack

X-ray analysis of the DBR stack was carried out using the Bede Scientific Instruments QC1 double-crystal diffractometer. This system operates by transmitting a beam of x-rays through a micro slit to create a highly collimated beam. The collimated x-rays are then incident onto a reference crystal (typically composed of the same material as the substrate of the test sample) at the Bragg angle. This process further collimates the beam as it is reflected off the reference crystal and onto the sample. The sample is placed on a rotating/tilting stage parallel to the reference crystal in order to maintain the Bragg condition and provide maximum reflection of the x-rays into a large area detector for detection and analysis [28].

The objective of the x-ray analysis was to determine the periodicity of the growth with respect to layer thicknesses. This was achieved by first running an x-ray scan on the 20 pair InP/InGaAsP DBR stack. The results of this scan can be found in Figure 4.6.1.
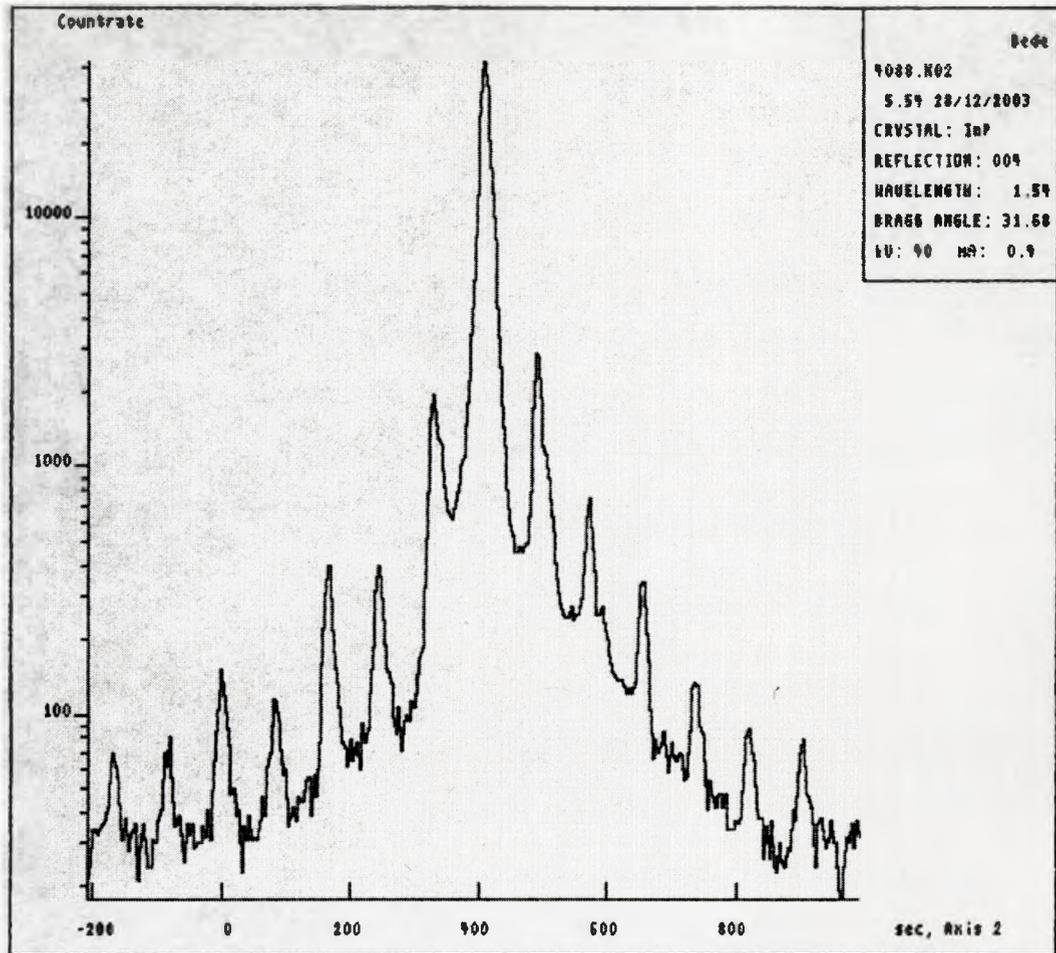
Figure 4.6.1: X-ray scan of a 20 pair InP/InGaAsP DBR stack.

The peaks in Figure 4.6.1 correspond to the interfaces between the binary and quaternary layers in the stack. The centermost peak represents the InP substrate and since it is a large single peak, it can be concluded that the stack is lattice matched to the substrate. With further analysis, it can be observed that the peaks to the left and right of the centermost peak are symmetrical and display an alternating high/low intensity. In addition, the distances between these peaks are regular at about 100 arc seconds confirming the consistency in the periodicity of the DBR stack.

To further analyze the validity of the x-ray measurement and determine the effects of minor changes in the DBR stack, an x-ray simulation was carried out using the both the original and most recent versions of the Bede simulation software. The outcome of

the first simulation using the original software can be found in Figure 4.6.2. A quick comparison of the simulated results to the experimental results reveals that the peaks in both plots are in good agreement with one another. In addition, the high/low sequences of peaks as well as the symmetry are conserved. The only noticeable difference is the sharpness of each peak along with the exaggeration of the high/low nature of the peaks.
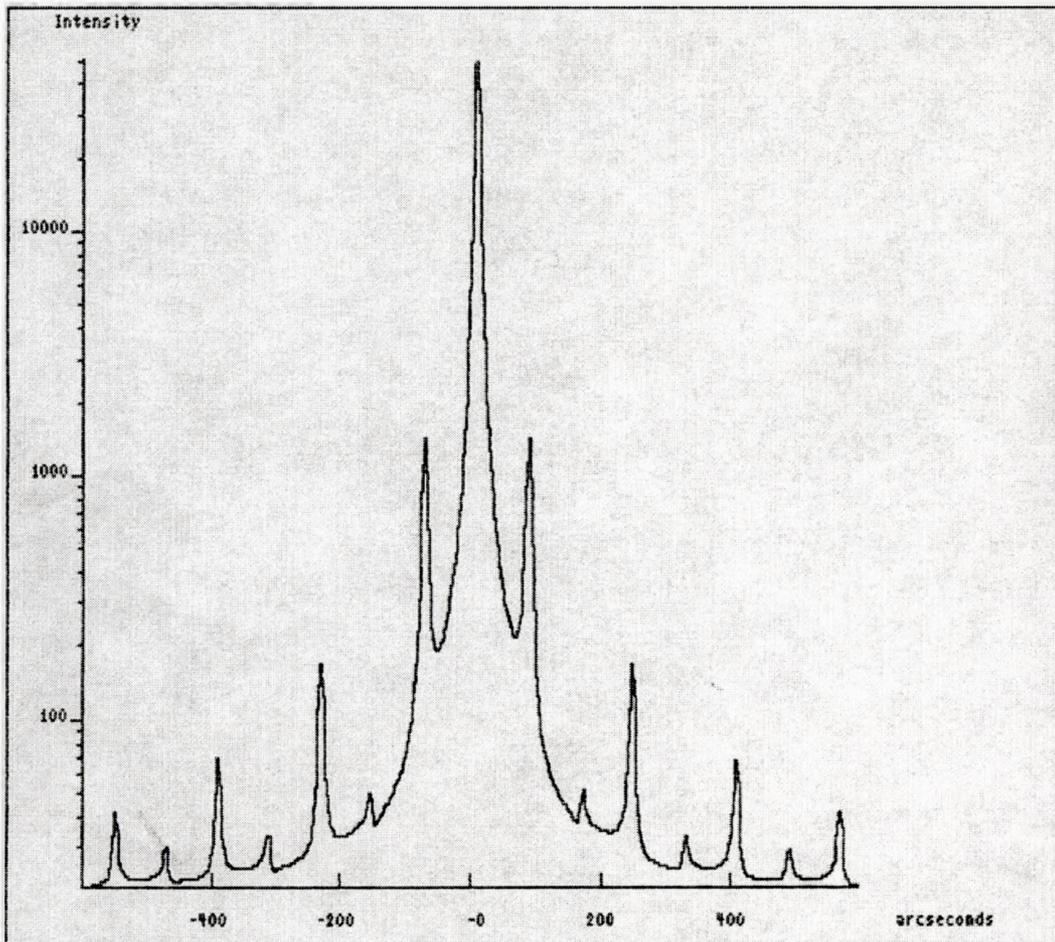
Figure 4.6.2: X-ray simulation of 20 pair InP/InGaAsP
DBR stack using Bede original software.

The results of the simulation conducted by the latest version (Version 3.0) of the Bede software can be found in Figure 4.6.3. Once again, the same characteristics as found in the original simulation along with the actual measurements can be seen here.
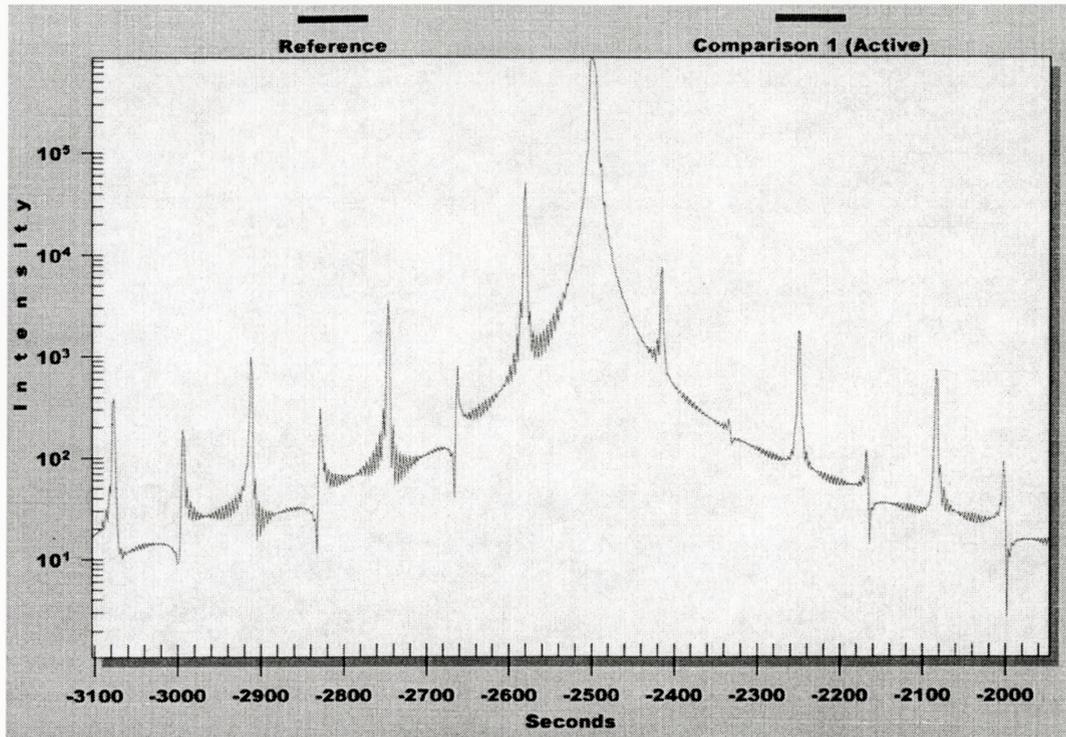
Figure 4.6.3: X-ray simulation of a 20 pair InP/InGaAsP
DBR stack using Bede Version 3.0 software.

For further investigation, some perturbations were made to the model in Figure 4.6.3. The first adjustment was made to the composition of the first 6 pairs. The gallium concentration was increased by 2.5% or 8 parts in 320. Figure 4.6.4 depicts the effects of this very minor change. As can be seen, the signal becomes noticeably "noisier" while the peaks tend to have broadened. Also, a compositional average peak has emerged just to the right of substrate peak relating the slight lattice mismatch.

Figure 4.6.5 provides the simulation results displaying a thickness change of 2.1% in the first 6 pairs of the quaternary layers. The only noticeable change is in the intensity of the peaks.
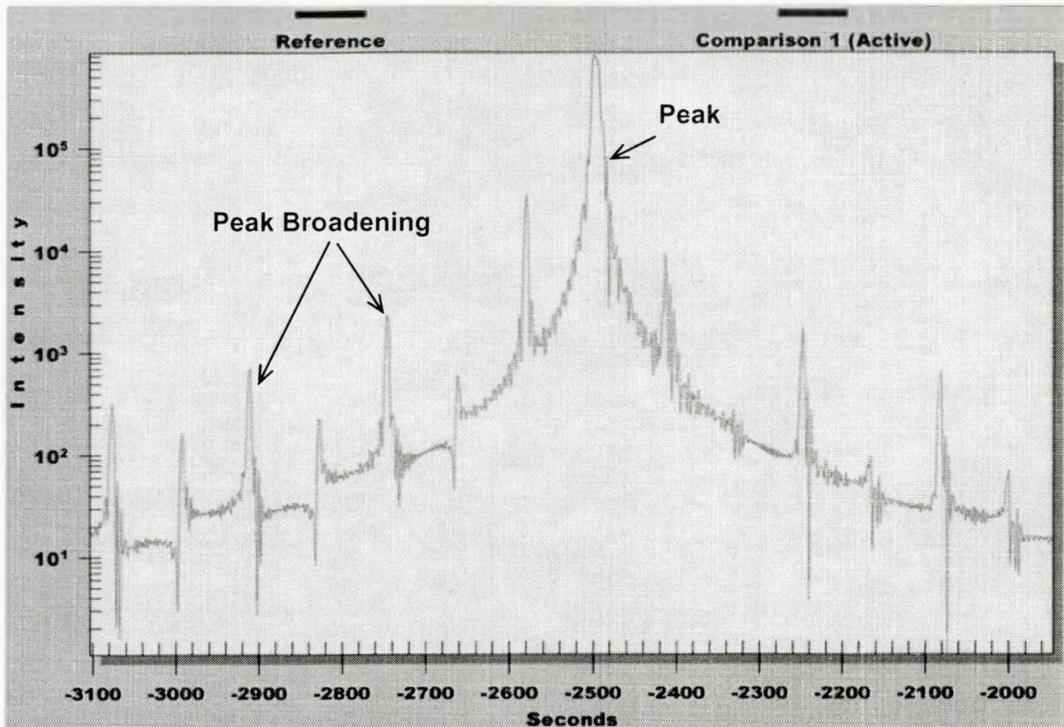
Figure 4.6.4: X-ray simulation of a 20 pair InP/InGaAsP DBR stack with a slight compositional change using Bede Version 3.0 software.
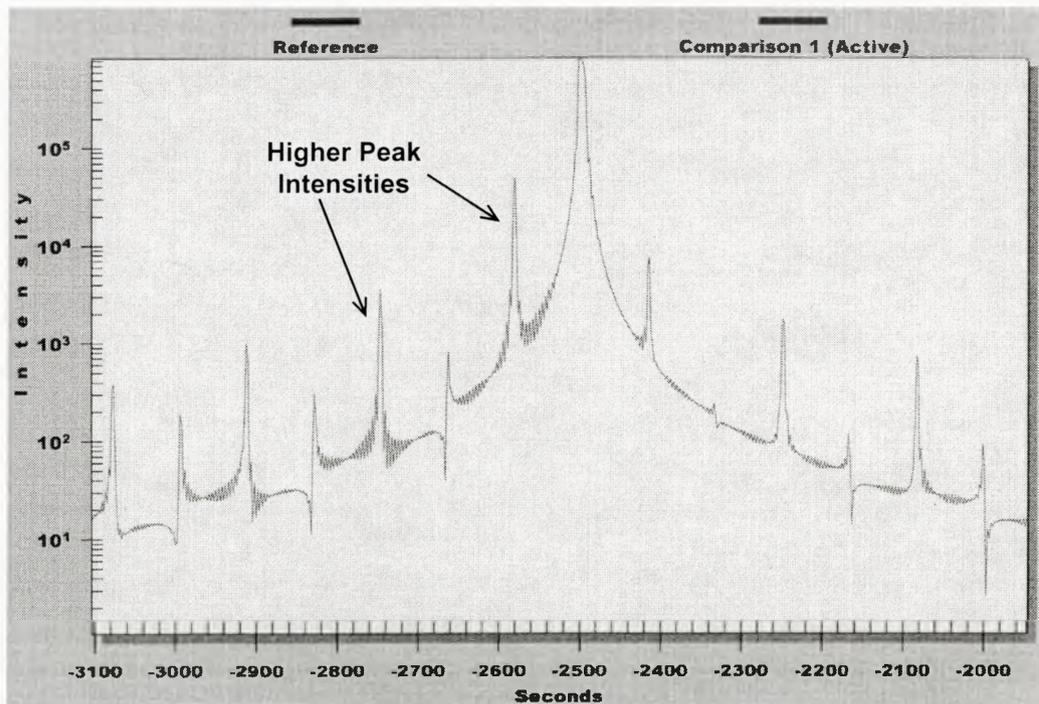
Figure 4.6.5: X-ray simulation of a 20 pair InP/InGaAsP DBR stack with a slight thickness change using Bede Version 3.0 software.

Despite the fact that neither of the simulations, including the ones with perturbations, were an exact match to the actual x-ray measurements, they still provided some insight and support of thethe stack composition and periodicity.

4.7 Compositional Analysis of the DBR Stack

Thus far, the investigation has been focused on the layer thicknesses of the InP/InGaAsP DBR stack in light of the curve fitting in Section 4.3. However, in order to confirm that the chemical composition of the quaternary is as designed and repeatable throughout the entire super-lattice structure, photoluminescence (PL) measurements were carried out on the DBR samples. It is important to note that the light source used in the PL system stimulates a response only from the topmost two quaternary layers due to absorption and losses in the material. Hence, by examining all the etched-back DBR samples with different numbers of pairs, chemical composition of the quaternary may be established.

Furthermore, a quick PL scan of a sample can uncover the existence of any incomplete layers left behind as a result of incomplete etching. The existence of such a layer becomes evident by examining the PL intensity. In the case of a poorly etched sample (incomplete etch of topmost layer), the PL intensity is on the order of a half to a third of that observed from a carefully processed sample. This is due to absorption caused by the undesired layer.

To obtain a standard for the PL scans, a calibration quaternary sample with the same composition as that of the DBR's quaternary was first analyzed. The result of this scan can be found in Figure 4.7.1. Figure 4.7.2 shows the PL scans obtained from the DBR stacks on a normalized scale for ease of comparison. Each sample was analyzed at least twice making sure that each measurement was taken at different points on the sample to ensure well averaged results.

PL Measurement of InGaAsP Calibration Quaternary
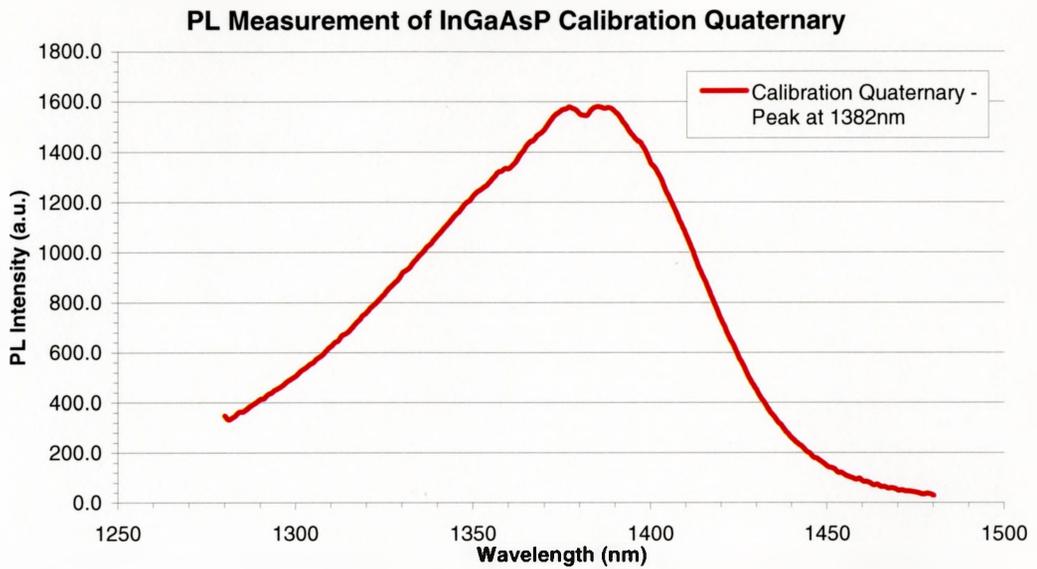
Figure 4.7.1: PL measurements taken for calibration purposes from a InGaAsP quaternary with identical composition as found in DBR stack.

PL Measurements of InP/InGaAsP DBR Stacks with Various Pairs
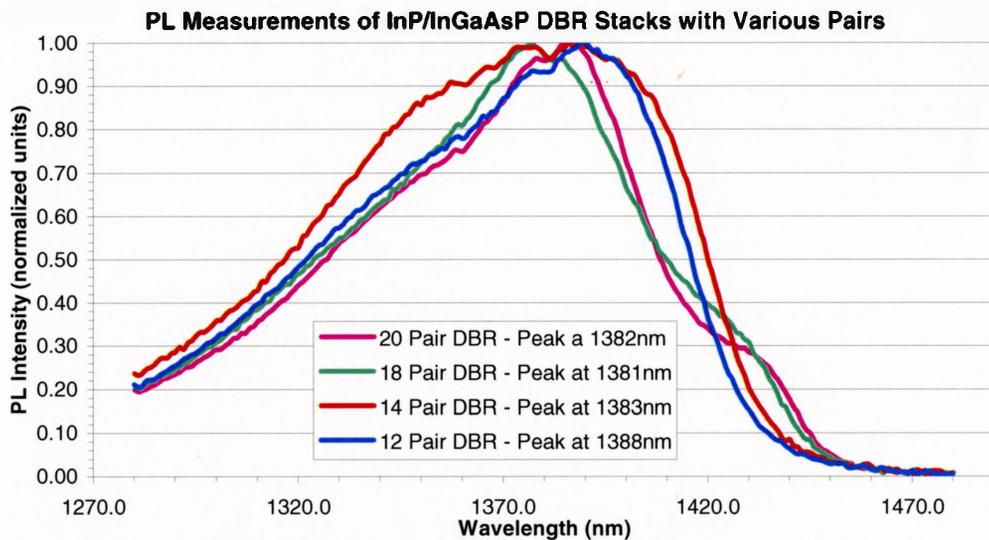
Figure 4.7.2: PL measurements taken from DBR stacks.

Examination of Figures 4.7.2 reveals that the DBR stack's composition varies by a negligible amount. This is determined by comparing the peaks of the PL measurements for the DBR stack to those of the calibration curve. The largest variation from the 1382nm calibration peak (band gap of 0.897eV) occurs for the 12 pair DBR stack with a

peak at 1388nm (band gap of 0.893eV). This 6nm or 3.88×10^{-3} eV difference translates into a compositional change of 0.83% for x and 2.7% for y components of the quaternary, respectively. In other words, the original quaternary composition would change from $In_{0.64}Ga_{0.36}As_{0.777}P_{0.223}$ to $In_{0.637}Ga_{0.363}As_{0.783}P_{0.217}$. This minor compositional variance has almost no effect on the index of refraction calculations (results in a change of 0.023% of index at the center wavelength of 1510nm). It is for this reason that no vertical adjustments were required during curve fitting in Section 4.3.

4.8 Summary of Analysis

Several characterization tools were used to analyze the 20 pair InP/InGaAsP DBR stack. Through reflectivity measurements, it was determined that there existed a slight difference between the specified growth thicknesses and the as grown sample. For the InP layer, the thickness was altered from the theoretically calculated value of 122.2nm to 117.5nm while the quaternary thickness went from 111.5nm to 108.0nm. The quality of the fits was satisfactory, however, they could be improved with more care taken during measurement scans.

Transmission electron microscopy along with x-ray analysis revealed the successful repeatability and consistency of the stack pairs from start to finish of the growth. Photoluminescence was used to analyze the composition of the quaternary layers in the stack. By comparing the peaks in the PL scans for the various samples, it was concluded that almost no compositional change was present throughout the DBR stack.

5. Experimental Results and Analysis for GaAs/InGaP DBR

5.1 Sample Preparations

The GaAs/InGaP DBR was designed and fabricated solely as a test to reconfirm all of the calculation procedures as well as the reflectivity measurement setup for yet another sample. Errors may have been present with the last sample and gone undiscovered, thus the analysis of another sample is necessary.

To begin, the as-grown sample was cleaved into three equal segments and prepared for etching. The desired number of layers for each sample was chosen to be:

a) 20 pair DBR sample (no etching required)

b) 19 pair DBR sample

c) 14 pair DBR sample

It is important to note that the 19 pair etched DBR sample was deliberately chosen to test the capabilities of the reflectivity measurement setup in terms of resolution.

The removal of the unwanted pairs from the super-lattice was done using a wet chemical etch. The etchant for the ternary layer was $HCl:H_3PO_4$ (1:3), with an etch rate of $0.4 \mu m/min$ [23]. The etchant for the GaAs layers was $H_2SO_4:H_2O_2:H_2O$ (1:8:40), with an etch rate of $0.1 \mu m/min$ [23]. After etching, reflectivity measurements were carried out, as before, at incident light angles of 0°, 12°, 24°, and 36°.

5.2 Variable & Normal Incidence Measurements

The reflectivity measurements were conducted in the exact same fashion as those described in Section 4.2. The first sample to be tested was the as grown sample. The resultant normal incidence reflectivity curve of this measurement can be found in Figure 5.2.1. As can be seen, the result is in no way close to the theoretical predictions of Chapter 3 and hence is cause for alarm. However, after some discussion with Brad Robinson (MBE operator), it was determined that an extra half layer had been grown resulting in 20.5 pairs. Consequently, the sample was etched to remove this extra half layer present on the as grown sample. Subsequent etches removed the layers in pairs. Figures 5.2.2 (a to c) depict the reflectivity measurement results.

Normal Incidence Reflectivity Measurement of As Grown GaAs/InGaP DBR Stack
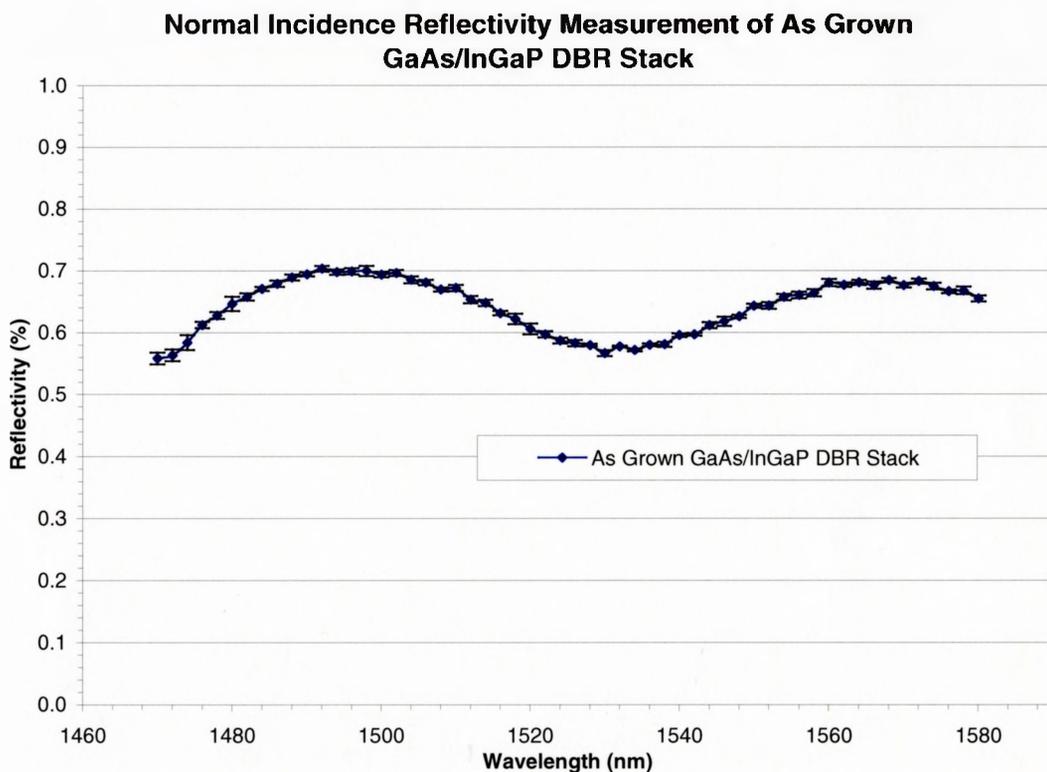
Figure 5.2.1: Normal incidence reflectivity measurements of as grown DBR stack with 20.5 pairs.

M.A.Sc. Thesis – M. Shahideh. McMaster – Engineering Physics

66
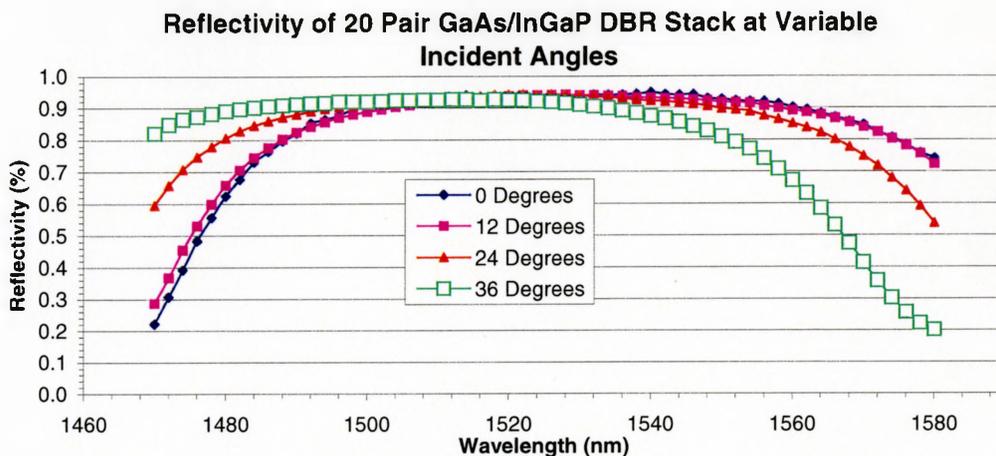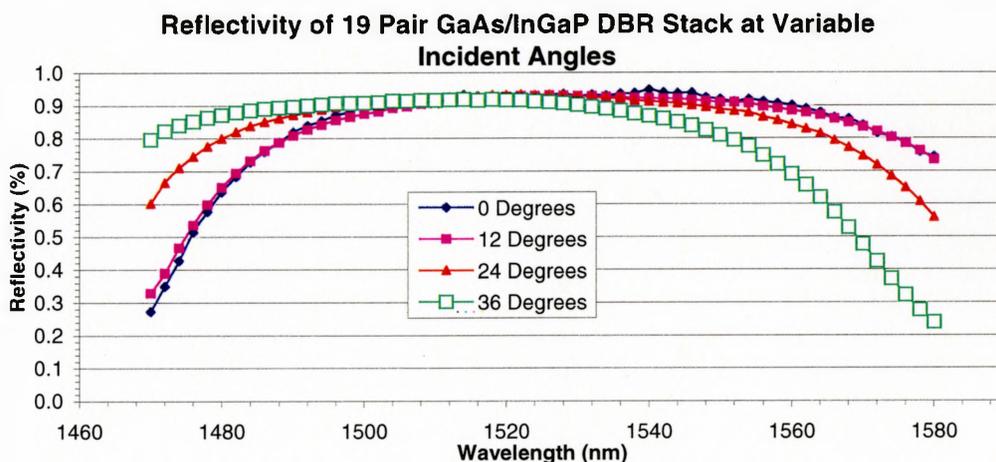
Figure 5.2.2(a)
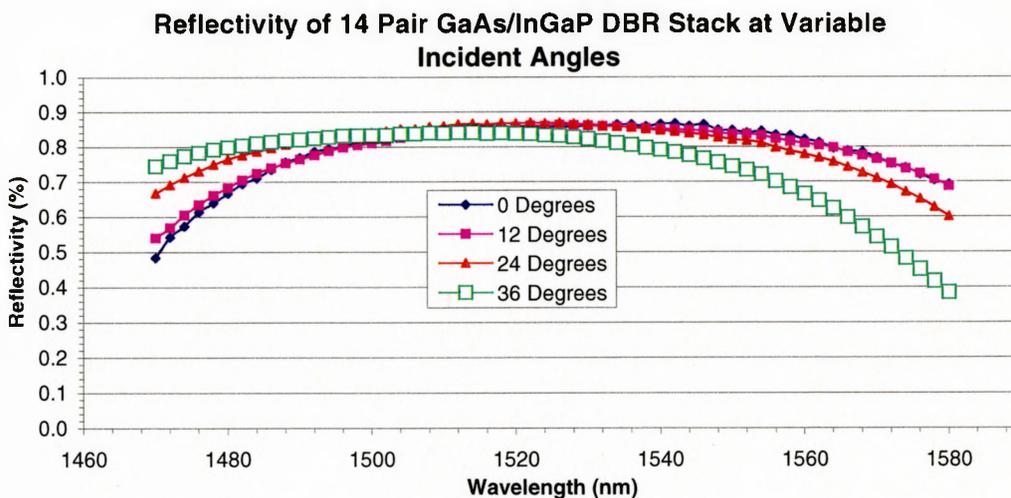
Figure 5.2.2(b)

Figure 5.2.2(c)

Visual analysis of Figures 5.2.2 (a to c) reveals that the desired center wavelength of 1550nm was slightly blue shifted to roughly 1532nm. This evident shift is, however, observed in all three samples translating to a root cause that is present throughout the entire super-lattice. Further examination reveals that the reflectivity is at the theoretically predicted value of roughly 95% for the 20 pair stack. Consequently, as was discussed in Section 4.3, the key cause of this shift is most likely the result of minor thickness errors. Figure 5.2.3 plots the predicted reflectivity curve of the 20 GaAs/InGaP DBR stack with the experimentally obtained curve at normal incidence.
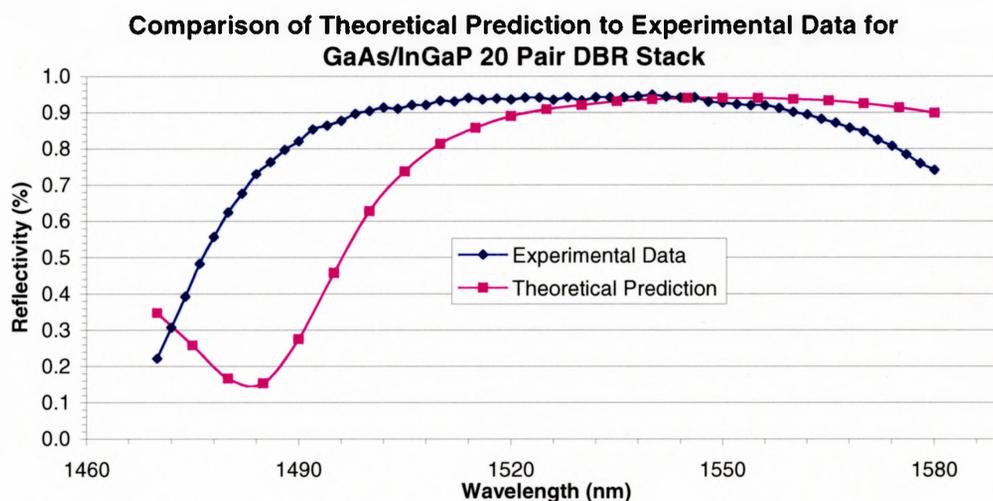
Figure 5.2.3: Theoretical predictions of 20 pair GaAs/InGaP DBR stack with experimentally obtained data.

The variable angle data obtained from Figures 5.2.2 (a to c) display a blue shift in the placement of the curve as the incident angle is increased. The larger the incident angle, the larger the shift. This is in agreement with the results obtained from the InP/InGaAsP DBR stack as well as the theoretical calculations. Once again, the path length difference from the normal incidence measurement and the 12° incident measurement is so small, that almost no change is noticeable between the two curves. For improved visualization, Figures 5.2.4 and 5.2.5 illustrate the theoretical reflectivity over a broad spectral window as well as at different incident light angles respectively for all three stacks.

GaAs/InGaP Theoretical Reflectivity at Normal Incidence
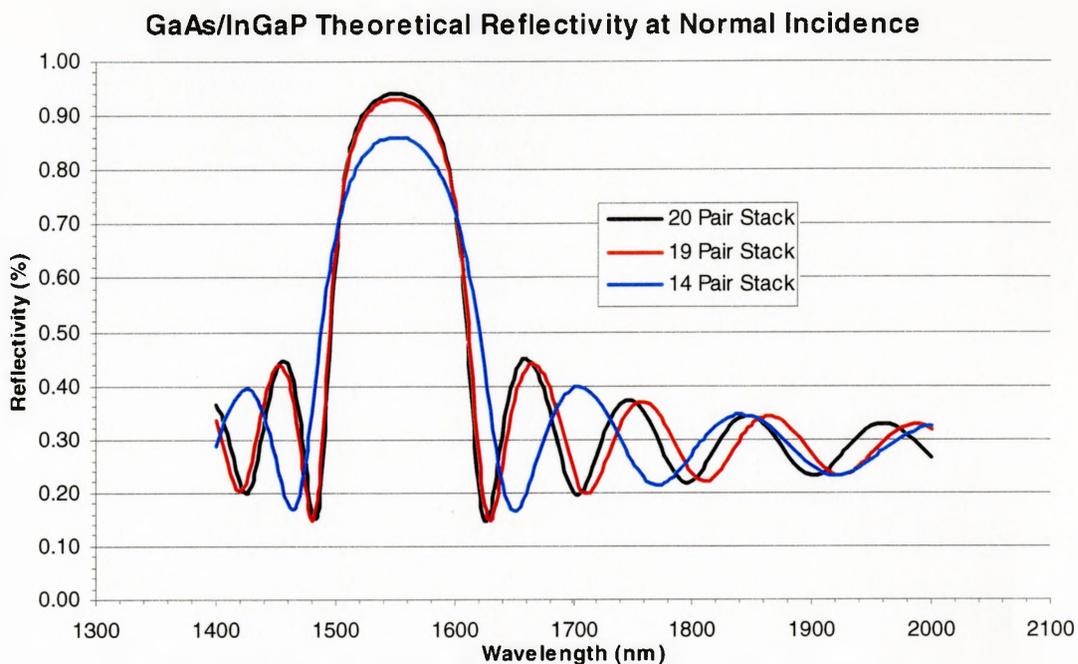
Figure 5.2.4: Theoretical Reflectivity of GaAs/InGaP DBR stack with various numbers of pairs at normal incidence.

Variable Incident Angles for 20 Pair GaAs/InGaP DBR Stack
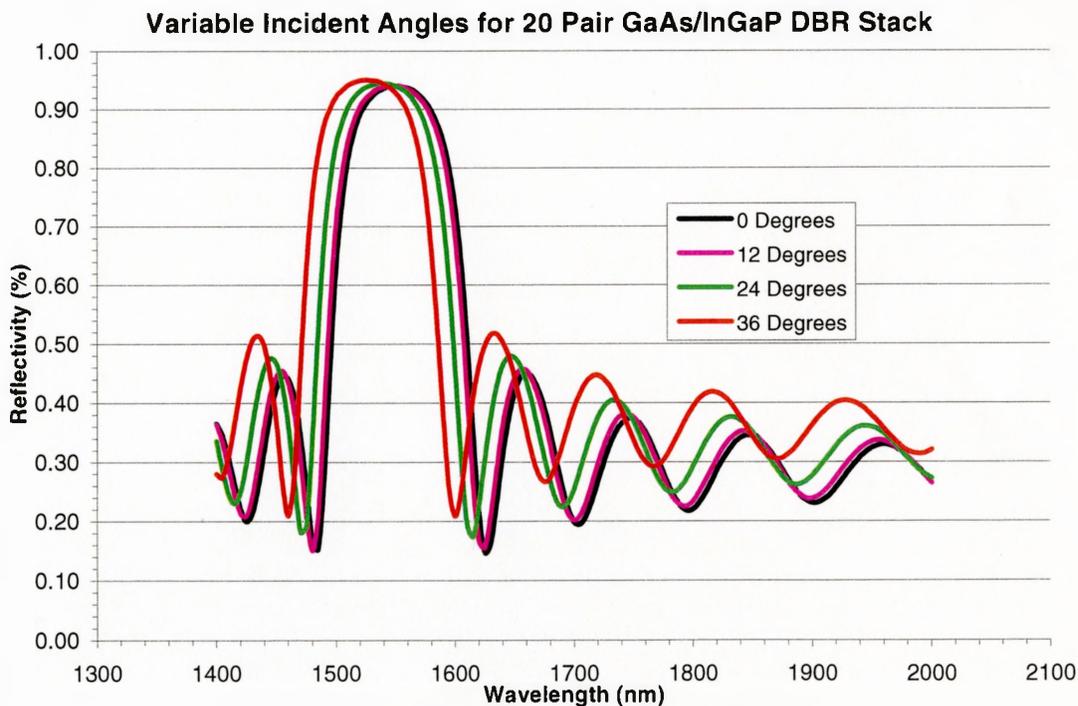
Figure 5.2.5: Variable incident reflectivity measurement of 20 pair GaAs/InGaP DBR stack.

5.3 Theoretical Curve Fitting to Experimental Data

The curve fitting approach used for the GaAs/InGaP stack is the exact same as that used in Section 4.3 for the InP/InGaAsP DBR stack. This approach is valid in this scenario due to the nature of the shifts present in the experimental data. Had the blue shifts not been constant between the various numbers of stacks in the three samples, then other measures would have to be taken in order to fit the data.

Using trial and error in conjunction with the least squares method, the thicknesses of the two layers were altered until a best fit was obtained. The change to the theoretical thickness values saw the GaAs thickness decrease from 114.99nm to 114.0nm and the InGaP thickness decrease from 123.82nm to122.0nm. The results of these fits are illustrated in Figure 5.3.1 through to 5.3.3.

(a) 0° incidence

(b) 12° incidence

(c) 24° incidence

(d) 36° incidence
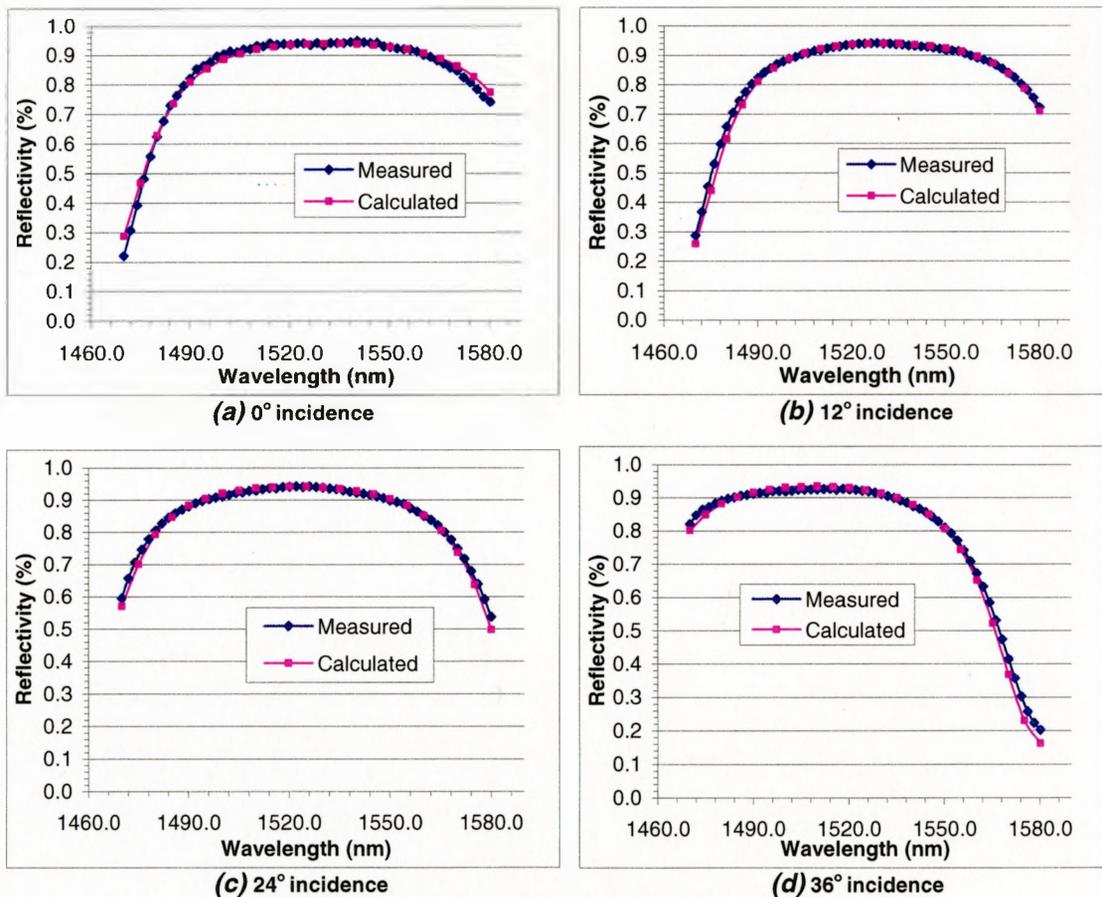
Figure 5.3.1: Theoretical fit to experimental data of
20 pair GaAs/InGaP DBR stack.
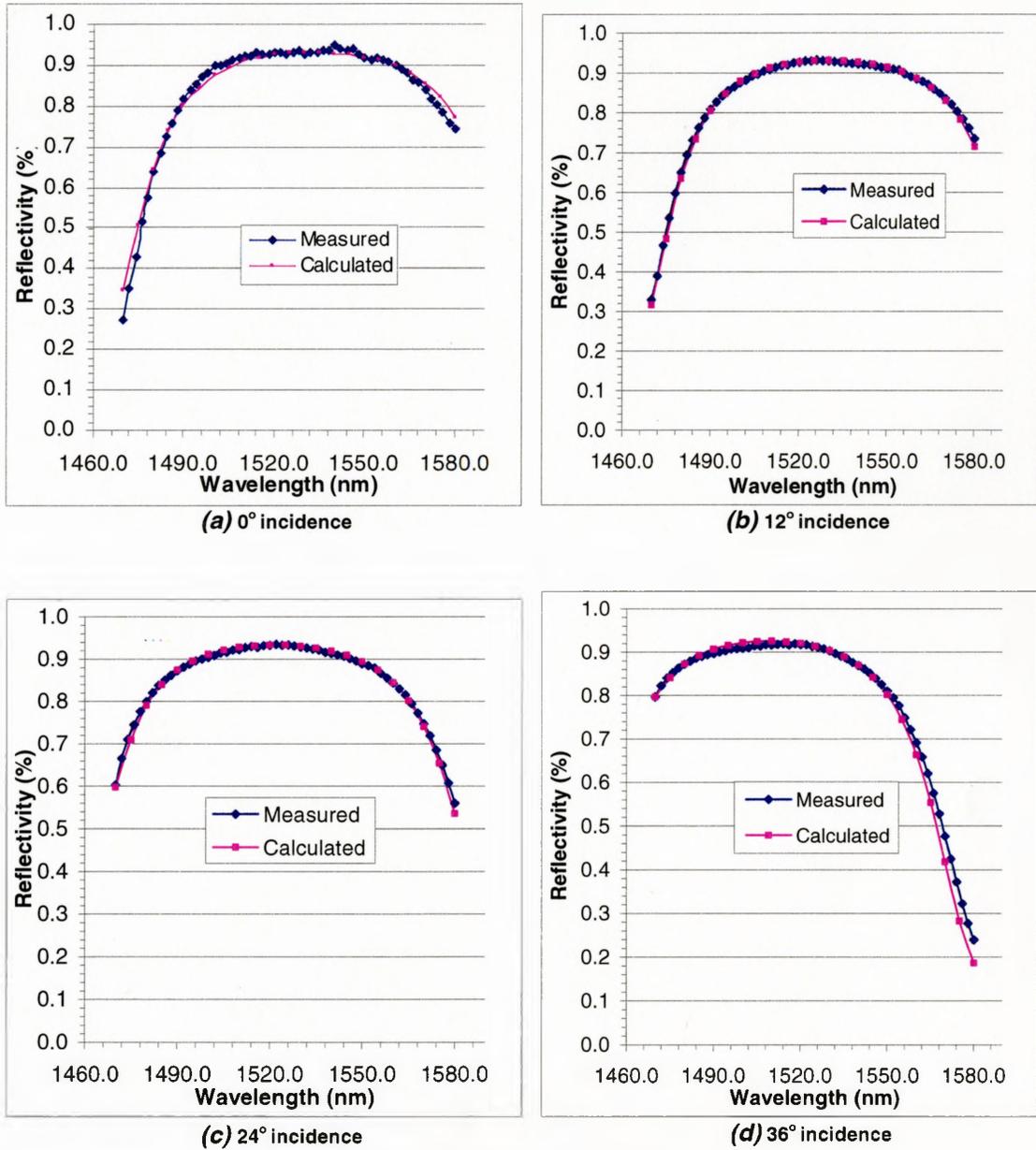
Figure 5.3.2: Theoretical fit to experimental data of 19 pair GaAs/InGaP DBR stack.

(a) 0° incidence

(b) 12° incidence

(c) 24° incidence

(d) 36° incidence
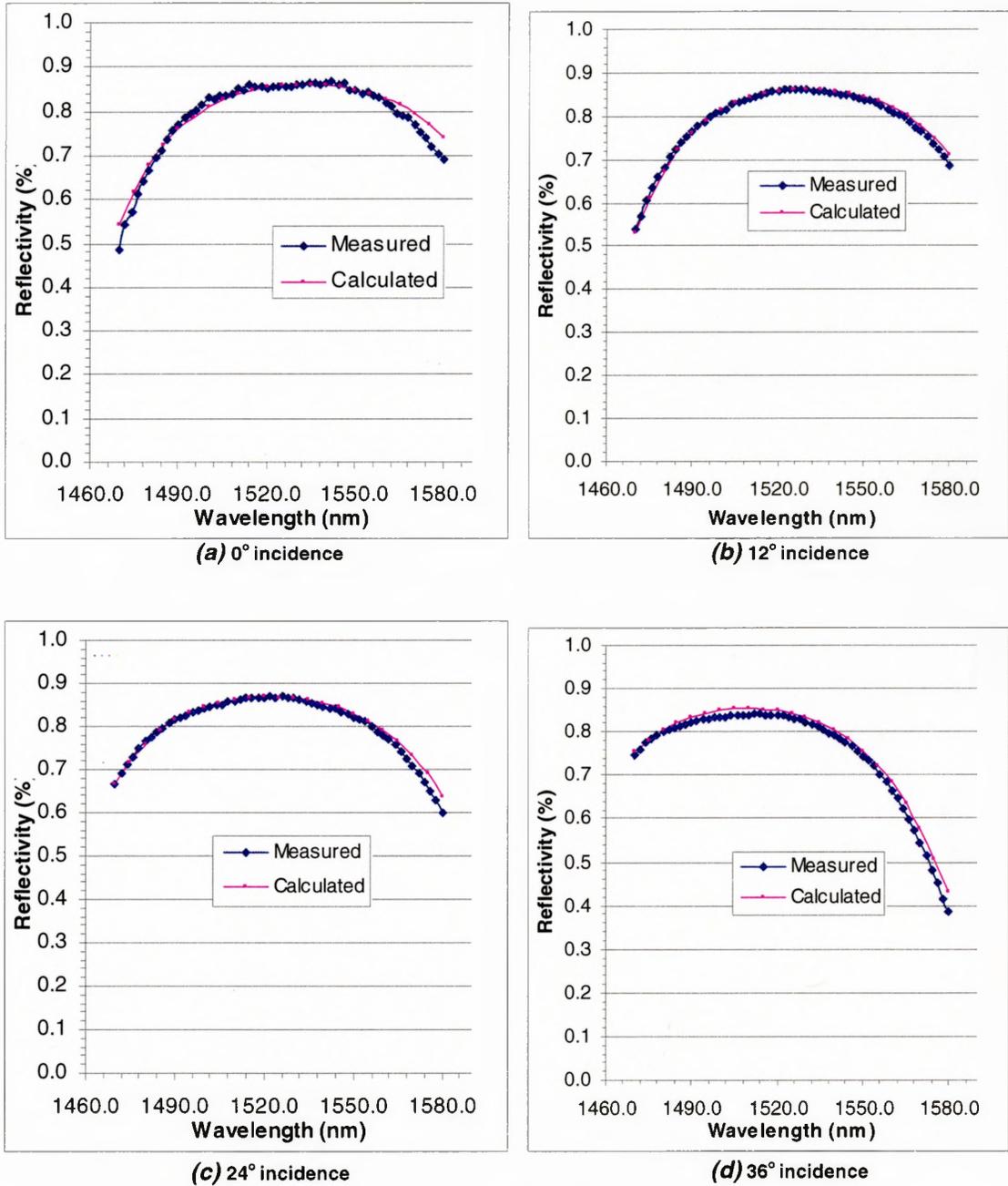
Figure 5.3.3: Theoretical fit to experimental data of 14 pair GaAs/InGaP DBR stack.

The theoretical fits obtained for this particular DBR stack are much more accurate than those obtained for the last sample. This is largely due to the fact that greater care was taken in ensuring that the sample surfaces were kept clean and scratch free. In addition, all reflectivity measurements were conducted overnight in order to avoid large room temperature fluctuations. Finally, all the measurements were conducted with the room lights kept on. This was even the case for the calibration process. The effects of these precautions are quite noticeable in Figures 5.3.1 through to 5.3.3.

The reflectivity measurement results for this DBR stack also solidify the capability and resolution of the measurement apparatus. In fact, the curves obtained for the 20 pair stack are quite distinguishable from those of the 19 pair stack. Hence, the GaAs/InGaP stack fulfilled its purpose of both testing and confirming the theoretical calculations as well as the reflectivity measurement setups.

5.4 X-Ray Analysis of DBR Stack

X-ray analysis was carried out on the 20 pair GaAs/InGaP DBR stack to check the periodicity and lattice matching of the structure. Figure 5.4.1 displays the results of the x-ray scan.

The center peak representing the GaAs substrate in the figure does not display any noticeable humps or split peaks. As a result, it is safe to conclude that lattice matching of the super-lattice to the substrate was done satisfactorily.
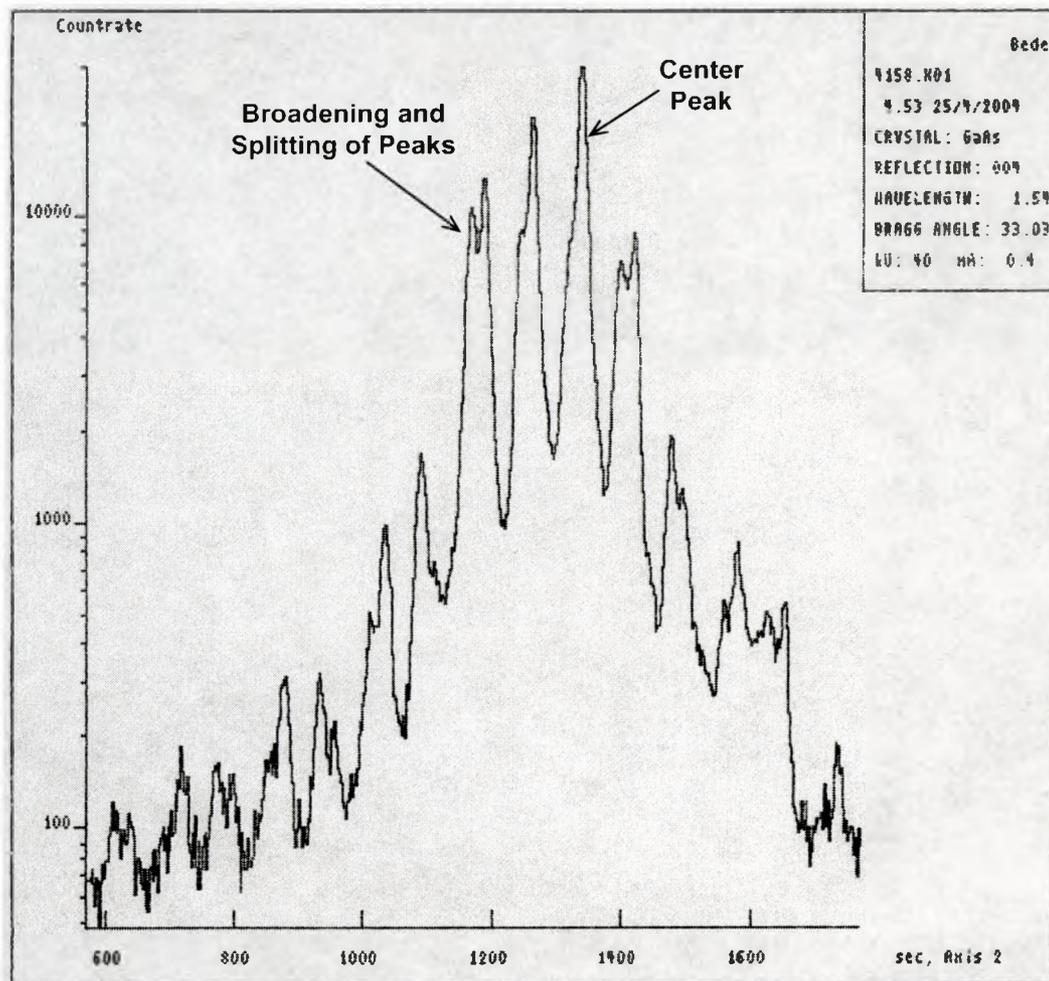
Figure 5.4.1: X-ray scan of the 20 pair GaAs/InGaP DBR stack.

Further analysis of Figure 5.4.1 reveals the presence of symmetry about the center GaAs substrate peak. The peaks found to the left and right of this center peak display some sort of split and broadening. In addition, they do not have the somewhat visible high/low characteristics observed in InP/InGaAsP DBR stack. The periodicity of the super-lattice is, however, maintained as peaks occur at roughly 80 arc second intervals.

Simulations were also performed for on this sample to provide a better understanding of the x-ray results. Figure 5.4.2 provides the simulation results using the original Bede software.

M.A.Sc. Thesis – M. Shahideh. McMaster – Engineering Physics

74
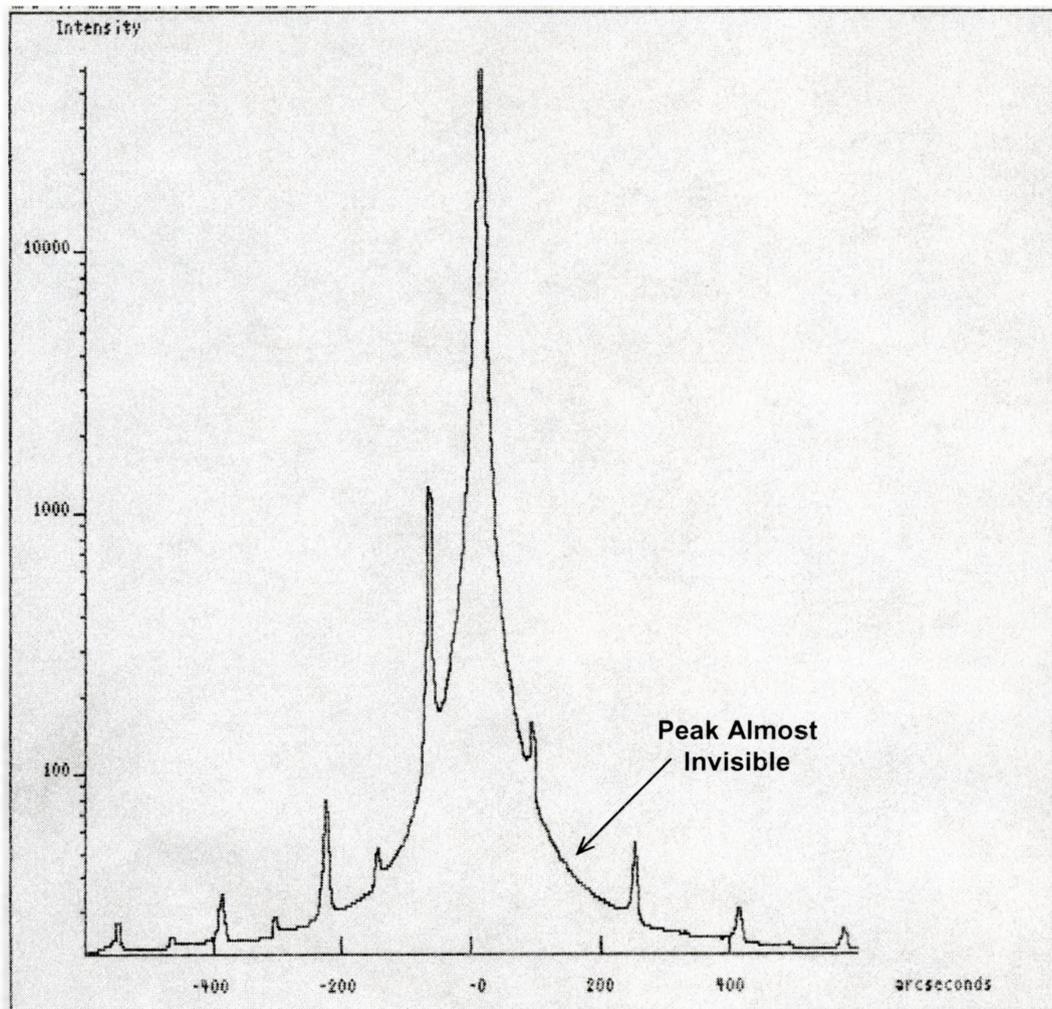
Figure 5.4.2: X-ray simulation of the 20 pair GaAs/InGaP
DBR stack using Bede original software.

Visually, Figure 5.4.2 barely resembles the experimentally obtained curve. However, closer inspection reveals a center peak with symmetric high/low peaks to its left and right. Despite the fact that the peaks in the simulation are much sharper, they do have the same periodicity of roughly 80 arc seconds as observed in the experimental curve.

The same simulation was repeated using the latest Bede software for comparison. The results of this simulation are illustrated in Figure 5.4.3. The majority of characteristics between the two simulations are quite similar with the exception of an additional peak present to the left of the GaAs substrate peak. This extra peak indicates

the existence a slight lattice mismatch between the super-lattice and GaAs substrate. The surprise is that this peak is neither present in the experimental scan nor the last simulation. Thus, the only explanation lies in the changes made to the form factors in the new software.
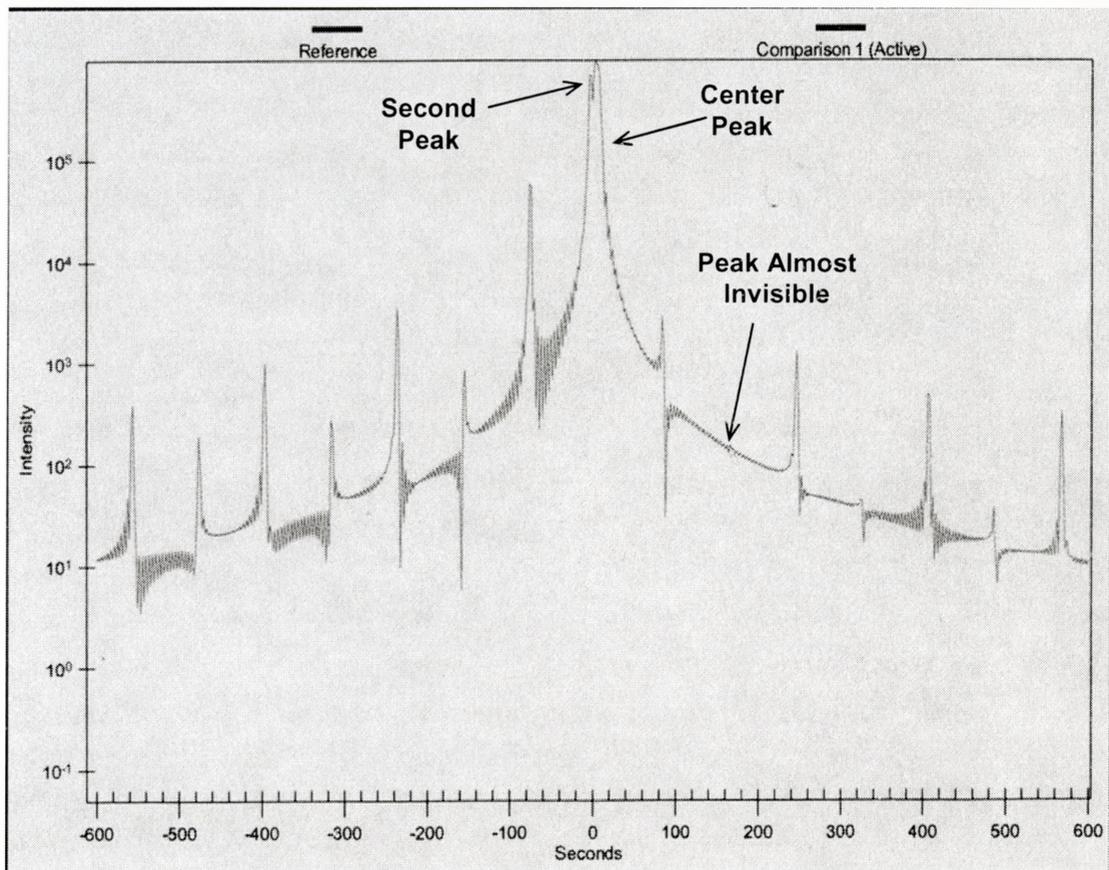
Figure 5.4.3: X-ray simulation of the 20 pair GaAs/InGaP DBR stack using Bede software Version 3.0.

In an attempt to discover the cause of peak broadening and splitting found in the experimental scan on the stack, slight alterations were made to the simulation models of the Bede Version 3.0 software. Initially, a compositional change of 1 part in 484 (increase) was made to the indium concentration in the ternary for the first 12 layers of the super-lattice. The results of this minor change are plotted in Figure 5.4.4.

M.A.Sc. Thesis – M. Shahideh. McMaster – Engineering Physics

76
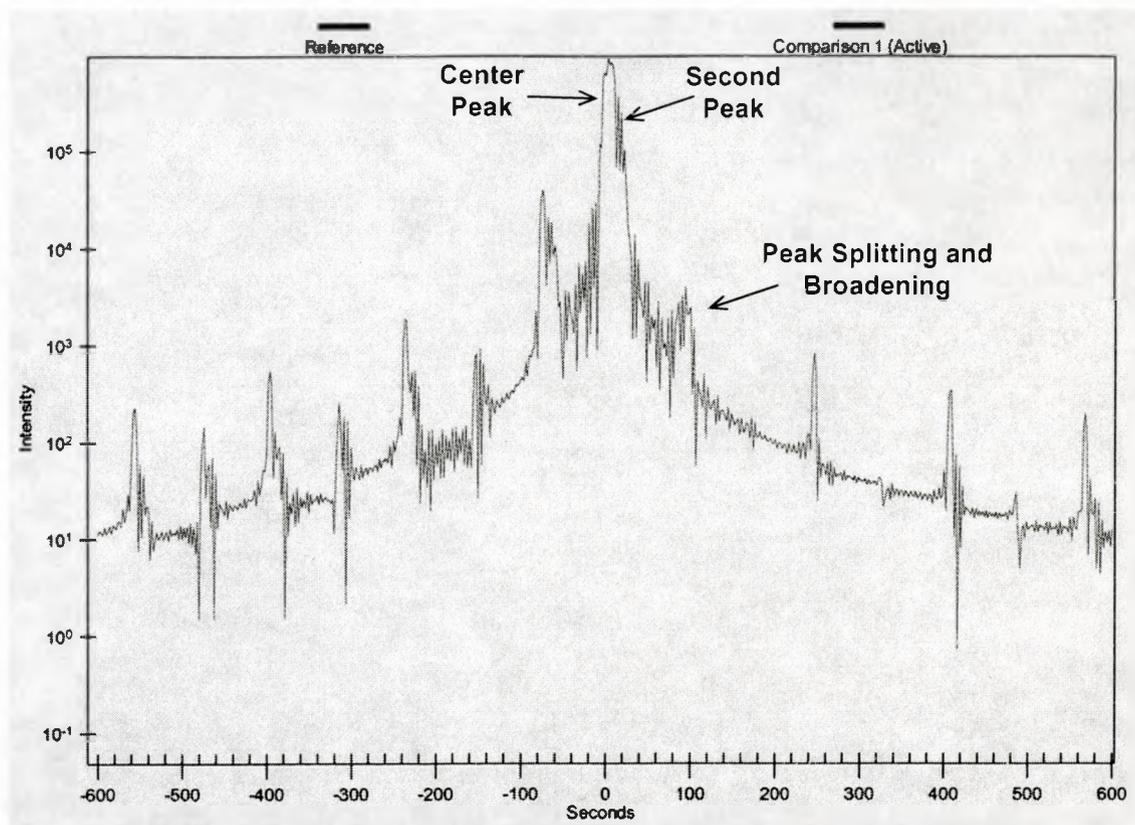
Figure 5.4.4: X-ray simulation of the 20 pair GaAs/InGaP DBR stack with a slight compositional change using Bede Version 3.0 software.

As can be seen, there is some noticeable broadening and splitting of the peaks. In addition, a separate peak is present just to the right of the substrate peak indicating the existence of a slight lattice mismatch. Other simulations were also conducted with larger compositional modifications, however, their results yielded plots that in no way even resembled the original.

The next step taken in the simulation perturbations was a slight change made to the thickness of the GaAs layer in the first 12 layers of the superlattice. The thickness was increased from 122.0nm to 125.0nm, a difference of 2.4%. The effects of this minor change are plotted in Figure 5.4.5. The most notable effect of this change is an increase in the intensity of the peaks with some added oscillations near the base of each peak. Other than that, the plot is identical to the original simulation.
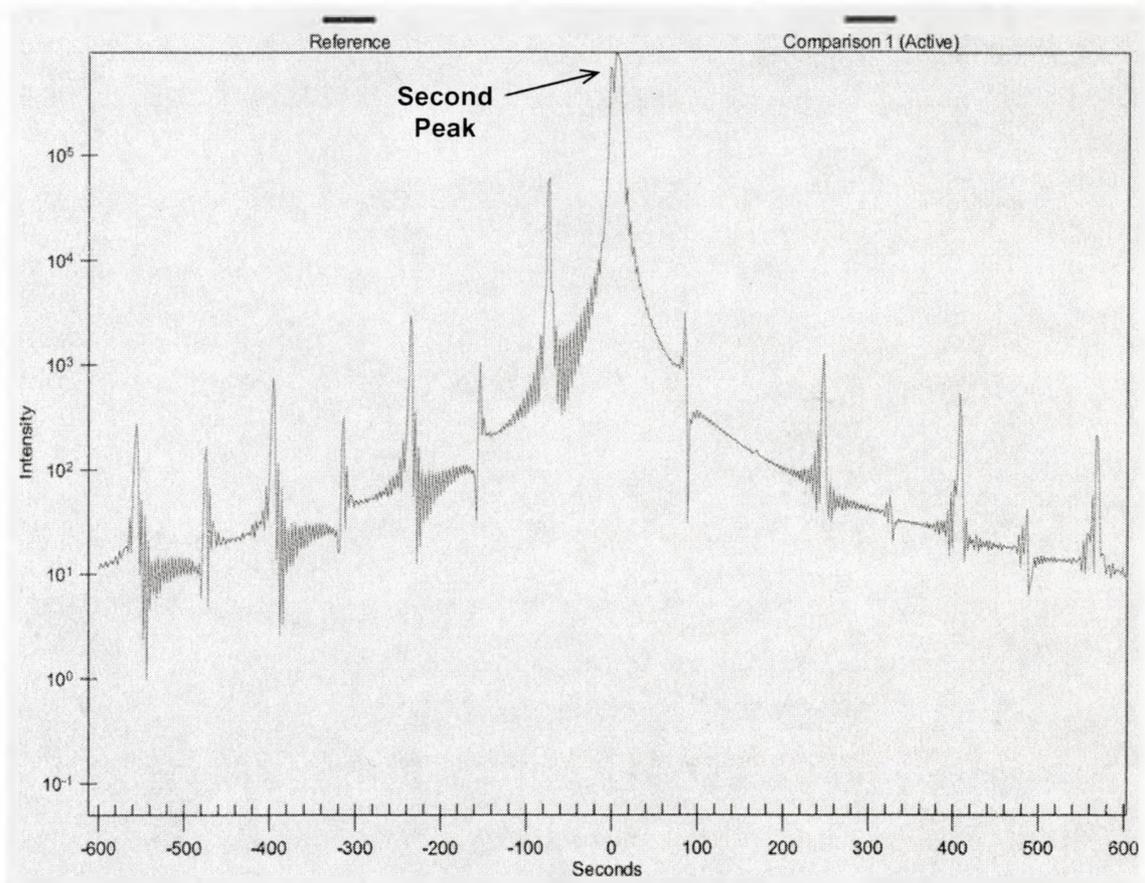
Figure 5.4.5: X-ray simulation of the 20 pair GaAs/InGaP DBR stack with a slight thickness change using Bede Version 3.0 software.

Taking into account the effects of the perturbations made to the original model, it can safely be concluded that the observed broadening and peak splitting in the experimental data has some underlying roots with slight compositional fluctuations. These fluctuations however are extremely small.

Despite the obvious flaws evident in the x-ray scan of the GaAs/InGaP DBR stack, the key factors of symmetry and periodicity of peaks was established. Hence, the x-ray analysis was a useful tool in characterization of the DBR stack.

5.5 Compositional Analysis of DBR Stack

A PL scan was carried out on all three GaAs/InGaP stacks in an attempt to determine any compositional fluctuations in the ternary layers of the super-lattice. The resultant scans can be found in Figure 5.5.1.

PL Measurements of GaAs/InGaP DBR Stacks with Various Pairs

Legend:
- 14 Pair DBR - Peak at 868nm
- 19 Pair DBR - Peak at 868nm
- 20 Pair DBR - Peak at 868nm
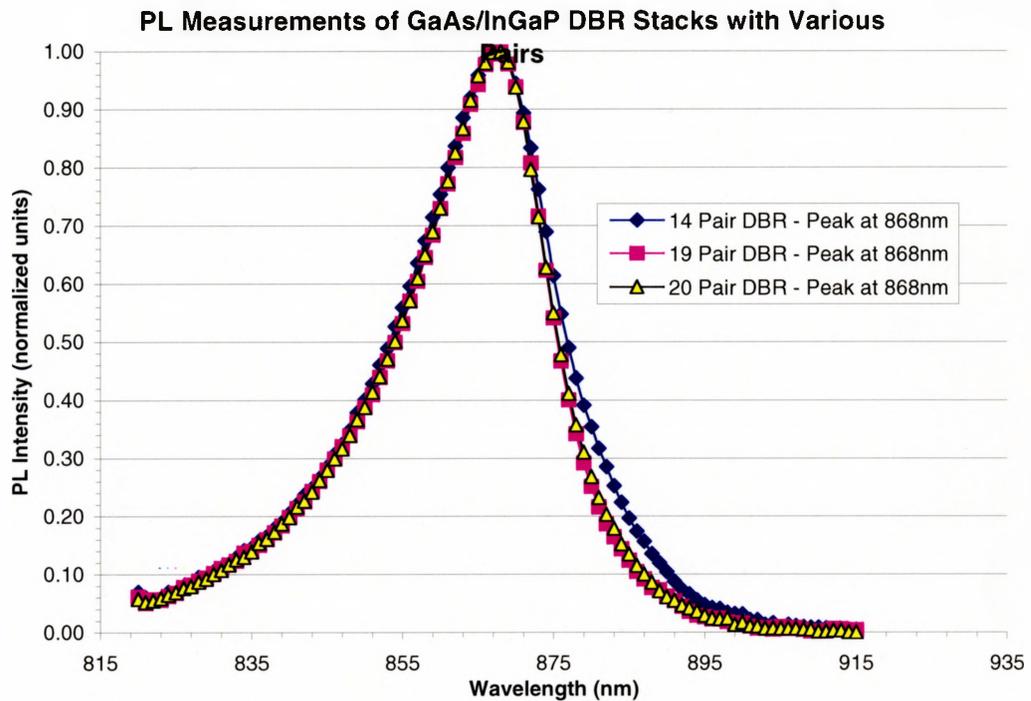
Figure 5.5.1: PL measurements taken from three GaAs/InGaP DBR stacks with various numbers of layers.

The apparent peaks in the scan all center at a wavelength of 868nm. This, however, corresponds to only the GaAs layers in the stack. The contributions from the ternary layers are entirely abolished as recombination occurs in these narrow band gap regions. Thus, the observed curves are only a representation of the top most GaAs layer. As a result, the PL scan conducted on this sample reveals no useful information with regards to the compositional makeup of the ternary layers.

5.6 Summary of Analysis

Measurements on the GaAs/InGaP DBR stack satisfactorily accomplished thier task of reconfirming the theoretical calculation process involved in the modeling of DBR stacks while verifying the abilities of the reflectivity measurement experimental setup. The first reflectivity scan of the as grown sample revealed an additional half period on top of the specified 20 layers of growth. Once this layer was removed, additional reflectivity measurements were carried out on the various numbered paired stacks. Upon theoretical fitting of the reflectivity measurements, minor growth thickness issues were uncovered. These issues were easily resolved by altering the GaAs thickness from 123.8nm to 122.0nm and the InGaP thickness from 115.0nm to 114.0nm. The resultant fits were much improved to the previous sample as extra care was taken to ensure minimal outside influences on results.

X-ray analysis of the various stacks revealed some very small compositional shifts in the ternary layers of the structure. Overall however, the x-ray scan demonstrated the periodicity of the stack and its lattice matched behavior to the GaAs substrate. A PL scan was also conducted on the samples, however, due to recombination in the binary layers, no useful information could be derived from it.

6. Conclusions and Future Work

6.1 Experimental Apparatus

The experimental apparatus utilized during experimentation required a great deal of preliminary work with calibration, alignment and various other power and wavelength tests. This was especially the case the with the normal light incidence setup. The results obtained from the normal incidence setup proved to have larger standard deviation values. Contrary to the normal incidence setup, the variable angle setup yielded results with extremely small standard deviations and hence very smooth and precise reflectivity curves with very little initial preliminary work.

From the analysis of the experimental results gathered, it was noted that the evident curve shift between the normal incidence runs and the 12° variable incident runs was almost nonexistent. This, as discussed earlier, comes about due to the minor path length difference that is present in the stack as a result of the slightly off normal incident light. Consequently, steps can be taken to completely eliminate the normal incidence setup and have one apparatus that could satisfactorily conduct both types of measurements. The only modification required to the variable angle setup to achieve this goal would be to design and build a longer (about 7-10cm longer) detector swivel arm. By adding this extension, the setup would then be able to measure reflectivities at incident angles as small as 6°. The path length difference brought about by a 6° incident light angle would then be negligible compared to the normal incidence case. This would save a great deal of time for any future experimenters while yielding improved results. In the case of building another setup, it

80

would also save roughly $3,000 to $4,000 by eliminating the need of two other detectors and various x, y, z translation stages.

In the case of future experimentation using this apparatus, one additional change should be made to further enhance measurement results. This would involve the replacement of the tunable laser as the light source for reflectivity measurements. The current tunable laser has an operational window of 100nm and thus is not wide enough to examine the characteristics of the entire stop-band of the DBR structures. By switching to a broad spectrum light source passed through a monochromator, a much larger spectral window could be examined.

6.2 Experimental Results

In summary, the InP/InGaAsP DBR stack had a predicted reflectivity of 96.6% for the as grown sample with 20 pairs at a center wavelength of 1550nm. Experimental data confirmed the reflectivity calculations, however, it revealed a shift in the position of the stop-band of the stack. This shift was attributed to a slight variation in the layer thicknesses that is believed to be consistent throughout the entire stack. The designed layer thicknesses of 111.5nm and 122.2nm for the quaternary and binary layers were determined to be 108.0nm and 117.5nm, respectively through model perturbations and curve fitting. Variable angle reflectivity measurements brought about a blue shift in the stop-band of the DBR stack as a result of a path length increase for the light traversing the stack. Transmission electron microscopy of the sample allowed for the examination of the consistency of the periodicity of the stack. Difficulties in examining the microfilms did not allow for measuring exact layer thicknesses, however, the periodicity of the sample was confirmed. X-ray analysis conducted on the sample verified once again the periodicity of the super-lattice and established an accurate lattice match to the InP substrate. Photoluminescence measurements were used to check for any compositional drift in the quaternary layer throughout the entire super-lattice. These measurements illustrated that almost no compositional change was present with the exception of a slight modification in the 20th to 24th layers.

In order to test the capabilities of the experimental setup and confirm the theoretical calculations procedure, an additional stack was design and fabricated. This stack consisted of 20 pairs of alternating GaAs/InGaP layers grown on a GaAs substrate. The predicted reflectivity was 94.9% for the as grown sample. Normal and variable incidence reflectivity measurements confirmed both the calculation process as well as the validity of the experimental setup. It was shown that a spectral resolution of 2 layers could be satisfactorily detected by the experimental setup. Once again, reflectivity measurements revealed the existence of some thickness mismatch between theoretical and experimental values. These were analyzed and the definite layer thicknesses of 114.0nm and 122.0nm for the ternary and binary layers were determined. Similar to the first sample, X-ray and photoluminescence measurements were conducted to determine the periodicity, quality of lattice matching, and any compositional variance in the ternary layer. The X-ray results confirmed both the periodicity and lattice matching of the super-lattice to the GaAs substrate. In addition, due to some peak splitting and broadening in the x-ray scans, some simulations were conducted. These simulations managed to only somewhat explain the cause of the apparent splitting and broadening of the peaks. These effects were attributed solely to a very minute compositional variance in the stack however no additional conclusions could be made as to the other causes of the observed effects. The photoluminescence measurements proved to be of no use for this sample due to recombination in the GaAs layer.

Overall, the project's outcome was successful. An effective reflectivity measurement setup was constructed to measure both normal and variable incidence of light. Furthermore, theoretical models were accurate in designing and predicting the reflective characteristics of the fabricated stacks.

6.3 Future Work with Antimonides

The semiconductor materials used to create the DBR stacks in this project produced very desirable reflectivities at a center wavelength of about 1550nm. However, the total number of layers in each stack to create such high reflectivities was rather large due to the contrast of the index of refraction between the alternating pairs. As discussed earlier, the

larger this difference is between layers, the smaller the number of pairs required in the stack to achieve high reflectivities. That is where antimode based stacks hold some promise. For example, it has been shown that a 20 pair stack consisting of alternating layers of $GaP_{0.35}Sb_{0.65}/AlP_{0.4}Sb_{0.6}$ has a reflectivity of 99.0% at a center wavelength of $1.55\mu m$ [15]. To achieve similar reflectivities with the first DBR stack designed in this project, roughly 44 pairs would be required. Hence, the benefits of antimonide based stacks are obvious

With the new molecular beam epitaxy hardware at McMaster University, it will become possible to design and fabricate antimonide based DBR stacks. In Appendix 7.6, are given some initial calculations for the design of a AlGaAsSb/AlAsSb DBR stack grown on an InP substrate. This stack will boast a predicted reflectivity of 99.33% at a center wavelength of 1550nm with a mere 20 pairs. With any luck, the work carried out in this project will serve as a starting point for any future work to be carried out here at McMaster University in the area of DBR design and fabrication.

7. Appendix

7.1 Band Gap Calculations for $Ga_xIn_{1-x}P_yAs_{1-y}$

GaP --> $AC := 2.78$

InP --> $BC := 1.344$ Binary band
                          gap values

GaAs --> $AD := 1.424$

InAs --> $BD := 0.354$

$$E(x,y,\alpha,\beta,\gamma,\theta) := \frac{\left[y \cdot (1-y) \cdot \left[(1-x) \cdot \gamma + x \cdot \theta\right] + x \cdot (1-x) \cdot \left[(1-y) \cdot \beta + y \cdot \alpha\right]\right]}{\left[x \cdot (1-x) + y \cdot (1-y)\right]}$$

$$y(x) := \frac{(0.189 - 0.405 \cdot x)}{(0.189 + 0.013 \cdot x)}$$ ⟵———— Lattice Matching Condition to InP

$\alpha(x,AC,BC) := x \cdot AC + (1-x) \cdot BC - 0.758 \cdot x \cdot (1-x)$

$\beta(x,AD,BD) := x \cdot AD + (1-x) \cdot BD - 0.40 \cdot x \cdot (1-x)$ Ternary alloy
                                                                            energy band
$\gamma(y,BC,BD) := y \cdot BC + (1-y) \cdot BD - 0.36 \cdot y \cdot (1-y)$ gaps

$\theta(y,AD,AC) := y \cdot AC + (1-y) \cdot AD - 0.186 \cdot y \cdot (1-y)$

$E_1(x) := E\big(x, y(x), \alpha(x,AC,BC), \beta(x,AD,BD), \gamma(y(x),BC,BD), \theta(y(x),AD,AC)\big)$

$E_1(0.36) = 0.904187361163128$ $y(0.36) = 0.223048327137546$

↑   ↑

Band gap energy at x Lattice matching condition
concentration of 0.36

7.2 Band Gap Calculations for $Ga_xIn_{1-x}P_y$

GaP --> $AC := 2.78$

InP --> $BC := 1.344$

GaAs --> $AD := 1.424$

InAs --> $BD := 0.354$

Binary band gap values

$$E(x,y,\alpha,\beta,\gamma,\theta) := \frac{\left[y\cdot(1-y)\cdot\left[(1-x)\cdot\gamma + x\cdot\theta\right] + x\cdot(1-x)\cdot\left[(1-y)\cdot\beta + y\cdot\alpha\right]\right]}{[x\cdot(1-x) + y\cdot(1-y)]}$$

$$y(x) := \frac{(0.405 - 0.405\cdot x)}{(0.0126x + 0.1895)}$$ ⟵—— Lattice Matching Condition to GaAs

$\alpha(x,AC,BC) := x\cdot AC + (1-x)\cdot BC - 0.758\cdot x\cdot(1-x)$

$\beta(x,AD,BD) := x\cdot AD + (1-x)\cdot BD - 0.40\cdot x\cdot(1-x)$

$\gamma(y,BC,BD) := y\cdot BC + (1-y)\cdot BD - 0.36\cdot y\cdot(1-y)$

$\theta(y,AD,AC) := y\cdot AC + (1-y)\cdot AD - 0.186\cdot y\cdot(1-y)$

Ternary alloy energy band gaps

$$E_1(x) := E\big(x,y(x),\alpha(x,AC,BC),\beta(x,AD,BD),\gamma(y(x),BC,BD),\theta(y(x),AD,AC)\big)$$

$E_1(0.51604) = 1.89573132719762$ $y(0.51604) = 1.00000865296834$

⬆   ⬆

Band gap energy at x Lattice matching condition
concentration of 0.51604

7.3 Sample Index of Refraction Calculation for InGaAsP

Equation to solve:

$$n = \sqrt{A\left[f(x_o) + 0.5 \cdot \left(\frac{E_o}{E_o + \Delta_o} \right)^{1.5} \cdot f(x_{os}) \right] + B}$$

Obtaining the value of *A*, *B*, and Δ_o parameters:
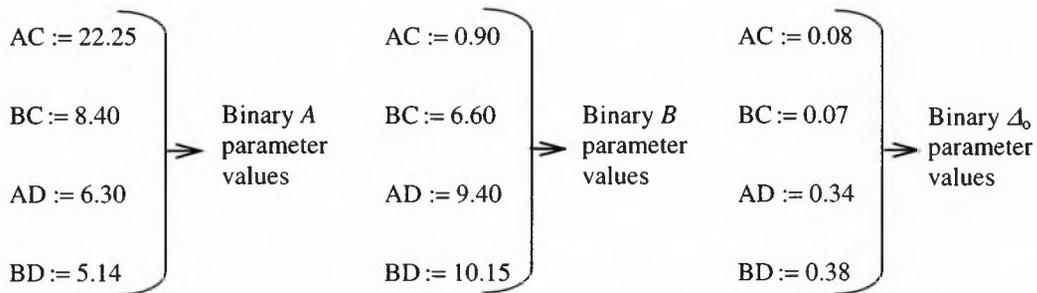
AC := 22.25	AC := 0.90	AC := 0.08
BC := 8.40 → Binary *A* parameter values	BC := 6.60 → Binary *B* parameter values	BC := 0.07 → Binary Δ_o parameter values
AD := 6.30	AD := 9.40	AD := 0.34
BD := 5.14	BD := 10.15	BD := 0.38

Each set of binary values are used to solve the below equations in order to yield the values of the *A*, *B*, and Δ_o parameters.

$$\alpha(x, AC, BC) := x\,AC + (1 - x)\,BC - 0.758\,x\,(1 - x)$$

$$\beta(x, AD, BD) := x\,AD + (1 - x)\,BD - 0.4\,x\,(1 - x)$$

$$\gamma(y, BC, BD) := y\,BC + (1 - y)\,BD - 0.36\,y\,(1 - y)$$

$$\theta(y, AD, AC) := y\,AC + (1 - y)\,AD - 0.186\,y\,(1 - y)$$

$$Q(x, y, \alpha, \beta, \gamma, \theta) := \frac{\left[y\,(1 - y) \cdot \left[(1 - x)\,\gamma + x\,\theta \right] + x\,(1 - x) \cdot \left[(1 - y)\,\beta + y\,\alpha \right] \right]}{\left[x\,(1 - x) + y\,(1 - y) \right]}$$

Therefore,

$$A = 7.218 \qquad B = 8.606 \qquad \Delta_o = 3.44 \times 10^{-20}\,\text{eV}$$

Obtaining the values of $f(x_o)$ and $f(x_{os})$ parameters:

$$f_1 := \left(\frac{h \cdot c}{\lambda \cdot E_0}\right)^{-2} \cdot \left[(2) - \sqrt{1 + \left(\frac{h \cdot c}{\lambda \cdot E_0}\right)} - \sqrt{1 - \frac{h \cdot c}{\lambda \cdot E_0}}\right] \quad \leftarrow f(x_o)$$

$$f_2 := \left[\frac{h \cdot c}{\lambda \cdot (E_0 + \Delta_0)}\right]^{-2} \cdot \left[(2) - \sqrt{1 + \left[\frac{h \cdot c}{\lambda \cdot (E_0 + \Delta_0)}\right]} - \sqrt{1 - \frac{h \cdot c}{\lambda \cdot (E_0 + \Delta_0)}}\right] \quad \leftarrow f(x_{os})$$

where,

$$h := 6.626 \, 10^{-34} \quad \lambda := 1.55 \, 10^{-6} \quad c := 2.9979245810^8 \quad E_0 := 1.4466997810^{-19}$$

Therefore,

$$f_1 = 0.368$$
$$f_2 = 0.306$$

Substituting the values into the index of refraction equation:

$$n = 3.474 \ @ \ \lambda = 1.55 \mu m$$

7.4 Sample Reflectivity Calculation for InP/InGaAsP DBR Stack:

$\gamma 0 := 1$ $\gamma 1 := 3.474$ $\gamma 2 := 3.17$ $\gamma s := 3.17$ $N := 20$

⇑   ⇑   ⇑   ⇑   ⇑

Index of air   Index of quaternary   Index of binary   Index of substrate   Number of pairs

$\Delta 1 = \delta = \left(\dfrac{2 \cdot \pi}{\lambda}\right) \cdot n_1 \cdot t \cdot \cos(\theta_t) = 87.141$ $\Delta 2 = \delta = \left(\dfrac{2 \cdot \pi}{\lambda}\right) \cdot n_2 \cdot t \cdot \cos(\theta_t) = 86.397$

Solving for reflectivity:

$$\text{MatrixHigh} := \begin{pmatrix} \cosd(\Delta 1) & \dfrac{i \cdot \sind(\Delta 1)}{\gamma 1} \\ i \cdot \gamma 1 \cdot \sind(\Delta 1) & \cosd(\Delta 1) \end{pmatrix}$$

$$\text{MatrixLow} := \begin{pmatrix} \cosd(\Delta 2) & \dfrac{i \cdot \sind(\Delta 2)}{\gamma 2} \\ i \cdot \gamma 2 \cdot \sind(\Delta 2) & \cosd(\Delta 2) \end{pmatrix}$$

$M := (\text{MatrixHigh} \cdot \text{MatrixLow})^N$

$$\text{Reflectivity1} := \left(\left|\dfrac{\gamma 0 \cdot M_{0,0} + \gamma s \cdot \gamma 0 \cdot M_{0,1} - M_{1,0} - \gamma s \cdot M_{1,1}}{\gamma 0 \cdot M_{0,0} + \gamma s \cdot \gamma 0 \cdot M_{0,1} + M_{1,0} + \gamma s \cdot M_{1,1}}\right|\right)^2 = 96.6\%$$

7.5 Sample Curve Fitting Calculation for InP/InGaAsP DBR Stack:

Initial Parameter Calculations:

High Index Layer (Qauternary)

λ	Index	Thickness (nm)	θ (degrees)	δ (radians)	δ (degrees)	γ (TE)	γ (TM)
1470	3.514	108	0	1.621316571	92.942	3.514	3.514
1475	3.511	108	0	1.614441112	92.548	3.511	3.511
1480	3.508	108	0	1.607612108	92.156	3.508	3.508
1485	3.505	108	0	1.600829091	91.767	3.505	3.505
1490	3.502	108	0	1.594091597	91.381	3.502	3.502
1495	3.499	108	0	1.587399171	90.997	3.499	3.499
1500	3.496	108	0	1.58075136	90.616	3.496	3.496
1505	3.494	108	0	1.574598379	90.264	3.494	3.494
1510	3.491	108	0	1.56803698	89.887	3.491	3.491
1515	3.489	108	0	1.561966574	89.539	3.489	3.489
1520	3.486	108	0	1.555489895	89.168	3.486	3.486
1525	3.484	108	0	1.549500433	88.825	3.484	3.484
1530	3.482	108	0	1.543550118	88.484	3.482	3.482
1535	3.48	108	0	1.537638567	88.145	3.48	3.48
1540	3.478	108	0	1.531765403	87.808	3.478	3.478
1545	3.476	108	0	1.525930252	87.474	3.476	3.476
1550	3.474	108	0	1.520132748	87.141	3.474	3.474
1555	3.472	108	0	1.514372527	86.811	3.472	3.472
1560	3.47	108	0	1.508649231	86.483	3.47	3.47
1565	3.468	108	0	1.502962505	86.157	3.468	3.468
1570	3.466	108	0	1.497312	85.833	3.466	3.466
1575	3.464	108	0	1.491697371	85.511	3.464	3.464
1580	3.463	108	0	1.486547544	85.216	3.463	3.463

$$\delta = \left(\frac{2 \cdot \pi}{\lambda_o} \right) \cdot n_1 \cdot t \cdot \cos\theta_{t1}$$

$$\gamma_1 = n_1 \cdot \sqrt{\in_o \cdot \mu_o} \cdot \cos\theta_{t1}$$

$$\gamma_1 = n_1 \cdot \frac{\sqrt{\in_o \cdot \mu_o}}{\cos\theta_{t1}}$$

Low Index Layer (Binary)

λ	Index	Thickness (nm)	θ (degrees)	δ (radians)	δ (degrees)	γ (TE)	γ (TM)
1470	3.175569	117.5	0	1.59404943	91.379	3.176	3.176
1475	3.174902	117.5	0	1.58831208	91.050	3.175	3.175
1480	3.174244	117.5	0	1.58261778	90.723	3.174	3.174
1485	3.173593	117.5	0	1.57696601	90.399	3.174	3.174

1490	3.172951	117.5	0	1.57135626	90.078	3.173	3.173
1495	3.172318	117.5	0	1.56578806	89.759	3.172	3.172
1500	3.171692	117.5	0	1.5602609	89.442	3.172	3.172
1505	3.171074	117.5	0	1.55477432	89.127	3.171	3.171
1510	3.170464	117.5	0	1.54932784	88.815	3.170	3.170
1515	3.169861	117.5	0	1.543921	88.505	3.170	3.170
1520	3.169266	117.5	0	1.53855334	88.197	3.169	3.169
1525	3.168678	117.5	0	1.53322442	87.892	3.169	3.169
1530	3.168097	117.5	0	1.52793381	87.589	3.168	3.168
1535	3.167523	117.5	0	1.52268106	87.287	3.168	3.168
1540	3.166957	117.5	0	1.51746574	86.988	3.167	3.167
1545	3.166397	117.5	0	1.51228745	86.692	3.166	3.166
1550	3.165844	117.5	0	1.50714577	86.397	3.166	3.166
1555	3.165297	117.5	0	1.50204029	86.104	3.165	3.165
1560	3.164757	117.5	0	1.49697061	85.814	3.165	3.165
1565	3.164223	117.5	0	1.49193634	85.525	3.164	3.164
1570	3.163696	117.5	0	1.48693709	85.238	3.164	3.164
1575	3.163175	117.5	0	1.48197247	84.954	3.163	3.163
1580	3.16266	117.5	0	1.47704213	84.671	3.163	3.163

$$\delta = \left(\frac{2 \cdot \pi}{\lambda_o}\right) \cdot n_2 \cdot t \cdot \cos\theta_{t2}$$

$$\gamma_2 = n_2 \cdot \sqrt{\epsilon_o \cdot \mu_o} \cdot \cos\theta_{t2}$$

$$\gamma_o = n_o \cdot \sqrt{\epsilon_o \cdot \mu_o} \cdot \cos\theta_o$$

$$\gamma_2 = n_2 \cdot \frac{\sqrt{\epsilon_o \cdot \mu_o}}{\cos\theta_{t2}}$$

$$\gamma_s = n_s \cdot \sqrt{\epsilon_o \cdot \mu_o} \cdot \cos\theta_s$$

λ	γ (Air)	γ (Substrate)
1470	1	3.175569
1475	1	3.174902
1480	1	3.174244
1485	1	3.173593
1490	1	3.172951
1495	1	3.172318
1500	1	3.171692
1505	1	3.171074
1510	1	3.170464
1515	1	3.169861
1520	1	3.169266
1525	1	3.168678
1530	1	3.168097
1535	1	3.167523
1540	1	3.166957
1545	1	3.166397
1550	1	3.165844
1555	1	3.165297
1560	1	3.164757
1565	1	3.164223
1570	1	3.163696
1575	1	3.163175
1580	1	3.16266

MathCAD Reflectivity Program:

$TOL := 1 \cdot 10^{-10}$ $sind(x) := sin(x \cdot deg)$ $cosd(x) := cos(x \cdot deg)$

$\gamma 0 := 1$ $N := 20$

$\Delta 1 :=$ 💾 $\Delta 2 :=$ 💾 $I :=$ 💾

     C:\..\del1.txt   C:\..\del2.txt   C:\..\indexQUAD.txt

$I2 :=$ 💾 $I3 :=$ 💾

     C:\..\IndexInP.txt   C:\..\IndexSUB.txt

Initial parameters loaded from Microsoft Excel
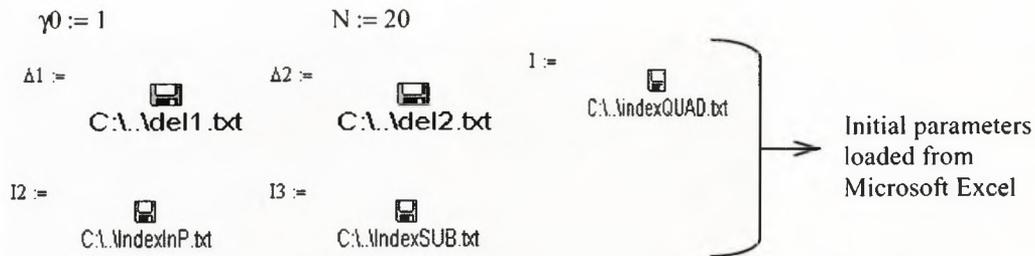
$Reflection :=$ for $i \in 0 .. rows(\Delta 1) - 1$

$\delta 1 \leftarrow \Delta 1_i$

$\gamma s \leftarrow I3_i$

$\gamma 2 \leftarrow I2_i$

$\gamma 1 \leftarrow I_i$

$\delta 2 \leftarrow \Delta 2_i$

$$MHigh \leftarrow \begin{pmatrix} cosd(\delta 1) & \dfrac{i \cdot sind(\delta 1)}{\gamma 1} \\ i \cdot \gamma 1 \cdot sind(\delta 1) & cosd(\delta 1) \end{pmatrix}$$

$$MLow \leftarrow \begin{pmatrix} cosd(\delta 2) & \dfrac{i \cdot sind(\delta 2)}{\gamma 2} \\ i \cdot \gamma 2 \cdot sind(\delta 2) & cosd(\delta 2) \end{pmatrix}$$

$M \leftarrow (MHigh \cdot MLow)^N$

$$r_i \leftarrow \frac{\gamma 0 \cdot M_{0,0} + \gamma s \cdot \gamma 0 \cdot M_{0,1} - M_{1,0} - \gamma s \cdot M_{1,1}}{\gamma 0 \cdot M_{0,0} + \gamma s \cdot \gamma 0 \cdot M_{0,1} + M_{1,0} + \gamma s \cdot M_{1,1}}$$

$R_i \leftarrow (|r_i|)^2$

R

	0
0	0.465
1	0.486
2	0.47
3	0.412
4	0.304
5	0.168
6	0.121
7	0.281
8	0.529
9	0.707
10	0.813
11	0.873
12	0.909
13	0.93
14	0.944
15	0.953

$Reflection =$

The values found in the Reflection table above are then fitted to the experimental data using a least squares fit method to determine the quality of fit.

7.6 Antimode Based DBR Stack Design Calculations

$Al_xGa_{1-x}As_ySb_{1-y}$ Band Gap and Composition Calculations:

$AC := 3.03$

$BC := 1.424$ $\quad\longrightarrow$ Binary band gap values

$AD := 2.3$

$BD := 0.75$

$$E(x,y,\alpha,\beta,\gamma,\theta) := \frac{\left[y\cdot(1-y)\cdot\left[(1-x)\cdot\gamma + x\cdot\theta\right] + x\cdot(1-x)\cdot\left[(1-y)\cdot\beta + y\cdot\alpha\right]\right]}{\left[x\cdot(1-x) + y\cdot(1-y)\right]}$$

$$y(x) := \frac{(0.227 + 0.04\cdot x)}{(0.443 + 0.033\cdot x)} \quad\longleftarrow\quad \text{Lattice Matching Condition to InP}$$

$\alpha(x,AC,BC) := x\cdot AC + (1-x)\cdot BC - 0.438\cdot x\cdot(1-x)$

$\beta(x,AD,BD) := x\cdot AD + (1-x)\cdot BD - 0.47\cdot x\cdot(1-x)$ $\quad\longrightarrow$ Ternary alloy energy band gaps

$\gamma(y,BC,BD) := y\cdot BC + (1-y)\cdot BD - 1.2\cdot y\cdot(1-y)$

$\theta(y,AD,AC) := y\cdot AC + (1-y)\cdot AD - 0.72\cdot y\cdot(1-y)$

$E_1(x) := E\big(x,y(x),\alpha(x,AC,BC),\beta(x,AD,BD),\gamma(y(x),BC,BD),\theta(y(x),AD,AC)\big)$

$E_1(0.05) = 0.925817307678285$ $\qquad\qquad$ $y(0.05) = 0.515011807039244$

Band gap energy at x concentration of 0.05 $\qquad\qquad$ Lattice matching condition

$$Al_{0.05}Ga_{0.95}As_{0.515}Sb_{0.485}$$

$AlAs_ySb_{1-y}$ Band Gap and Composition Calculations:

$AC := 3.03$

$BC := 0$

$AD := 2.3$

$BD := 0$

Binary band gap values

$$Q(x, y, \alpha, \beta, \gamma, \theta) := \frac{\left[y \cdot (1 - y) \cdot \left[(1 - x) \cdot \gamma + x \cdot \theta \right] + x \cdot (1 - x) \cdot \left[(1 - y) \cdot \beta + y \cdot \alpha \right] \right]}{\left[x \cdot (1 - x) + y \cdot (1 - y) \right]}$$

$$y(x) := \frac{(0.227 + 0.04 \cdot x)}{(0.443 + 0.033 \cdot x)}$$

Lattice Matching Condition to InP

$x := 1$ $y := 0.5609$

$\alpha(x, AC, BC) := x \cdot AC + (1 - x) \cdot BC - 0.438 x \cdot (1 - x)$

$\beta(x, AD, BD) := x \cdot AD + (1 - x) \cdot BD - 0.47 x \cdot (1 - x)$

$\gamma(y, BC, BD) := y \cdot BC + (1 - y) \cdot BD - 1.2 y \cdot (1 - y)$

$\theta(y, AD, AC) := y \cdot AC + (1 - y) \cdot AD - 0.72 y \cdot (1 - y)$
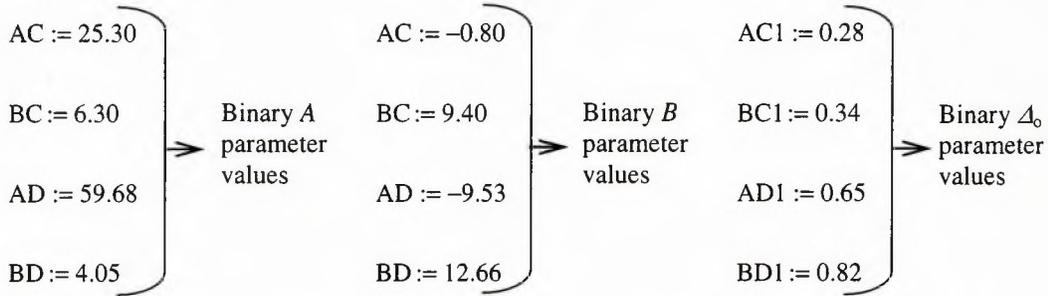
Ternary alloy energy band gaps

$E_1(x) := Q(x, y, \alpha(x, AC, BC), \beta(x, AD, BD), \gamma(y, BC, BD), \theta(y, AD, AC))$

$E_1(1) = 2.532$

Band gap energy at x concentration of 1.0

$AlAs_{0.5605}Sb_{0.4395}$

Obtaining the value of A, B, and Δ_o parameters for AlGaAsSb layer:

$AC := 25.30$

$BC := 6.30$ → Binary A parameter values

$AD := 59.68$

$BD := 4.05$

$AC := -0.80$

$BC := 9.40$ → Binary B parameter values

$AD := -9.53$

$BD := 12.66$

$AC1 := 0.28$

$BC1 := 0.34$ → Binary Δ_o parameter values

$AD1 := 0.65$

$BD1 := 0.82$

Each set of binary values are used to solve the below equations in order to yield the values of the A, B, and Δ_o parameters.

$$\alpha(x, AC, BC) := x \cdot AC + (1 - x) \cdot BC - 0.438 \cdot x \cdot (1 - x)$$

$$\beta(x, AD, BD) := x \cdot AD + (1 - x) \cdot BD - 0.47 \cdot x \cdot (1 - x)$$

$$\gamma(y, BC, BD) := y \cdot BC + (1 - y) \cdot BD - 1.2 \cdot y \cdot (1 - y)$$

$$\theta(y, AD, AC) := y \cdot AC + (1 - y) \cdot AD - 0.72 \cdot y \cdot (1 - y)$$

$$Q(x, y, \alpha, \beta, \gamma, \theta) := \frac{\left[y \cdot (1 - y) \cdot \left[(1 - x) \cdot \gamma + x \cdot \theta \right] + x \cdot (1 - x) \cdot \left[(1 - y) \cdot \beta + y \cdot \alpha \right] \right]}{\left[x \cdot (1 - x) + y \cdot (1 - y) \right]}$$

Therefore,

$$A = 6.797 \qquad B = 9.93 \qquad \Delta_o = 5.008 \times 10^{-20} eV$$

Obtaining the value of A, B, and Δ_o parameters for AlAsSb layer:

$AC := 25.30$

$BC := 0$ → Binary A parameter values

$AD := 59.68$

$BD := 0$

$AC := -0.8$

$BC := 0$ → Binary B parameter values

$AD := -9.53$

$BD := 0$

$AC1 := 0.28$

$BC1 := 0$ → Binary Δ_o parameter values

$AD1 := 0.65$

$BD1 := 0$

Each set of binary values are used to solve the below equations in order to yield the values of the A, B, and Δ_o parameters.

$$\alpha(x, AC1, BC1) := x \cdot AC1 + (1 - x) \cdot BC1 - 0.438 \, x \, (1 - x)$$

$$\beta(x, AD1, BD1) := x \cdot AD1 + (1 - x) \cdot BD1 - 0.47 \, x \, (1 - x)$$

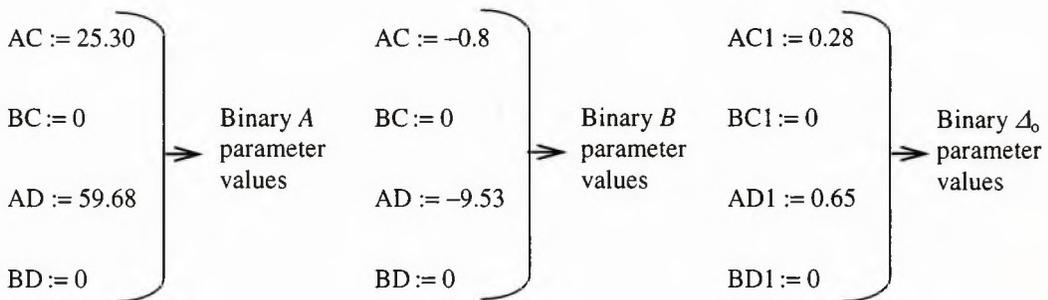$$\gamma(y, BC1, BD1) := y \cdot BC1 + (1 - y) \cdot BD1 - 1.2 \, y \, (1 - y)$$

$$\theta(y, AD1, AC1) := y \cdot AC1 + (1 - y) \cdot AD1 - 0.72 \, y \, (1 - y)$$

$$Q(x, y, \alpha, \beta, \gamma, \theta) := \frac{\left[y \cdot (1 - y) \cdot \left[(1 - x) \cdot \gamma + x \cdot \theta \right] + x \cdot (1 - x) \cdot \left[(1 - y) \cdot \beta + y \cdot \alpha \right] \right]}{\left[x \cdot (1 - x) + y \cdot (1 - y) \right]}$$

Therefore,

$$A = 40.219 \qquad B = -4.811 \qquad \Delta_0 = 4.336 \times 10^{-20} \text{eV}$$

Calculating the Index of Refraction for both Layers:

$$n(A, B) := \sqrt{A \cdot \left[f_1 + 0.5 \cdot \left(\frac{E_0}{E_0 + \Delta_0} \right)^{1.5} \cdot f_2 \right] + B}$$

$$n(A, B) = 3.605\blacksquare \qquad\qquad n(A, B) = 3.16341173700898$$

$$\uparrow \qquad\qquad\qquad\qquad \uparrow$$

Index for AlGaAsSb layer $\qquad$ Index for AlAsSb layer

Reflectivity Calculation for DBR Stack at Normal Incidence with Center Wavelength of 1550µm:

$$R = \left[\frac{\left(\frac{n_o}{n_s} \right)\left(\frac{n_L}{n_H} \right)^{2N} - 1}{\left(\frac{n_o}{n_s} \right)\left(\frac{n_L}{n_H} \right)^{2N} + 1} \right]^2 \qquad\qquad R = 99.33\%$$

8. References

[1] Shun L. Chuang, *Physics of Optoelectronic Devices*, Wiley Series in Pure and Applied Optics, New York, 1995.

[2] L. A. Coldren and S. W. Corzine, *Diode Lasers and Photonic Integrated Circuits*, Wiley, New York, 1995.

[3] A. Wilmsen, T. Temkin, and L. Coldren, *Vertical-Cavity Surface-Emitting Lasers: Design, Fabrication, Characterization, and Applications*, Cambridge Studies in Modern Optics, New York, 1999.

[4] Russian Scientific Journal.
http://www.scientific.ru/journal/news/n100501.html

[5] F. H. Peters, M. L. Majewski, M. G. Peters, J. W. Scott, B. J. Thibeault, D. B. Young, and L. A. Coldren, "Vertical Cavity Surface Emitting Laser Technology," *SPIE Proceedings*, 1851, 122-127, 1993.

[6] G. Parry and A. Khan, "Vertical Cavity Surface Emitting Lasers (VCSELs)," *Department of Materials Engineering Newsletter*, Oxford University.
http://www.materials.ox.ac.uk/

[7] O. Blum, I. J. Fritz, L. R. Dawson, A. J. Howard, T. J. Headly, J. F. Klem, and T. J. Drummond, "Highly reflective, long wavelength AlAsSb/GaAsSb distributed Bragg reflector grown by molecular beam epitaxy on InP substrates," *Appl. Phys. Lett.*, **66**(3), January 1995.

[8] C. J. Chang-Hasnian, "Progress and Prospects of Long-Wavelength VCSELs," *IEEE Optical Communications*, Vol. 41, Feb. 2003.

[9] Hewlett Packard, *HP 8168E/8168F Tunable Laser Source Technical Specifications*, February 2000.

[10] K. Killen, & W. Breiland, "In situ spectral reflectance monitoring of III-V epitaxy," *J. Electron. Mater.*, **23**, 179-183, 1994.

[11] Newport, *Fiber Pigtailed Collimators Specifications*, Model F-COL-9-15.

[12] D. I. Babic, K. Streubel, R.P Mirin, N. M. Margalit, E. L. Hu, J. E. Bowers, D. E. Mars, L. Yang, and K. Carey, "Room-Temperature Continuous-Wave Operation of 1.54µm Vertical-Cavity Lasers," *IEEE Photonics Technology Letters*, **7**(11), 1225-1227, 1995.

[13] Pedrotti & Pedrotti, *Introduction to Optics*, 2nd ed., Prentice Hall, New Jersey, 1993.

[14] S. Adachi, "Refractive indices of III-Vcompounds: Key properties of InGaAsP relevant to device design," *J. Appl. Phys.*, **53**(8), 5863-5869,1982.

[15] M. Guden & J. Piprek, "Material parameters of quaternary III-V semiconductors for multilayer mirrors at 1.55µm wavelength," *Modeling & Simulation in Materials Science & Engineering*, **4**(4), 349-357, 1996.

[16] M. J. Mondry, D. I. Babic, J. E. Brown, and L. A. Coldren, "Refractive indexes of (Al, Ga, In)As epilayers on InP for optoelectronic applications," *IEEE Photon. Technol. Lett.*, **4**(6), 627-630, 1992.

[17] O. Blum, I. J. Fritz, L. R. Dawson, and T. J. Drummond, "Digital alloy AlAsSb/AlGaAsSb distributed Bragg reflectors lattice matched to InP for 1.3-1.55µm wavelength range," *Electron. Lett.*, **33**(22), 1878-1880, 1997.

[18] S. Adachi, *Physical Properties of III-V Semiconductor Compounds*, Wiley, New York, 1992.

[19] A. Yariv, *Quantum Electronic*, 3rd ed., Wiley, New York, 1989.

[20] M. Linnik, A. Christou, "Calculations of optical properties for quaternary III-V semiconductors alloys in the transparent region and above (0.2-4.0eV)," *Physica B*, vol. 318, 140-161, 2002.

[21] E. F. Schubert, "Refractive index and extinction coefficient of materials," *Filmetrics Cooperation of San Diego*, 2004.

[22] P. A. Judge, C. H. L. Quay, and J. A. Hudgings, "Robustness to optical feedback of oxide-confined versus proton-implanted vertical-cavity surface-emitting lasers," *Applied Physics Letters.*, vol. 81, 34-37, Nov. 2002.

[23] A. R. Clawson, "Guide to references on III-V semiconductor chemical etching," *Materials Science & Engineering*, 1-438, 2001.

[24] Hou, H. Q., Chui, H. C., Choquette, K. D., Hammons, B. E., Breiland, W. G., and Geib, K. M., "Highly uniform and reproducible Vertical-cavity surface-emitting lasers grown by metalorganic vapor phase epitaxy with in situ reflectometry," *IEEE Photonics Technol. Lett.*, **8**(10), 1285-7, 1996.

[25] L. A. Coldren, *Lasers and Modulators for OEICs in Integrated Optoelectronics*, Academic Press, New York, 1994.

[26] Erwin Kreyszig, *Advanced Engineering Mathematics*, Wiley, New York, 1998.

[27] Newport, *818 Series Low Power Detectors*, Key Features and Specifications.

[28] Ray R. Lapierre, M.A.Sc. Thesis (1994), Spinodal Decomposition of InGaAsP on (100) and Non-(100) InP Substrates, Dept. of Engineering Physics, McMaster University